2020

Engineered metallic foam for controlling sound and vibration

BOSTON UNIVERSITY

COLLEGE OF ENGINEERING

Dissertation

ENGINEERED METALLIC FOAM FOR CONTROLLING SOUND AND VIBRATION

by

MARK J. COPS

B.S., University of Wisconsin - Platteville, 2016
M.S., Boston University, 2019

Submitted in partial fulfillment of the

requirements for the degree of

Doctor of Philosophy

2020

Approved by

First Reader

J. Gregory McDaniel, Ph.D.
Associate Professor of Mechanical Engineering
Associate Professor of Materials Science and Engineering

Second Reader

Sheryl M. Grace, Ph.D.
Associate Professor of Mechanical Engineering

Third Reader

R. Glynn Holt, Ph.D.
Associate Professor of Mechanical Engineering

Fourth Reader

Elizabeth A. Magliula, Ph.D.
Director of Research
Naval Undersea Warfare Center (NUWC), Newport

Fifth Reader

David J. Bamford, Ph.D.
Mechanical Engineer
Naval Undersea Warfare Center (NUWC), Newport

Acknowledgments

I am most grateful to my advisor, Greg, for the opportunity to work in the Sound and Vibration Laboratory. His expertise, creativity, encouragement and sense of humor have made the last four years not only educational but extremely enjoyable.

Thank you to all my committee members. To Liz and Dave for many insightful discussions during telcons and for hosting me for two summers. To Professors Grace and Holt for their insights at multiple stages throughout my graduate career including qualification exams, prospectus, and courses.

Additionally I owe many thanks to Eric, Doug, and others at NUWC who all gave me some of their time assisting with experiments. To Enrique at BU for working closely with me at the start of my graduate career. To Jay at Acentech for assisting with impedance tube measurements. Thanks to other engineering Ph.D. students especially the 4th floor, for their engaging discussions as well as their friendship. Thanks to Alyssa for being a constant source of positivity and enthusiasm in the lab, and for her valuable input on numerous research problems and presentations, all the way up to my final defense.

Thanks to Greg and Liz for writing the proposal and obtaining funding for this work. Thanks to the Naval Undersea Research Program and Maria Medeiros at ONR for the awarded grant.

Lastly, thanks to my family and Mary Beth for their continued interest, support, and encouragement.

ENGINEERED METALLIC FOAM FOR CONTROLLING SOUND AND VIBRATION

MARK J. COPS

Boston University, College of Engineering, 2020

Major Professor: J. Gregory McDaniel, Ph.D.
Associate Professor of Mechanical Engineering
Associate Professor of Materials Science and Engineering

ABSTRACT

Many structural acoustic and vibration designs rely extensively on materials that are light-weight, stiff, and highly damped. Advanced materials such as metallic foams can be engineered to achieve these properties in order to control sound and vibration for a variety of aerospace, maritime, and ground transportation applications.

In this work, the structural and acoustic properties of commercially available and digitally designed metallic foams are analyzed through numerical and experimental methods. Furthermore as a post-manufacturing process, metallic foams can be engineered in order to preferentially alter the microstructure and achieve material property enhancements. In this work, the following engineering methods are proposed and investigated: plastic deformation and material saturation.

When a metallic foam is plastically deformed, the foam's porosity and pore shape are dramatically altered. This transformation in microstructure can lead directly to changes in bulk properties. In this work, a method for triaxial hydrostatic compression of metallic foams is proposed and demonstrated experimentally. The structural properties of transformed foams are tested using a load cell with digital image correla-

tion. Transformed foams exhibit higher compliance, higher toughness, and a reduced Poisson ratio. Measurement and analysis of acoustic properties indicate that the transformed foams can absorb significantly more sound than the conventional samples of equal thickness in the test range of 0.25 – 4.50 kHz.

Due to their open-cell microstructure, metallic foams can be filled with saturating materials. In this work, metallic foams saturated with viscous liquids are investigated for reducing vibration transmissibility in a structure. For the best performing saturated foam subject to a transient excitation, an order of magnitude increase in damping ratio is measured. Additionally, a composite foam (consisting of metallic foam saturated with polyurethane foam) is fabricated to enhance acoustic properties. For the best performing composite foam at normal incidence, the sound absorption coefficient is improved by a factor of 6 near 0.60 kHz and by a factor of 2 up to 4.50 kHz.

Lastly, two methods for estimating acoustic absorption in metallic foams are presented which utilize finite element analysis and boundary layer theory. The proposed methods are discussed for commercially available foams as well as for representative digital designs. Limitations and assumptions of the methods pertaining to size scales and boundary layer features are addressed.

Contents

List of Tables

List of Figures

List of Abbreviations

CAD	.....	computer aided design
DIC	.....	digital image correlation
FEA	.....	finite element analysis
JCA	.....	Johnson-Champeux-Allard
JCAL	.....	Johnson-Champeux-Allard-Lafarge
JCAPL	.....	Johnson-Champeux-Allard-Pride-Lafarge
Mac OS	.....	Macintosh operating system
micro-CT	.....	micro-computed tomography
OpenGL	.....	Open Gaming Language
PPI	.....	pores per inch
PU	.....	polyurethane
SDF	.....	signed distance function

Chapter 1

Introduction

1.1 Motivation

Materials that are light-weight, stiff, and highly damped are essential for many mechanical designs. Advanced materials such as metallic foams can be engineered to achieve these properties in order to control sound and vibration for a variety of aerospace, maritime, and ground transportation applications. For example, metallic foams may find wide use as a component in automotive bumpers, due to the reduced mass and ability to absorb impact energy during plastic collapse. Alternatively, metallic foams could find use in jet turbine or fan liners, to absorb acoustic energy while maintaining thermal stability. Use of metallic foams for the aforementioned multi-functional applications requires a knowledge of the material properties which may change dramatically over frequency and temperature.

Currently, there are several commercial manufacturers of metallic foams; however limited technical data and material specifications are available from these manufacturers. This research is motivated by the desire to understand and predict material properties of both commercial and engineered metallic foams. "Engineered" metallic foams in this work refers to either a purposeful design of the microstructure prior to manufacturing or a post-manufacturing process to enhance the properties of the foam. This work will leverage both concepts by investigating engineering methods on commercially available metallic foams (which contain a randomized microstructure) as well as by investigating the design of the foam's microstructure which may

be specially fabricated by techniques such as 3D printing. The following engineering methods are proposed as methods to preferentially alter a metallic foam after fabrication: plastic deformation and material saturation. A goal of this work is to expand the design space for industrial designers and materials engineers by exploring enhancements in materials properties for engineered foams compared to conventional foams.

1.2 Overview and Significance of this Thesis

The body of this work is divided into four main chapters. In Chapter 2, the stiffness and mass properties of metallic foams are investigated. Digital designs of foams are presented and analyzed for effective static elastic properties such as elastic modulus and Poisson ratio. Additionally, high fidelity models of commercially available foams are constructed from micro-computed tomography. Implications of the foam properties such as pores per inch, porosity, host metal, and strut density are examined. As a result, it is observed that the most efficient foams in terms of stiffness-to-weight ratio are those with hollow strut cross sections.

In Chapter 3, an engineering method for triaxial hydrostatic compression of metallic foam is presented to preferentially alter the foam's microstructure. The method is demonstrated on an assortment of open-cell aluminum foams with varying pore size and porosity. Measurements of acoustic absorption indicate that the compressed samples absorb significantly more sound than the conventional samples of equal thickness in the test range from $0.25 - 4.50\,\mathrm{kHz}$. An analysis is presented which links the microstructure properties of compressed foam samples to conventional samples, thereby providing a means to estimate acoustic absorption trends for compressed samples through use of existing models. Additionally, hydrostatically compressed foams are prepared and tested mechanically to evaluate bulk mechanical properties utilizing a

load cell and digital image correlation. The hydrostatically deformed foam exhibits higher compliance, higher toughness, and a reduced Poisson ratio.

In Chapter 4, a composite foam consisting of open-cell metallic foam embedded with polyurethane foam is fabricated and evaluated for sound absorbing properties. The best performing composite foam increased the sound absorption by a factor of 6 (from 0.1 – 0.6) in the low frequency test range near 0.6 kHz and by a factor of 2 (from 0.2 – 0.4) in the frequency range up to 4.50 kHz, compared to the original metallic foam. A lumped element model is used to predict and elucidate the absorption mechanisms for the composite, as well as for pure metallic foam and pure polyurethane foam. The model gives insight into the physical mechanisms that control acoustic absorption, including thermo-viscous effects at pore interfaces, structural damping effects due to foam elasticity, and coupling effects due to the interaction of air, metal, and polyurethane in the composite. Additionally, a simplified two parameter model is used to elucidate acoustic absorption trends for composite foams. The developed composite foams are advantageous for engineering and architectural applications where combined high stiffness and sound absorption are required. Furthermore in Chapter 4, experimental investigations of vibration damping of metallic foams saturated by viscous liquids are described for both steady state and transient experiments. Results are presented for metallic foam that was saturated with petroleum jelly, which increased the damping ratio by an order of magnitude in a transient ring down experiment.

Lastly in Chapter 5, a method for estimating acoustic absorption in foams is presented using a combination of micro-computed tomography, finite element analysis, and boundary layer loss theory. In the method, the foam is assumed to be rigid-framed and the viscous and thermal boundary layers at the fluid and frame interface are assumed to be small compared to foam dimensions. The boundary layer losses

are approximated using an infinite planar model. The method is demonstrated for a commercially available open-cell metallic foam and allows for absorption to be estimated without determination of any intermediate variables that are required in existing methods. Enhancement of sound absorbing properties by selection of foam properties, such as porosity and pores per inch, is discussed. Furthermore, predicted absorption trends agree with other published models and experimental data. A simplified, two-dimensional geometry is presented in which the assumptions of this method are analyzed.

A second method for estimating acoustic absorption is also presented and discussed in Chapter 5. This method uses thermal and viscous boundary layers terms represented as acoustic boundary conditions to the Helmholtz equation for the acoustic pressure. The method is proposed for rigid-framed porous materials, where vibration of the frame is negligible compared to pressure fluctuations in air. The computational efficiency of the method is shown to improve by two orders of magnitude compared to a thermoviscous acoustic solver. Furthermore the method is shown to be highly accurate over geometrical features and frequencies of interest, as long as thermal and viscous boundary layers do not overlap and the effects of sharp changes in curvature are negligible. The method is demonstrated for a periodic sound absorber from the literature as well as a sound absorber with a randomly graded microstructure. Both methods discussed in this chapter are advantageous for analyzing acoustic absorption of metallic foams as well as optimizing geometrical placement for digitally designed foams.

1.3 Most Relevant Literature

This chapter will conclude with a summary of the most relevant literature pertaining to this work. This summary is meant to be concise, a more in depth review will be

given in each subsequent chapter.

Fabrication and Bulk Mechanical Properties An excellent review of metallic foam manufacturing methods has been recently written [3]. Essentially there are four families of techniques that have been utilized depending on the state of the metal: metal vapor, liquid metal, powdered metal, and metal ions. Knowledge of the manufacturing techniques are important for considering design limitations, ranges of available material properties, and production costs. The predominant foam studied in this work is an open-cell foam sold by ERG Aerospace Corp. Although the manufacturing method is proprietary, it is believed to be an investment casting process that uses a polyurethane foam precursor [3]. Additional manufacturing methods as well as an extensive list of commercial metallic foam suppliers is given in [4].

The properties of metallic foams and other cellular solids has been studied extensively and compiled in a well-known textbook on cellular solids [5]. The single most important mass property of a foam is its relative density, or the ratio of the foam density to the solid (host material) density. The relative density along with the structure of the foam (open-cell versus closed-cell) can be used to derive scaling laws which predict the bulk mechanical properties of foams. While the deformation of most common foams is dominated by beam bending, topologies can be designed to promote beam stretching as the dominating mechanism [6]. An analysis is presented in [7] for which contributions of beam bending, twisting, and extension are all considered for periodic unit cell. For pure bending, the stiffness is related to the density by a power exponent of 2, inclusion of the additional terms reduced the power exponent by less than 5%.

Plastic Deformation Metallic foams can be plastically deformed if the local stress exceeds the yield stress of the host material. The precise application of plastic strain to metallic foams, especially open-cell, has been shown in the literature

to yield dramatically different materials properties compared to conventional foams. The pioneering work in this topic was done by Lakes, who proposed a method of transforming open-cell metallic foams by plastic deformation to achieve a negative Poisson ratio [8], [9]. The plastic deformation aims to buckle struts of the foam to transform the pore shape from an outward oval to an inward, buckling re-entrant shape. This is usually achieved for volume compression ratios greater than 2. Currently in the literature, the method for applying plastic deformation is through incremental, orthogonal, plastic strain using a vise. This method has a couple of disadvantages. First, it is very time consuming, as one side must be compressed at a time. Second, foam samples tend to shear during uniaxial compression, which causes distorted deformation and may limit effects of altering material properties. In addition to negative Poisson ratio, transformed metallic foams have been shown to have superior shear strength, crack resistance, and fracture toughness [10], [11].

Saturating Materials Through additional manufacturing processes, open-cell foams can be saturated with filler materials to dramatically change the material properties. For soft rubber foams, air saturation has been shown to add vibration damping to the foam due friction arising from forcing air through the pores [12], [13]. Viscous liquids such as silicone oil have also been saturated into soft foams [14] and have shown agreement to theory presented in [13]. To the author's knowledge, there has not been an investigation into vibration damping of fluid saturated metallic foams. For acoustic absorption underwater, there has been some research into saturating porous materials with fluids other than air. Xu et. al [15] presented a silicon carbide foam saturated with silicone oil that had an experimentally measured absorption coefficient (measured in a water impedance tube) greater than 0.7 in the frequency range of 0.5 – 4.0 kHz. Additionally Wang [16] presented a set of non-dimensional analyses and numerical results to indicate that porous metal absorbers filled with a

viscous fluid and backed with a cavity could be efficient sound absorbers in water.

Metallic foams have been filled with viscoelastic materials by processes where a liquid is poured into the pores of the foam and allowed to cure. For both a randomized metallic foam [17] and a periodic lattice structure [18], a silicate rubber filler increased the foams energy absorption capacity compared to the original metallic foam when subject to quasi-static compression. A further set of experiments showed that metallic foams embedded with rubber increased the dynamic stiffness by 26.4% and the loss factor by 28.1% for a forcing frequency of up to 2 Hz [19].

Acoustic Absorption The acoustic performance of metallic foams depends highly on the microstructure. The acoustic losses arise from thermal and viscous boundary layer effects near the interface of the air and the metal. For acoustic excitation in air, metallic foams can be considered rigid due to the high stiffness of the metal compared to air [1]. An excellent textbook was written by Allard and Atalla [20] which includes modeling methods applicable to metallic foams such as rigid-framed models, multilayered absorbers, and poroelastic finite element methods. Experimental measurements have been used to characterize sound absorption in both open-cell and closed-cell foams. In general, open-cell foams have superior sound absorption because they allow propagation of the acoustic wave further into the material, whereas much of the energy is purely reflected for closed-cell foams [21], [22].

Chapter 2

Bulk Mechanical Properties of Open-cell Metallic Foams

2.1 Digital Designs from Computer Graphics

This chapter begins with a discussion of mass density and structural elastic properties of open-cell metallic foams. Background on microstructure features and definitions of some important foam vocabulary will be given. Furthermore, this section describes the use of 3D computer graphics as a tool for designing the microstructure of metallic foams. Resulting designs can be imported into finite element software in order to determine effective static material properties. This approach is advantageous because it allows for rapid design iteration of complex topological structures and variation of foam properties such as relative density.

2.1.1 Introduction

A typical commercially available metallic foam is shown in Figure 2·1. This foam exhibits a characteristic topology of voids and thin beam-like metallic structures called struts. The vertex location where multiple struts merge together is known as a node. This is an open cell foam, meaning that the cells are inter-connected and as a result, fluid may flow through the entire network of pores.

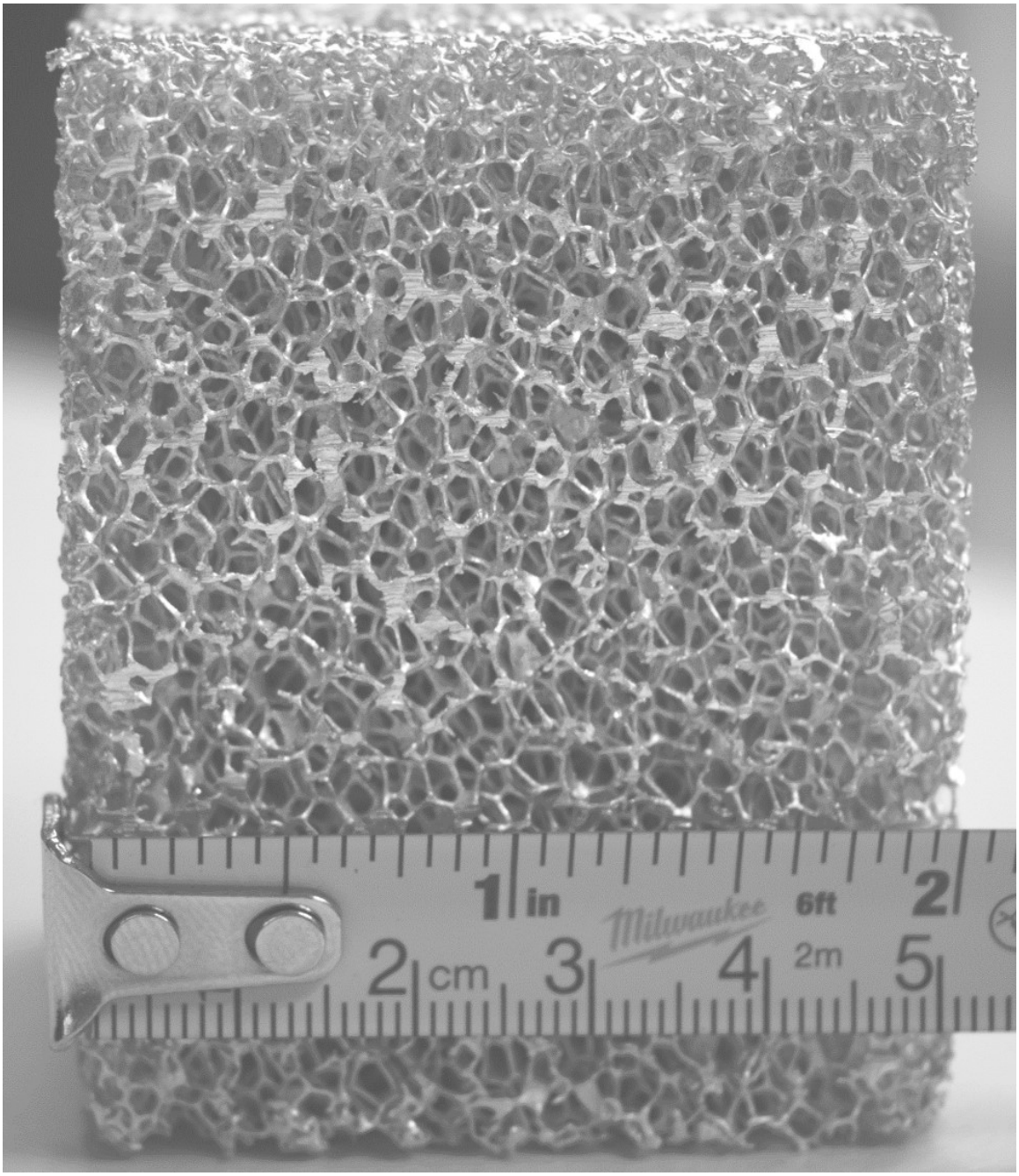

Figure 2·1: An open-cell aluminum foam, 20 PPI and 90% porosity, manufactured by ERG Aerospace Corp.

The void fraction ϕ is the ratio of void volume to total bulk volume. The effective

density of the foam ρ_f is the volume average of the constituent materials

$$\rho_f = \rho_v \phi + \rho_s (1 - \phi), \tag{2.1}$$

where subscripts f, v, and s denote the foam, void, and solid material, respectively. For many applications such as structural deformation, the air does not contribute to the structure and thus the relative density can be written as

$$\frac{\rho_f}{\rho_s} = 1 - \phi. \tag{2.2}$$

Many manufacturers also specify the number of pores per inch (PPI) as a measure of the average inverse pore size. Common foams are produced anywhere from 5 to 40 PPI (average pore diameter of 5 – 0.6 mm). The bulk mechanical properties of metallic foams and other cellular solids has been studied extensively by Gibson and Ashby [5]. Based on bending and nondimensional arguments for an open-cell square lattice, it can be shown that the material moduli are given by

$$\frac{E_f}{E_s} = C_1 \left(\frac{\rho_f}{\rho_s} \right)^2, \tag{2.3}$$

and

$$\frac{G_f}{E_s} = C_2 \left(\frac{\rho_f}{\rho_s} \right)^2, \tag{2.4}$$

where E and G are the elastic and shear modulus, respectively and C_1 and C_2 are geometric proportionality constants. For a linear-elastic and isotropic material,

$$\nu = \frac{E}{2G} - 1, \tag{2.5}$$

where ν is the Poisson ratio. Using Equations (2.3), (2.4), and (2.5), and solving for the foam Poisson ratio with the assumption that the foam behaves as a linear-elastic

isotropic material, one obtains

$$\nu_f = \frac{C_1}{2C_2} - 1 = C_3. \tag{2.6}$$

Although derived for simple geometries, the material constants $C_1 = 1$, $C_2 = 3/8$, and $C_3 = 1/3$ are found to fit experimental data to "an adequate approximation" [5] for a wide range of open cell foams.

These equations highlight the importance of foam relative density (ρ_f/ρ_s) in determining material properties. Conveniently, relative density is also often one property selection made available by metallic foam manufacturers, thus understanding its relationship to material properties is crucial for industrial designers and engineers.

There are inherent difficulties with experimentally determining material properties for foams. For example, in compression the size of the specimen can highly influence mechanical measurements due to local inhomogeneities and buckling effects [23]. In tension or shear, the foams are more difficult to test due to mounting considerations which may require fixture design and special preparation to grip the sample. There are also difficulties with accurately measuring Poisson ratio when considering non-uniform edge deformation.

The remainder of Section 2.1 describes the use of 3D computer graphics to design cellular structures, which can be imported into finite element software in order to determine effective static material properties. This approach is advantageous because it allows for rapid design iterations and variations of the foam's mass properties.

2.1.2 Methodology

Computer Graphics

Open Gaming Language (OpenGL) is a programming language used in computer graphics for display rendering, artistic graphics, animation creation, and video game

creation. Its main advantage is the increased processing speed and efficiency due to the ability to interface with a computers graphic processing unit. F3 is a software for Mac OS which utilizes OpenGL and signed-distance functions (SDFs) to design 3D structures. Also known as a shader language, the concept is as follows - a display can be rendered by treating each pixel as a coordinate point and writing a function to output a desired display for that pixel. The function computes the distance from the origin to the coordinate point. Additional operations are then performed to design the structure, where return of a negative magnitude corresponding to a particular coordinate point yields a solid material while a positive magnitude yields void space. Mathematically, this is known as a signed-distance function (SDF) [24] and can be written as

$$f(x,y,z) = \begin{cases} -d(x,y,z,\partial\Omega), & \text{for } x,y,z \in \Omega \\ d(x,y,z,\partial\Omega), & \text{for } x,y,z \notin \Omega \end{cases}, \tag{2.7}$$

where x, y and z are coordinates in three dimensional space, f is the signed distance function, d is the design function, in this case determines what the 3D structure will look like in a region Ω with boundary $\partial\Omega$. An interesting characteristic of the design function is that it is run parallel for every pixel, thus each pixel output is independent.

Two open cell geometries were created using the described method. The first is an aluminum tetradecahedron (polygon with faces consisting of 6 squares, 8 hexagons) lattice with triangular struts. The design was created by defining 12 vectors and using a strut sub-function to define triangular strut regions along each vector. Next, a blending function was used to merge and smooth nodes where two struts met, Finally, symmetry and mirrored planes were exploited to create a pattern of cells. The second geometry is a copper Schwarz P geometrical surface [25], given by

$$\cos(\omega x) + \cos(\omega y) + \cos(\omega z) = 0 \tag{2.8}$$

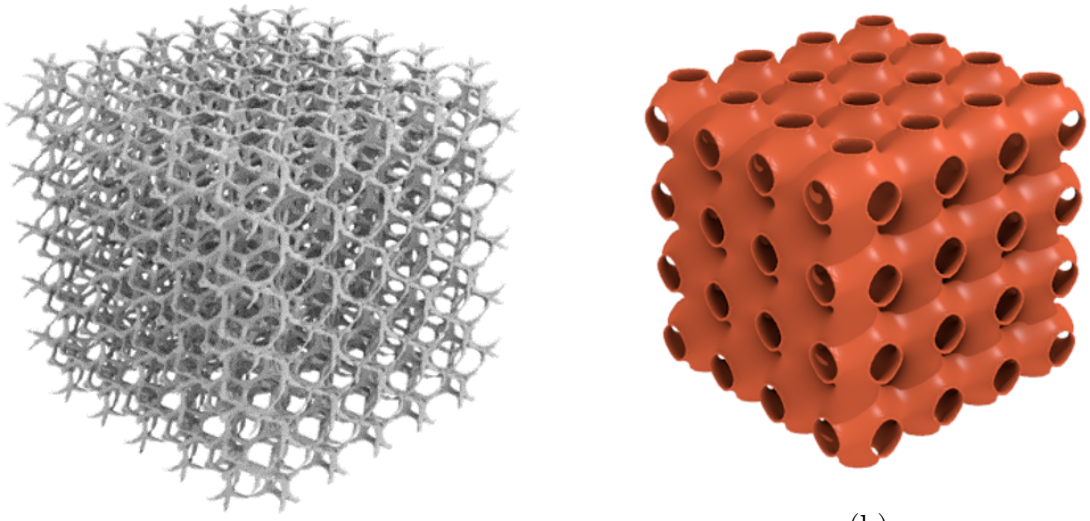

(a) (b)

Figure 2·2: Metallic foam structures designed using F3 software (a) an aluminum tetradecahedron lattice and (b) a copper Schwarz P surface.

This structure is one of a number of minimal geometrical surfaces, which minimize a surface area constraint with respect to volume. Both foams are shown in Figure 2·2.

Finite Element Analysis and Homogenization

Designs from F3 were exported as STL files and imported into MATLAB. Tetrahedral volume mesh generation was accomplished using iso2mesh [26], a free MATLAB mesh generation toolbox. The meshes were imported into Abaqus for finite element analysis. Both models were approximately cubes with a side length of 25.4 mm. In Abaqus, the material properties of aluminum and copper were created and assigned to both model elements, respectively. To determine effective material properties, six strain loading scenarios were imposed on the model (three in tension and three in compression, Figure 2·3) using the Abaqus Micromechanics Plugin.

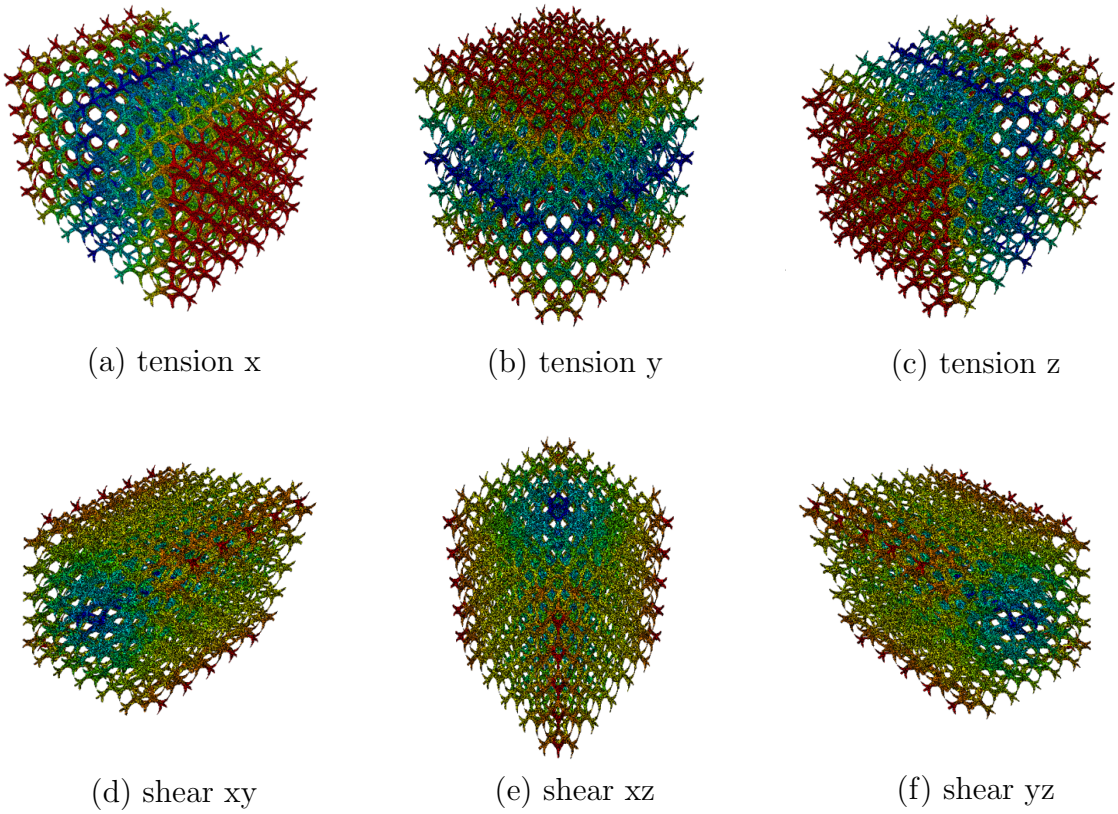

(a) tension x (b) tension y (c) tension z

(d) shear xy (e) shear xz (f) shear yz

Figure 2·3: Finite element loading scenarios for the tetradecahedron lattice. Color is normalized displacement (blue is zero, red is max).

The general form of Hooke's Law for a linear-elastic material written in Voigt notation is

$$\begin{bmatrix} \sigma_{11} \\ \sigma_{22} \\ \sigma_{33} \\ \sigma_{12} \\ \sigma_{13} \\ \sigma_{23} \end{bmatrix} = \begin{bmatrix} C_{11} & C_{12} & C_{13} & C_{14} & C_{15} & C_{16} \\ C_{21} & C_{22} & C_{23} & C_{24} & C_{25} & C_{26} \\ C_{31} & C_{32} & C_{33} & C_{34} & C_{35} & C_{36} \\ C_{41} & C_{42} & C_{43} & C_{44} & C_{45} & C_{46} \\ C_{51} & C_{52} & C_{53} & C_{54} & C_{55} & C_{56} \\ C_{61} & C_{62} & C_{63} & C_{64} & C_{65} & C_{66} \end{bmatrix} \begin{bmatrix} \varepsilon_{11} \\ \varepsilon_{22} \\ \varepsilon_{33} \\ 2\varepsilon_{12} \\ 2\varepsilon_{13} \\ 2\varepsilon_{23} \end{bmatrix}. \tag{2.9}$$

Each strain loading scenario isolates one column of the stiffness matrix, thus the stiffness matrix is determined column by column by solving for the volume averaged stress components for each load case.

An orthotropic material model can then be written by inverting the stiffness ma-

trix,

$$C_{ortho} = \begin{bmatrix} \frac{1}{E_1} & \frac{-\upsilon_{21}}{E_2} & \frac{-\upsilon_{31}}{E_3} & 0 & 0 & 0 \\ \frac{-\upsilon_{12}}{E_1} & \frac{1}{E_2} & \frac{-\upsilon_{32}}{E_3} & 0 & 0 & 0 \\ \frac{-\upsilon_{13}}{E_1} & \frac{-\upsilon_{23}}{E_2} & \frac{1}{E_3} & 0 & 0 & 0 \\ 0 & 0 & 0 & \frac{1}{G_{12}} & 0 & 0 \\ 0 & 0 & 0 & 0 & \frac{1}{G_{13}} & 0 \\ 0 & 0 & 0 & 0 & 0 & \frac{1}{G_{23}} \end{bmatrix}. \tag{2.10}$$

Finally, isotropic material properties were computed by an iterative least-squares method to find an elastic modulus and Poisson ratio which most closely matches the orthotropic compliance to the isotropic compliance matrix.

$$C_{iso} = \begin{bmatrix} \frac{1}{E} & \frac{-\upsilon}{E} & \frac{-\upsilon}{E} & 0 & 0 & 0 \\ \frac{-\upsilon}{E} & \frac{1}{E} & \frac{-\upsilon}{E} & 0 & 0 & 0 \\ \frac{-\upsilon}{E} & \frac{-\upsilon}{E} & \frac{1}{E} & 0 & 0 & 0 \\ 0 & 0 & 0 & \frac{1}{G} & 0 & 0 \\ 0 & 0 & 0 & 0 & \frac{1}{G} & 0 \\ 0 & 0 & 0 & 0 & 0 & \frac{1}{G} \end{bmatrix} \tag{2.11}$$

For the structures presented in this section, due to the periodic unit cell pattern, an isotropic material model is appropriate, however in general this may not be true.

2.1.3 Results

For each of the two structures, the relative density was altered by keeping the pore spacing (the distance between void openings in the surface) constant and increasing the thickness of material. Multiple structures of relative densities between 0 and 0.5

were designed in F3, meshed in MATLAB, analyzed in Abaqus, and homogenized with the procedure previously. Figure 2·4 shows the isotropic relative elastic modulus and Poission ratio versus relative density for the aluminum lattice. Similarly, Fig 2·5 shows the same property curves for the copper structure. Additionally, each curve is fit with a quadratic function of relative density.

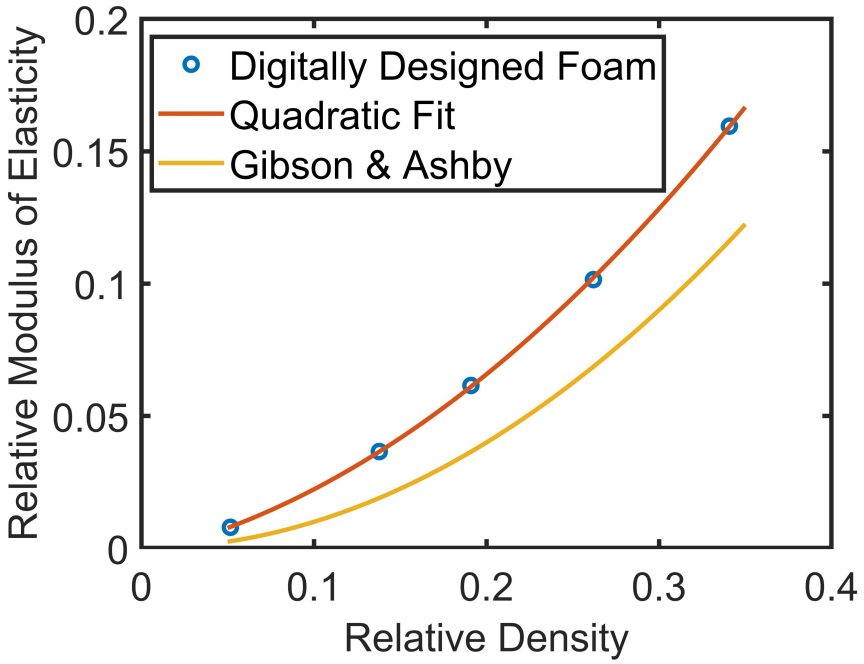

(a)

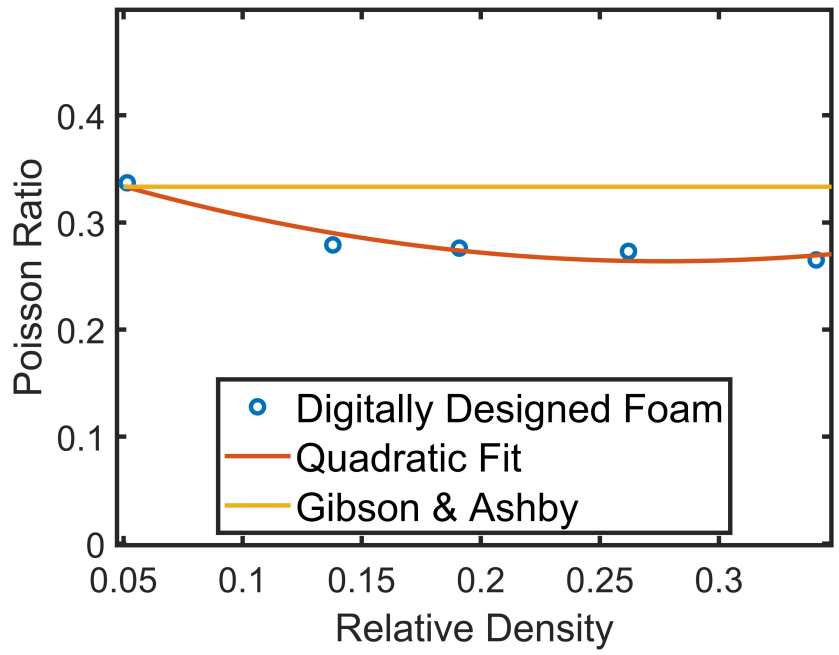

(b)

Figure 2·4: Material property curves for the Aluminum tetradecahedron lattice including (a) relative modulus and (b) Poisson ratio.

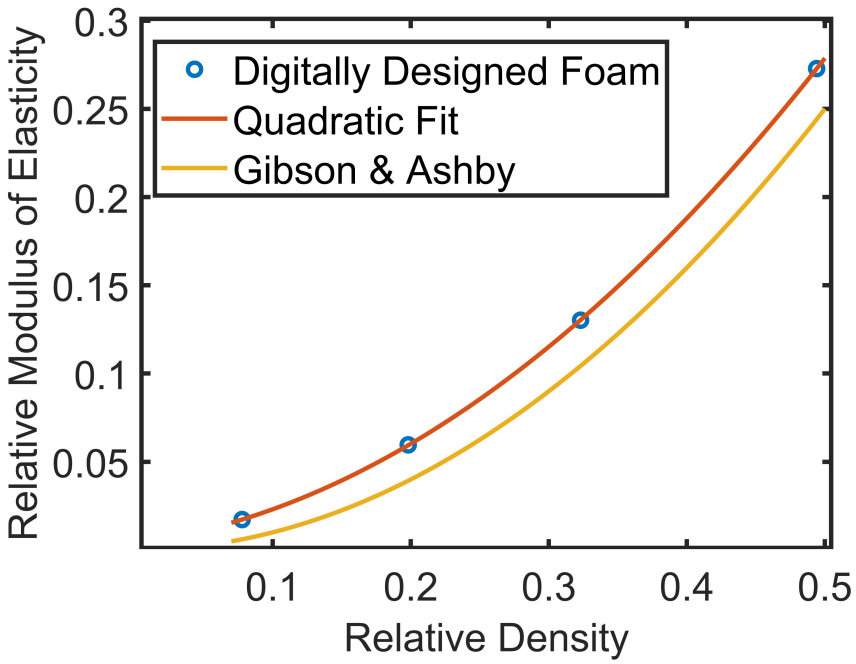

(a)

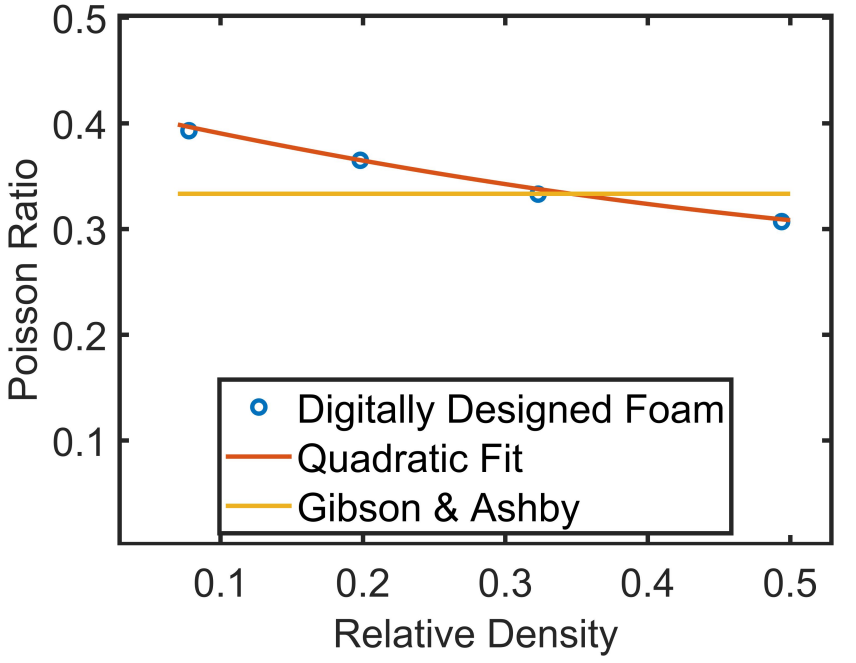

(b)

Figure 2·5: Material property curves for the copper Schwarz P structure including (a) relative modulus and (b) Poisson ratio.

2.1.4 Discussion

For both structures, material properties are found to have a good fit to a quadratic function of relative density in the form

$$E_f/E_s = A_1(\rho_f/\rho_s)^2 + A_2(\rho_f/\rho_s) + A_3, \tag{2.12}$$

and

$$\nu_f = A_4(\rho_f/\rho_s)^2 + A_5(\rho_f/\rho_s) + A_6, \tag{2.13}$$

where the A_i terms are the fitted constants. Table 2.1 shows the values of the constants for both structures. The Gibson and Ashby model (see Equation 2.3) only has a squared term in the fit for modulus of elasticity. There are, however, a number of assumptions with their model. First the derivation is only based on bending arguments. One advantage to using FEA is that it can capture effects of combined bending torsion, and compression, especially at higher relative densities where compression may begin to dominate. For Poisson ratio, the Gibson and Ashby trend is constant (see Equation 2.6) however there is large scatter in experimental data [5] due to inherent difficulty in measuring Poisson ratio. The FEA results suggest that Poisson ratio is (although not strongly) a function of relative density.

2.1.5 Conclusion

Concepts for digitally designing metallic foams were described using a computer graphics approach. Finite element software was used to analyze the designed microstructures. Isotropic homogenization was done to characterize static material properties including elastic modulus and Poisson ratio. Material properties were discussed in line with existing theory for cellular solids and were found to be a strong function of relative density. Material design curves, like the ones generated by the discussed approach, are advantageous for designers, because they enable visualization

Table 2.1: Material property coefficients for the tetradecahedron and Schwarz P structures

	tetradecahedron	Schwarz P
A_1	0.954	0.893
A_2	0.149	0.104
A_3	-0.002	0.004
A_4	1.358	0.173
A_5	-0.753	-0.309
A_6	0.368	0.420

of the design space and availability of material properties. Such foams can then be fabricated and implemented to serve a wide range of structural applications.

2.2 Additive and Subtractive Digital Designs

This section describes additional concepts for digitally designing cellular solids, and demonstrates the ability of this design method for tuning effective material properties. A design is presented which has orthotropic material properties, including a negative Poisson ratio in one direction. Additionally to demonstrate the usefulness of the described method, several designs of varying relative density were 3D printed from PLA and compression tested using an Instron load cell. Comparisons between load cell data and numerical analysis were made for validation.

2.2.1 Introduction

Digital designs of microstructures are presented and then analyzed with finite element software to determine effective material properties. Digital designs are split into two groups, based on suitable manufacturing method. Subtractive models describe a foam that could be created by CNC machining a specified pattern from a solid section.

Additive models describe foams that could be fabricated from a 3D printing process. The relationship between mass properties and effective static material properties (such as elastic modulus and Poisson ratio) of cellular solids will be discussed for the digital designs, with reference to existing theory. The same method for meshing, FEA, and homogenization was used as described previously in Section 2.1.

2.2.2 Subtractive Model

A subtractive model was created by designed a slotted cut-out pattern into a 50.8 mm x 50.8 mm x 50.8 mm block of aluminum (E = 69 GPa, ν = .33), as shown in Figure 2·6 (a).

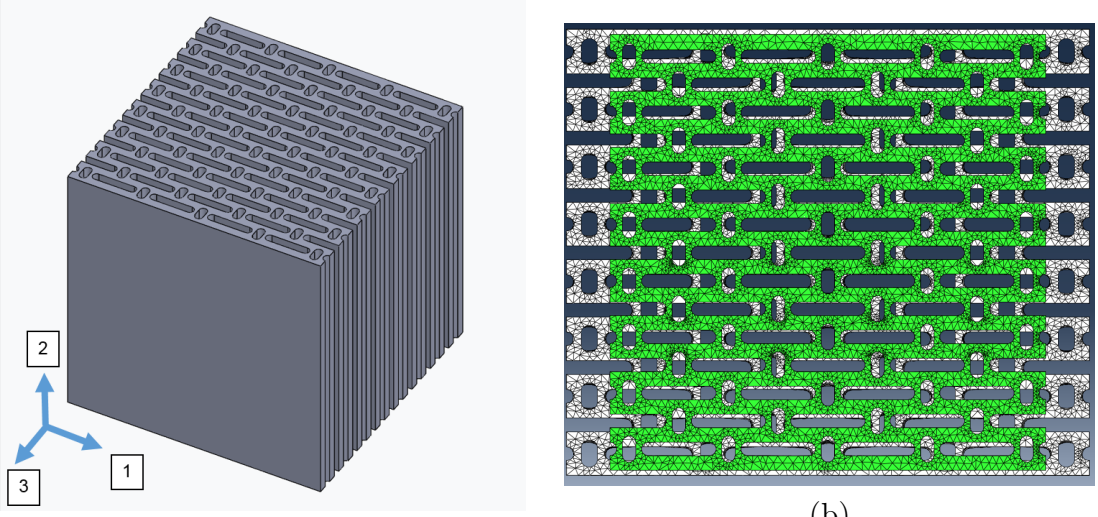

(a) (b)

Figure 2·6: (a) Geometry of the slotted cube subtractive model and (b) deformation profile (in white) for lateral extension of the slotted cube (green)

The pattern is unique due to the orientation and size of the slots. When extended laterally, the smaller slots tend to become rounder, due to stretching. This, in turn, widens the longer slots which leads to an extension in the lateral direction. This is represented in Figure 2·6 (b). The slotted cellular structure was fit to an orthotropic

Table 2.2: Orthotropic material properties including elastic modulus, shear modulus, and Poisson ratio for the digitally designed slotted cube.

E_1 (MPa)	E_2 (MPa)	E_3 (MPa)
30129	38178	4735
ν_{12}	ν_{13}	ν_{23}
0.2604	-0.1159	0.3300
G_{12} (MPa)	G_{13} (MPa)	G_{23} (MPa)
12050	3656	4532

material model and the resulting properties are shown below in Table 2.2. From the table, it is seen that the 2 direction is the stiffest for this material, corresponding to the direction along the length of the drilled out slots. In the 1-3 direction, the Poisson ratio is -0.1159, a result that is unique to this design.

2.2.3 Additive Model

An additive model was constructed by creating an octahedral lattice with round cross sectional area struts. In order to do a parametric study, six different iterations of this structure were designed by keeping strut spacing constant and varying strut diameter. The microstructure for the most dense structure (relative density equal to 0.42) is shown in Figure 2·7. Finite element analysis was used to predict the elastic modulus and Poisson ratio. The results will be discussed in section 2.2.5.

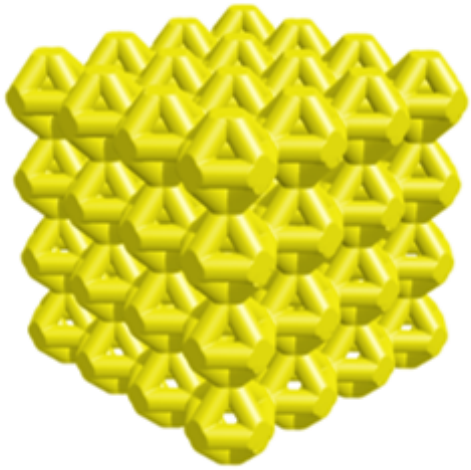

Figure 2·7: Digital design of a foam constructed from an octahedral lattice, relative density equal to 0.42.

2.2.4 Experimental Results

Experimental efforts were focused on measuring elastic modulus for the octahedral lattice. Five distinct octahedral geometries were 3D printed from PLA. Relative density was calculated by weighing the samples and measuring the length dimensions to calculate volume. To estimate Young's modulus, force and axial displacement were measured by the Instron load cell during a compression test with a rate of 0.1 mm/s. Test were manually stopped after yield point. An average stress was calculated assuming the force acted over the entire area of the structure. Likewise, an average strain was calculated over the length of the structure.

There is a distinct linear regime from which the elastic modulus can be calculated prior to yielding. This was done for all 3D printed structures. Lastly, one final test was done. A dogbone shaped sample was 3D printed in the same manner from PLA. This sample was tested in tension to get an estimate of the elastic modulus of 3D printed, layered PLA. The value measured was $E_{PLA} = 2038$ MPa, and was used to

calculate relative elastic modulus for comparison to numerical and analytical results.

2.2.5 Discussion

The most well known theory relating effective mass properties to mechanical properties of cellular solids is the Gibson and Ashby model [5] (see Equations 2.3 and 2.6. In Figure 2·8 the Gibson and Ashby model is plotted along side the numerical and experimental data for the octahedral lattice.

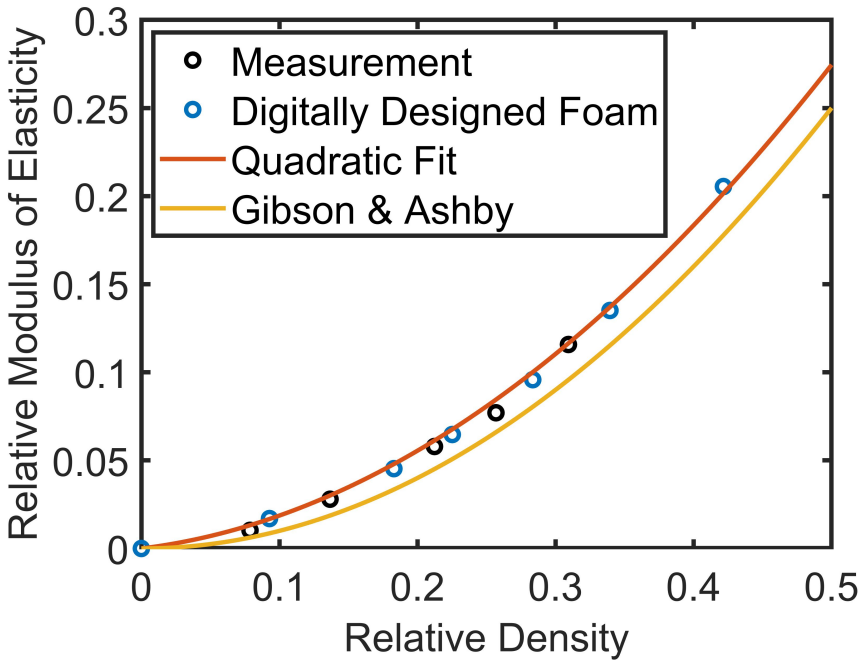

(a)

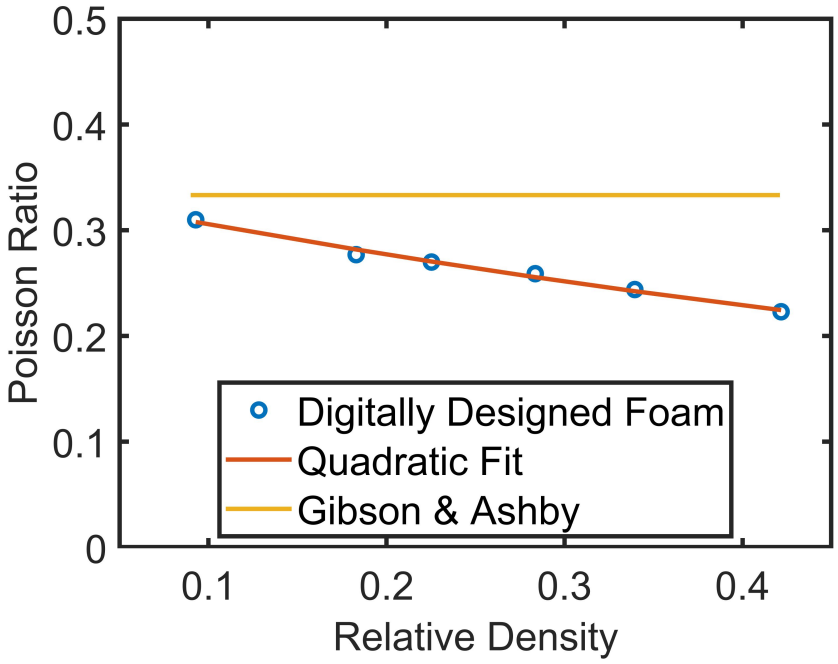

(b)

Figure 2·8: Material property curves for the octahedral lattice including (a) elastic modulus and (b) Poisson ratio.

Both the numerical and experimental points fit quite well to a quadratic fit below. It is seen that there is a noticeable offset from the Gibson and Ashby model.

$$E_f/E_s = 0.9052(\rho_f/\rho_s)^2 + 0.0964(\rho_f/\rho_s). \tag{2.14}$$

Additionally the Poisson ratio was seen to fit a quadratic function of relative density of the following form

$$\nu_s = 0.147(\rho_f/\rho_s)^2 - 0.329(\rho_f/\rho_s) + 0.337. \tag{2.15}$$

These trends agree with the previously reported results discussed in Section 2.1.4 and are also confirmed experimentally for elastic modulus. Overall, the Gibson and Ashby trends give correct order of magnitude of agreement for elastic properties of digitally designed foams. There are some structural dependent deformation mechanisms that can be more accurately captured with a full quadratic fit to relative density.

2.2.6 Conclusion

Subtractive and additive models were used to design various cellular structures. Design curves were generated by finite element analysis and compared with experimental measurements and analytical scaling laws. The methods presented in this section can be used to design structures with tunable stiffness and mass properties which can be fabricated for use in sound and vibration applications.

2.3 Commerically Available Metallic Foams

The previous focus of this chapter has been on digital designs of microstructures. There are, however a wide range of commercially available metallic foam with randomized porous microstructures. In this section examples of such foams are investigated.

2.3.1 Introduction

In the literature there are many examples of compression tests of commercial foams in order to estimate the stiffness. A common foam is Duocel aluminum foam, for which some results from the literature [27–32] are reported in Figure 2·9.

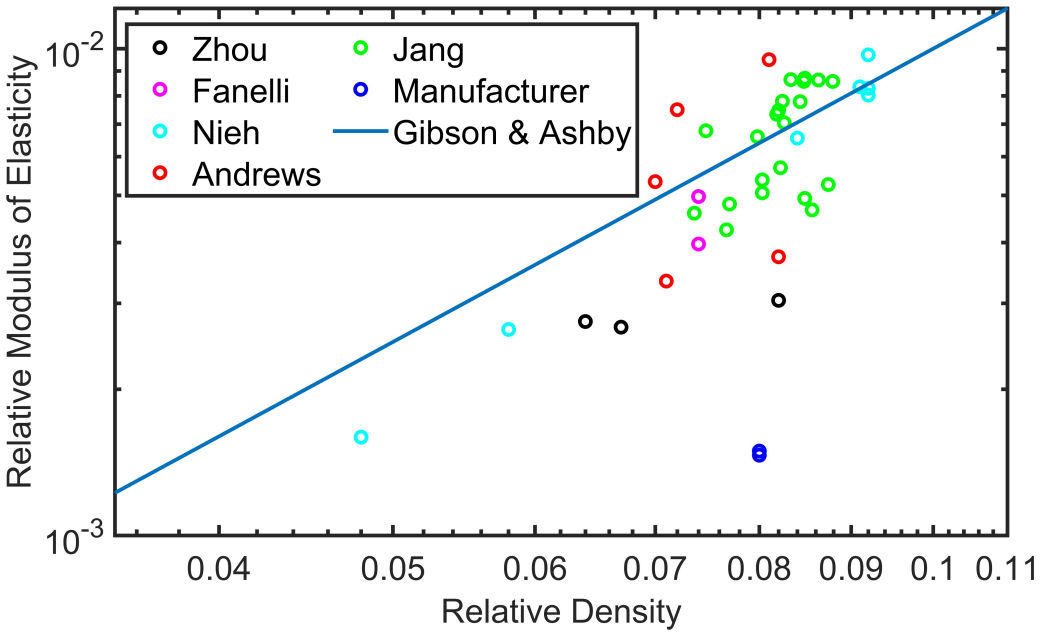

Figure 2·9: Overlay of Gibson and Ashby theory with experimental measurements from the literature of elastic modulus for Duocel aluminum foam. The Gibson & Ashby curve is given by Equation 2.3 (relative quantities are normalized by the properties of the solid material)

Reports of the stiffness for this foam loosely agree with the Gibson scaling laws, however they do span nearly an order of magnitude for relative density near 0.08. This variation in measurements could be due to a number of assumptions. Foams with with the same relative density may have different pore sizes. This is not captured by the Gibson model nor explored in depth in any of the previously cited literature. Secondly, the direction of compression is important to consider, and was not noted in the previous studies. The Duocel foams are hypothesized to be slightly anisotropic

due to the curing direction of the foam in manufacturing. Gravity is thought to slightly elongate pores in one direction [33].

A second microstructure property that results from manufacturing processes is the strut fill density. Duocel foams are known to have completely dense (solid) struts, however this is not true for all metal foams. For example, some foams manufactured by deposition techniques [34, 35], result in hollow struts. One such manufacturer is Nanoshel. A comparison of micro-CT scan images for solid and hollow strut foams is shown in Figure 2·10.

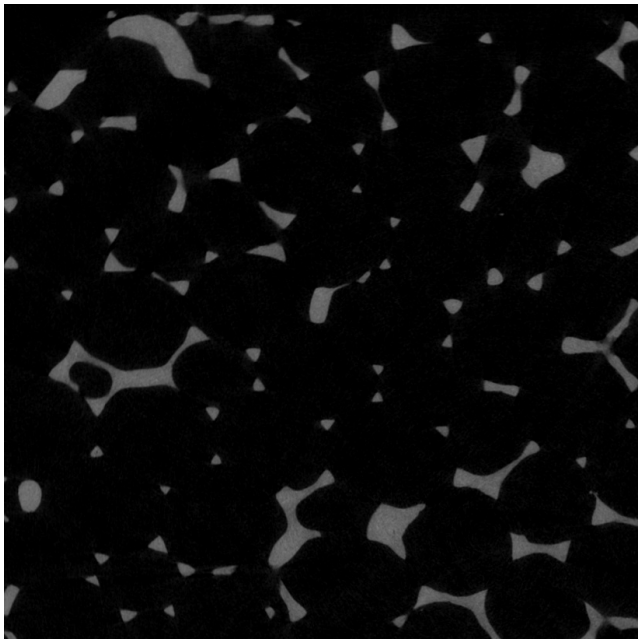

(a)

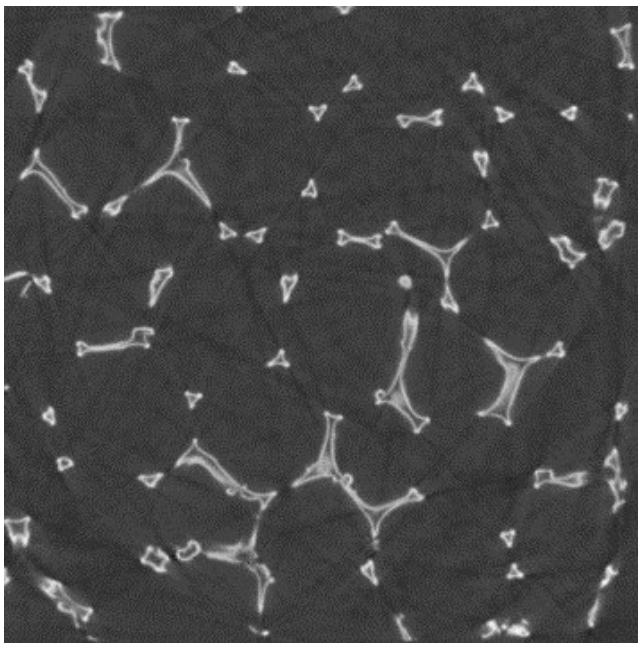

(b)

Figure 2·10: Micro-CT scans for (a) solid strut aluminum foam (Duocel), (b) hollow strut copper foam (Nanoshel). The brighter gray regions are the solid metal and the black is the void space.

2.3.2 Finite Element Analysis Results

An array of commercially available metallic foams were cut into approximately 25.4 mm cubes and micro-CT scanned at Boston University. The foams studied were from 2 different manufactures (ERG and Nanoshel), consisted of 3 different materials (copper, aluminum, and nickel), and had pore sizes varying from 20 PPI to approximately 80 PPI. The microstructures can be seen in Figure 2·11 (c). Three dimensional finite element models were constructed from the micro-CT scan images using the commercial software Simpleware ScanIP. For the Duocel foams, a tetrahedral mesh was created and for the Nanoshel foams, a surface mesh of triangular elements was created. A thickness was prescribed to the triangular shell elements that was a mean thickness estimated from the images using ImageJ. The directionally dependent elastic modulus and Poisson ratios were computed in Abaqus as described in Section 2.2.

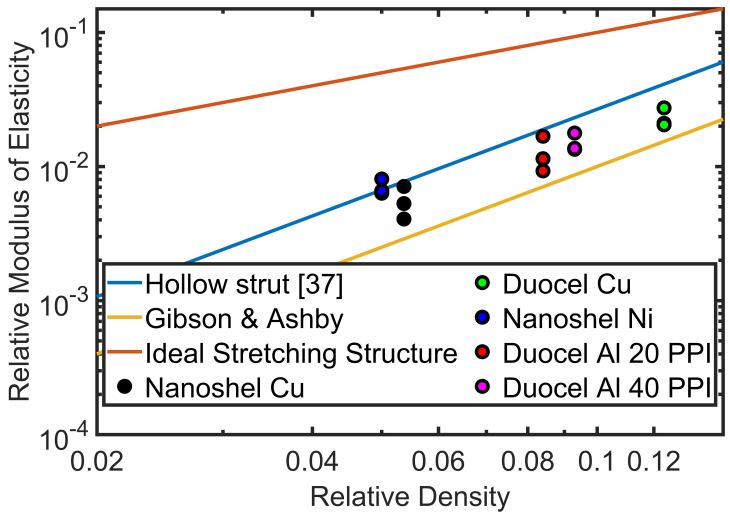

(a)

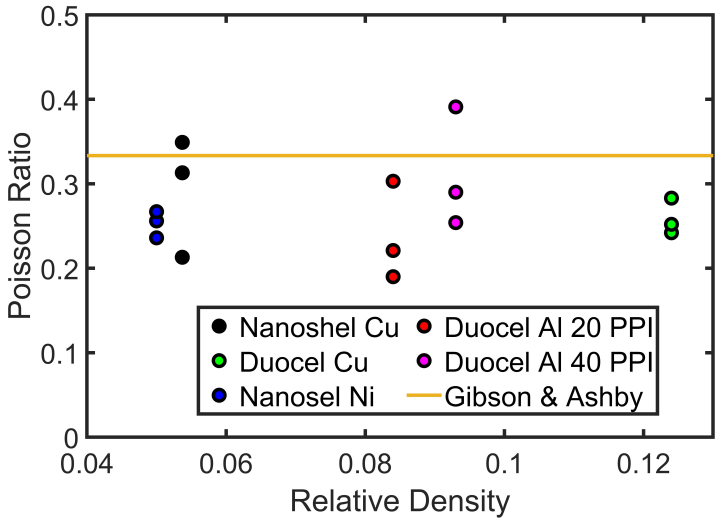

(b)

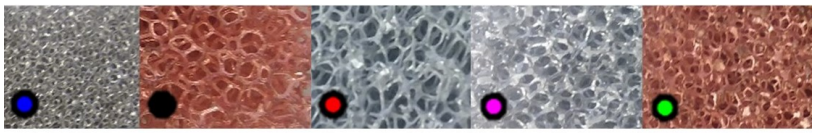

(c)

Figure 2·11: (a) relative elastic modulus versus relative density, (b) Poisson ratio versus relative density, and (c) microstructure of the five different commercially available metallic foams.

The results are shown in Figure 2·11. Plotted in Figure 2·11 (a) are a few additional scaling curves. The ideal stretching structure is one whose stiffness scales with relative density to the first power [36]. Foams with hollow struts have have also been shown to be more efficient in terms of stiffness-to-weight ratio (having a higher relative modulus for the same relative density) [37], [38]. For hollow strut foams, C_1 in Equation 2.3 is not equal to one, but can be estimated from the thickness and size of the hollow strut cross section. Using the methodology in [37] and approximate measurements from micro-CT images, the estimated stiffness constant was $C_1 = 2.67$. It is noticed that for most of the 5 foams, at least one direction is stiffer than the other two, suggesting that direction-ability is important. In Figure 2·11 (b), the Poisson ratio is directionally dependent, ranging between approximately 0.2-0.4. Poisson ratio for most open-cell foams has been reported to be near 0.33 [5].

2.3.3 Conclusion

In this section, finite element analysis of commercially available metallic foams was described which yielded estimates of static mechanical properties such as elastic modulus and Poisson ratio. From the analysis, the properties appeared to be directionally dependent. The manufacturing process of the foam can highly influence the mechanical properties, both by effects of gravity and by changing the strut density.

Chapter 3

Acoustic and Bulk Mechanical Properties of Metallic Foam after Triaxial Hydrostatic Compression

3.1 Acoustic Absorption by Metallic Foam after Triaxial Hydrostatic Compression

In this chapter, an engineering method for triaxial hydrostatic compression of metallic foam is presented to preferentially alter the foam's microstructure. The method is demonstrated on an assortment of open-cell aluminum foams with varying pore size and porosity. Measurements of acoustic absorption indicate that the compressed samples absorb significantly more sound than the conventional samples of equal thickness in the test range from 0.25 – 4.5 kHz. An analysis is presented which links the microstructure properties of compressed foam samples to conventional samples, thereby providing a means to estimate acoustic absorption trends for compressed samples through use of existing models.

3.1.1 Introduction

The engineering design specification for stiff and lightweight materials has led to the development of many types of composites and cellular structures, including metallic foams. Metallic foams consist of interconnected metal regions surrounded by large volume fractions of air. As engineering materials, they have many attractive proper-

ties including a linear elastic small strain response that arises from the microstructure [29], ductility from the host metal [32], and high energy absorption capability due to plastic collapse [30]. Currently in an effort to provide designers with an expansive materials database, many fabrication methods and engineering methods are being researched to produce foams with tunable bulk mechanical properties.

In this section, an engineering method for triaxial, plastic compression of metallic foam using hydrostatic pressure is proposed and demonstrated to preferentially alter the foam's microstructure and porosity. The proposed method can provide simultaneous compression from three orthogonal directions and mitigates the effects of shear deformation which can result from existing methods. The method is a post-manufacturing process for metallic foams that can be used to create foams with properties unable to be manufactured otherwise. For example, some manufacturers of metallic foams are limited in production of foams with small pore sizes; this method can decrease the pore size of existing foams. Additionally, the local yielding of metal struts creates a spatial variation in modulus within the foam, resulting in foams whose bulk elastic properties do not scale with conventional scaling laws for open-cell foams. Furthermore, the compression produces a foam with a re-entrant pore shape.

The acoustic absorbing properties of an array of conventional and compressed foams were measured in an impedance tube using a standard method. The acoustic absorption of the metal foam was significantly higher for all compressed samples over the measured frequency range (0.25 – 4.5 kHz). Acoustic absorption increased with increasing compression ratio up to the maximum compression ratio tested (approximately 2). Finite element analysis is used to predict changes in the foam's microstructure with increasing volumetric compression ratio for a 3D unit pore for both conventional and compressed configurations. The results from this analysis are

then used along with an existing model to predict the acoustic absorption of the compressed samples.

Traditionally, metallic foams have been plastically compressed by the vise method [8]. In this method, a vise was fit with plexiglass platens covered with sandpaper (to prevent sliding) and required incremental small applications of strain. This method has been used by researchers to transform the pore structure into a re-entrant shape [9], [33]. Additionally due the metal plasticity, plastic hinges are formed at regions of high stress. For the previously cited references, the combination of these two effects has lead to a measurable negative Poisson ratio for some metallic foams. The drawbacks of the vise method are, however, that it is time consuming, only one dimension is typically strained at a time, it requires high manual force for large samples, and the compression can result in undesired shear deformation.

The hydrostatic loading of foams has typically been done in order to study the properties of the material that change with volume, for example the bulk modulus. Moore et al. [39] developed a test method for hydrostatic compression of an open-cell polyurethane foam. Viot [40] utilized high speed imaging and image processing techniques to study the hydrostatic deformation of a closed cell polypropylene foam. Deshpande and Fleck [41] designed a testing apparatus for sealing a metallic foam undergoing hydrostatic loading that consisted of shims, wedges, and a rubber membrane. This apparatus was designed for cylindrical samples and enabled the applications of a uni-axial load superimposed upon a hydrostatic pressure.

The acoustic performance of metallic foams depends highly on the microstructure. The acoustic losses arise from thermal and viscous boundary layer effects near the interface of the air and the metal. For acoustic excitation in air, metallic foams can be considered rigid due to the high stiffness of the metal compared to air [1]. Overall, closed-cell metallic foams tend to be poorer sound absorbers in air than open-cell, but

have been improved by rolling and hole drilling processes [21]. Sound absorption and one-dimensional compression of a porous nickel-iron alloy was studied experimentally by Bai et al. [42]. They found an optimal compression ratio of 70% to maximize sound absorption (in one direction) between 1-6 kHz for a sample with an initial porosity of 0.75. A subsequent effort [43] improved sound absorption through spark-erosion drilling to create microperforations in the foam.

One of the most widely used methods for estimating acoustical indicators of rigid-framed, porous materials is based on modeling of the foams' microstructure properties [20]. These properties (such as porosity, tortuosity, flow resistivity, viscous characteristic length, and thermal characteristic length) can then be employed in an effective fluid homogenization model. One of the most predominant, five parameter models is the Johnson-Champoux-Allard model [44], [45]. Other methods for estimating acoustic absorption can be used without the need for determining any intermediate variables if the geometry of the foam is known and the acoustic boundary layers are small compared to foam geometry [46].

In the next section, the materials and methods are described for the hydrostatic and acoustic experiments. In Section 3.1.3 the background theoretical and numerical work is outlined for modeling and predicting the acoustic absorption of the conventional and compressed metallic foam samples. In Section 3.1.4, the modeling results are presented and discussed and lastly the conclusion is Section 3.1.5.

3.1.2 Materials, Methods, and Measurements

Hydrostatic Testing

Open-cell aluminum foams samples (50.8 x 50.8 x 63.5 mm) from ERG Aerospace Corporation were obtained for this study. To promote uniform pressure loading, the samples were specially prepared and sealed as shown in Figure 3·1. First the

foam was placed into a set of 3D printed compression fixtures, which acted as corner guides for compression. They were also designed to limit the compression by coming into self contact after a desired compression ratio. Next a compressible foam board approximately 6.35 mm thick was used to enclose the entire sample. Finally, the assembly was placed in an elastic sealing layer that was tied shut.

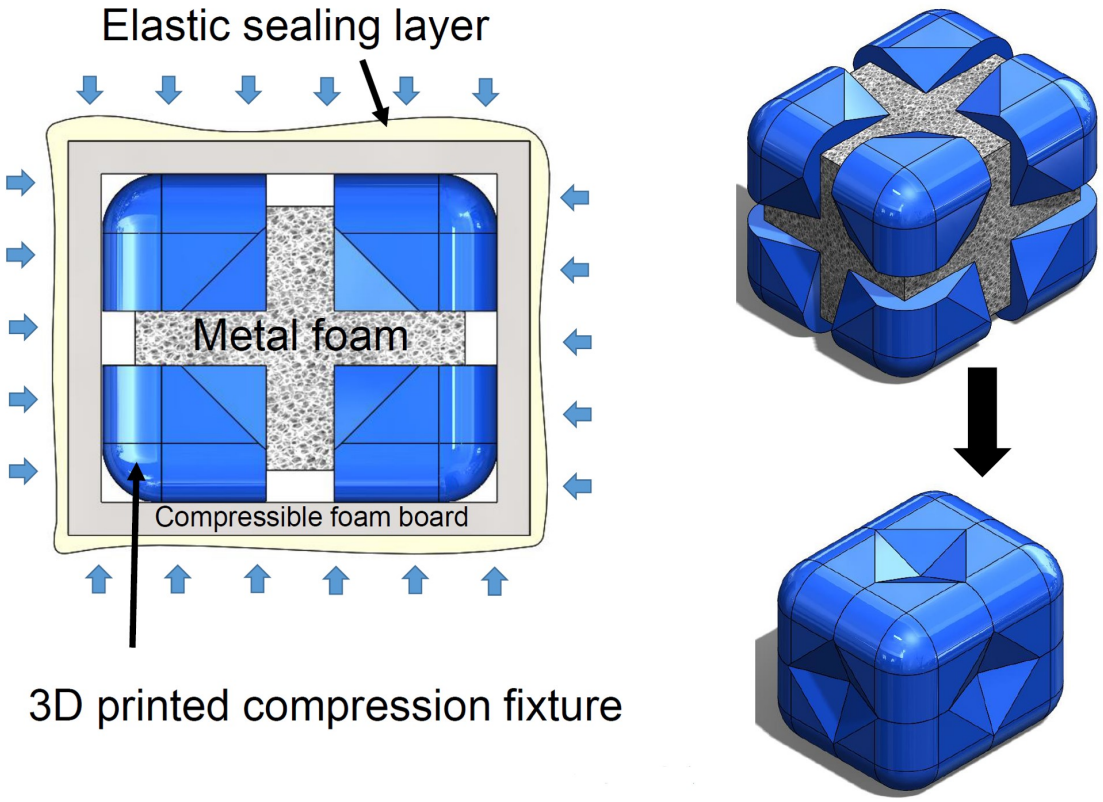

Figure 3·1: Preparation of metal foam sample for hydrostatic pressure tests.

The hydrostatic pressure apparatus is shown in Figure 3·2. A hand pump, pressure guage, and steel pressure vessel were connected inline with a water supply. For compression, the samples were placed in the vessel and the cap was bolted on. The water supply was turned on and air was bled from the system by opening a union near the top of the cap. Once the air was removed, the union was closed and pressure was increased through pumping. Once the desired pressure was reached, the union

was carefully opened to release pressure.

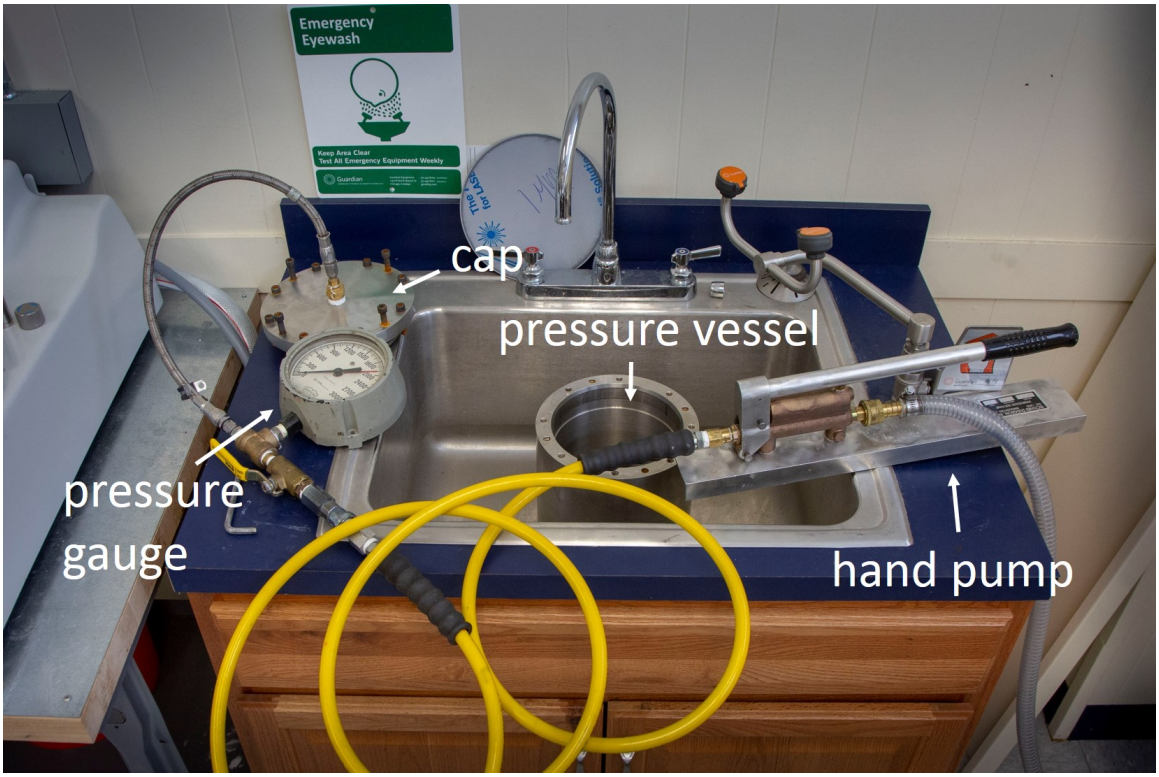

Figure 3·2: Experimental apparatus used for compression of metallic foam.

An array of 6 foams of varying porosity and pores per inch (PPI) were compressed through this method. It was found that in order to best maintain uniform deformation and preserve shape homogeneity, multiple sets of 3D printed fixtures were used consecutively on samples, including sets designed for volumetric compression ratios of 1.5, 2, and 3. Figure 5·22 shows 5 PPI foams with multiple compression ratios. A summary of all samples compressed is shown in Table 3.1 along with the maximum applied pressure.

(a) (b) (c)

Figure 3·3: 5 PPI aluminum foam samples, 10% nominal relative density and insets of the same samples after electrical discharge machining for (a) nominal sample and samples with compression ratios of approximately (b) 1.45 and (c) 1.90.

The volumetric compression ratio was measured two ways. First the volumetric compression ratio was computed as the ratio of the intial bulk volume to the final bulk volume. Due to sample's shape after compression (in some cases the middle faces of the samples tended to deform more than the edges), an uncertainty of $\pm$ 7% was estimated for compression ratio based on $\pm$ 1 mm measurement of edge lengths for a sample of volumetric compression ratio of 2. Secondly, the volumetric compression ratio was computed as the ratio of final relative density (after compression and machining) to initial relative density. This assumes the volume of aluminum remains unchanged during compression.

Results for the methods are plotted in Figure 3·4. Data for volume compression ratio equal to 1 is included to show measured deviation of relative density for the same sample before and after machining (no compression). Since the foams are random structures, this variation in measurement (greater than 7% for 40 PPI) indicates that the relative density is spatially dependent. For the 20 and 40 PPI foams, compression ratio measured both ways agrees within the 7% error bars. For 5 PPI foams, the

Table 3.1: Summary of hydrostatically compressed aluminum foam samples.

Sample	PPI	Initial Void Fraction	Final Void Fraction	Approximate Compression Ratio	Maximum Pressure (MPa)
1	5	0.901	0.901	-	-
2	5	0.893	0.825	1.45	5.17
3	5	0.892	0.770	1.9	6.89
4	20	0.881	0.881	-	-
5	20	0.867	0.802	1.42	5.17
6	20	0.867	0.738	1.84	6.89
7	40	0.922	0.922	-	-
8	40	0.918	0.870	1.51	3.44
9	40	0.917	0.822	1.97	4.83

compression ratio estimated by relative density measurements over predicts that measured by bulk volume. It was observed during hydrostatic compression experiments that 5 PPI foams were the most difficult to deform, required higher pressures, and had the largest amount of shape non-uniformity. This is attributed to the large pore size and large size (thickness and length) of the individual metal ligaments which required higher loading to deform. In Section 3.1.4, volume compression ratio in terms of bulk volume measurements and corresponding uncertainty are used to analyze the experimental data.

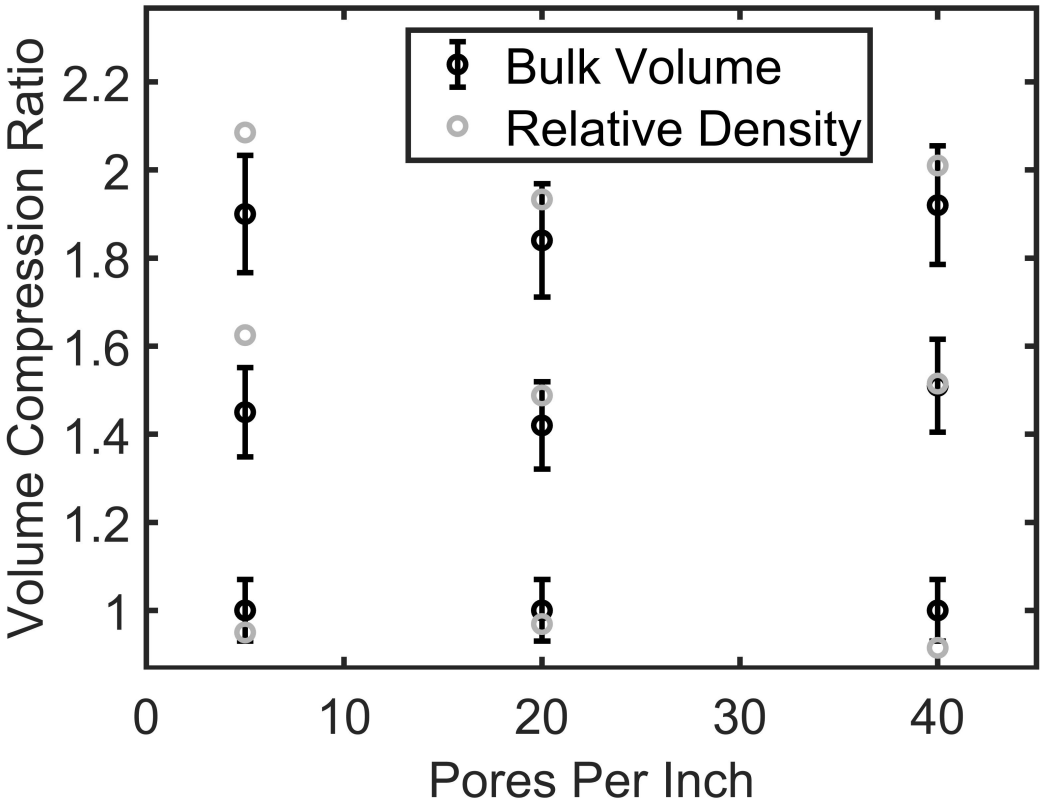

Figure 3·4: Comparison of volume compression ratio measurements based on bulk volume and relative density.

Acoustic Testing

In total, 9 samples were tested for acoustic absorption (6 compressed and 3 conventional samples) in an impedance tube at Acentech in Cambridge, MA. For testing, the samples were machined into cylinders with 34.9 mm outside diameter and 45.7 mm height using electrical discharge machining. Test were done using the two microphone method in accordance with ASTM Standard E1050-12 [47].

Each sample was tested multiple times (including after flipping end-for-end) with no appreciable difference in absorption measured between trials. The tube plunger was pushed flush with the specimen back such that there was no air cavity (sample

was rigidly backed). The frequency range for the tests was 0.25 – 4.50 kHz based on cutoff limits for the tube.

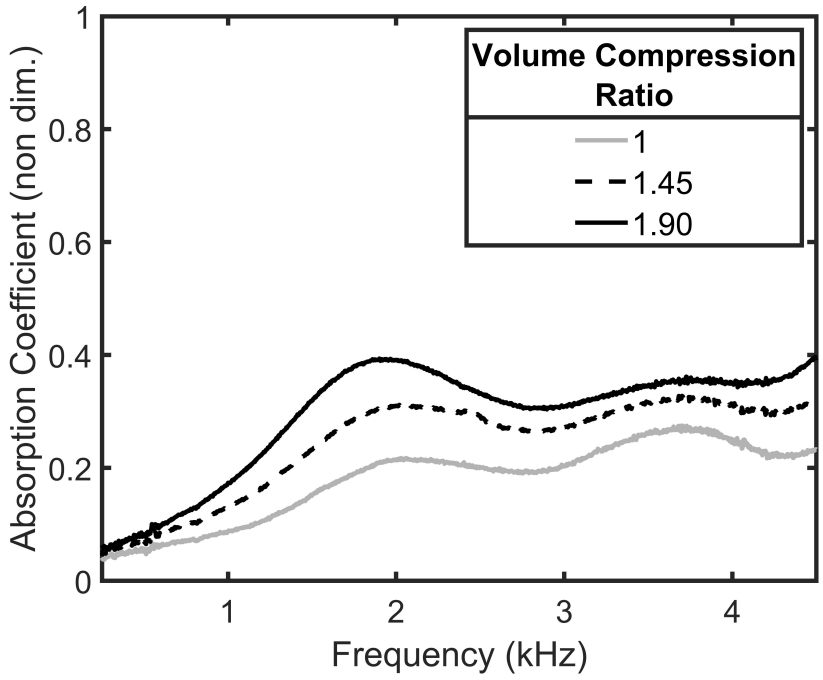
Volume Compression Ratio
1
1.45
1.90
Absorption Coefficient (non dim.)
Frequency (kHz)
0
0.2
0.4
0.6
0.8
1
2
3
4

(a)

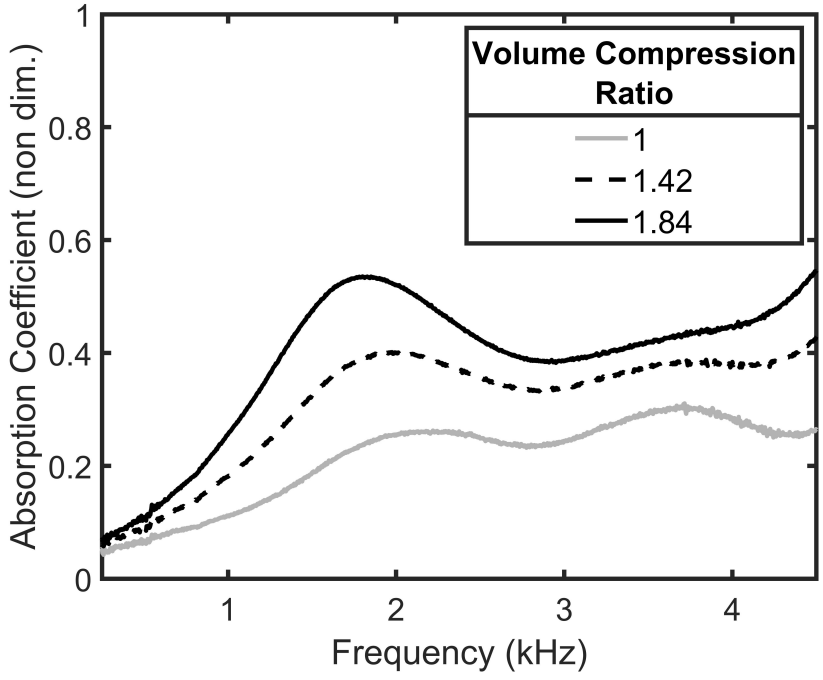
Volume Compression Ratio
1
1.42
1.84
Absorption Coefficient (non dim.)
Frequency (kHz)
0
0.2
0.4
0.6
0.8
1
2
3
4

(b)

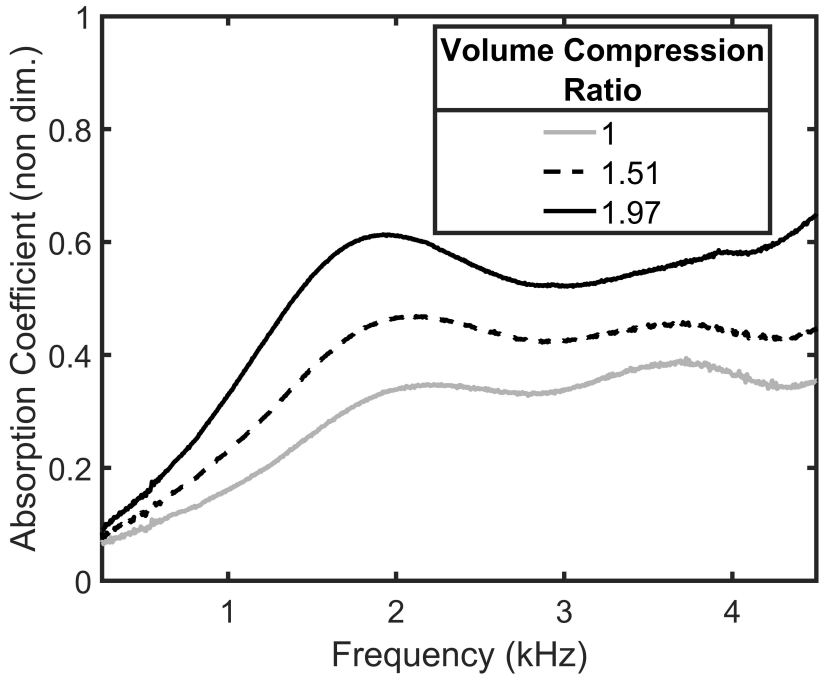

(c)

Figure 3·5: Normal incidence sound absorption coefficient measurements for metallic foam samples (a) 5 PPI, (b) 20 PPI, and (c) 40 PPI. All samples approximately 45 mm thick.

The measured results are in Figure 3·5. Comparing the conventional samples (compression ratio = 1) for the 5, 20, and 40 PPI samples, it can be seen that foams with increasing PPI have increased absorption. This has been noted elsewhere [46] and is largely attributed to increased specific surface area leading to increased boundary layer losses for larger PPI (smaller pore sizes). For all samples, absorption is increased with increasing compression ratio to approximately 2, the maximum compression ratio in this study. The 40 PPI sample with a compression ratio of 1.97 was the best absorber, which increased absorption by an average of 0.2 over the tested frequency range. This sample also had the smallest effective pore size after compression, which is also a smaller pore size than any aluminum foams currently

produced by the manufacturer.

3.1.3 Acoustic Modeling

Theoretical Background

A predominant model for acoustic propagation in rigid-framed porous media is the Johnson-Champoux-Allard [JCA] model [44], [45]. This model views the foam as an equivalent fluid that satisfies the Helmholtz equation

$$\nabla^2 p + k_{eq}^2 p = 0 \tag{3.1}$$

where $k_{eq} = \frac{\omega}{c_{eq}}$ is the homogenized wave number and the homogenized sound speed is $c_{eq} = \sqrt{K_{eq}/\rho_{eq}}$, written in terms of homogenized density and bulk modulus of the porous material.

According to the JCA model, expressions for frequency dependent, complex K_{eq} and ρ_{eq} can be written in terms of properties of the surrounding fluid as well as five foam microstructure parameters (porosity ϕ, flow resistivity σ, tortuosity α_∞, viscous characteristic length Λ, and thermal characteristic length Λ'). The two expressions are

$$\rho_{eq}(\omega) = \frac{\alpha_\infty \rho_0}{\phi}\left[1 + \frac{\sigma\phi}{j\omega\rho_0\alpha_\infty}\sqrt{1 + j\frac{4\alpha_\infty^2\eta\rho_0\omega}{\sigma^2\Lambda^2\phi^2}}\right] \tag{3.2}$$

$$K_{eq}(\omega) = \frac{\gamma P_0/\phi}{\gamma - (\gamma-1)\left[1 - j\frac{8\kappa}{\Lambda'^2 C_p\rho_0\omega}\sqrt{1 + j\frac{\Lambda'^2 C_p\rho_0\omega}{16\kappa}}\right]^{-1}} \tag{3.3}$$

The properties of the fluid surrounding the foam, air in this case, are density ($\rho_0 = 1.2\,\mathrm{kg/m^3}$), dynamic viscosity ($\eta = 18.18 \times 10^{-6}\,\mathrm{Pa\,s}$), specific heat ratio ($\gamma = 1.4$), thermal conductivity ($\kappa = 2.6 \times 10^{-2}\,\mathrm{W/(m\,K)}$), atmospheric pressure ($P_0 = 101.3\,\mathrm{kPa}$), and specific heat at constant pressure ($C_p = 1 \times 10^3\,\mathrm{J/(kg\,K)}$).

Extensions of the JCA model include the additional static thermal permeability

term introduced by Lafarge et al. [48] and two additional tortuosity terms introduced by Pride et al. [49]. In this work, the JCA is used for both conventional and compressed samples. The JCA model has been used previously for similar types of porous metals [50] and has the advantage of being a simpler model with fewer inputs.

To compute the acoustic absorption of a foam layer, first the impedance at the surface (with the foam rigidly backed) is computed by

$$Z_s = -iZ_{eq}\cot\left(k_{eq}L\right) \tag{3.4}$$

where $Z_{eq} = \rho_{eq}c_{eq}$ and L is the thickness of the layer. The reflection and absorption coefficients are

$$R = \frac{Z_s - Z_{air}}{Z_s + Z_{air}} \tag{3.5}$$

$$\alpha = 1 - |R|^2 \tag{3.6}$$

where Z_{air} is the characteristic impedance of air.

Conventional Samples

For the conventional samples, determination of the five foam microstructure parameters is necessary in order to predict the acoustic absorption. The porosity of the samples was taken as the measured value in Table 3.1. Additionally, flow resistivity measurements have been reported in the literature for ERG aluminum foams for 20 and 40 PPI of similar porosity as in this study [51], [52]. For 5 PPI, the flow resistivity was estimated based on additional trends reported for 10 PPI foams. Thus by assuming known porosity from measurements and flow resistivity from the literature, five unknowns are reduced to three. To determine the characteristic lengths as well as the tortuosity, the inverse method was used. A global optimization was implemented to minimize error between the measured and modeled response. This inverse

method has been introduced and used previously by others [53], [54]. The complete set of parameters used in the JCA models for conventional foams are listed in Table 3.2, where the values for tortuosity, viscous characteristic length, and thermal characteristic length result directly from the optimization.

Table 3.2: Summary of JCA model parameters used for conventional foam samples

Foam (conventional)	ϕ	α_∞	σ (N s/m^4)	Λ (mm)	Λ' (mm)
5 PPI	.901	1.00	50	1.06	1.90
20 PPI	.881	1.00	350	.931	1.49
40 PPI	.922	1.00	520	.639	1.21

The results in Table 3.2 show trends of decreasing characteristic lengths as pore size decreases (PPI increases), as well as constant tortuosity near unity. The tortuosity result is not surprising since all foams have a similar microstructure and furthermore it is close to a reported result in the literature [1] for a 40 PPI foam ($\alpha_\infty = 1.07$).

Compressed Samples

In this section, a method for predicting the acoustic absorption of the compressed samples is described and implemented. The method involves prediction of the change in the foams' microstructure parameters assuming known compression ratio and intial microstructure parameters. Some predictions have been formulated analytically for the case of compression of a fibrous material. For 1D compression, assuming a small fiber radius [55],

$$\phi^{(n)} = 1 - n(1 - \phi^{(0)}),\ \alpha_\infty^{(n)} = 1 - n(1 - \alpha_\infty^{(0)}),\ \sigma^{(n)} = n\sigma^{(0)} \tag{3.7}$$

$$\Lambda^{(n)} = \frac{\Lambda^{(0)}}{\sqrt{n}},\ \Lambda'^{(n)} = \frac{\Lambda'^{(0)}}{\sqrt{n}} \tag{3.8}$$

where $^{(0)}$ refers to the parameter of the conventional material and $^{(n)}$ the compressed material after undergoing compression of one side $n = \frac{L^{(0)}}{L^{(n)}}$. For 2D, n in the expressions above is replaced with n^2 [56]. Extrapolating to 3D, utilizing the relationship for volumetric compression ratio $\upsilon = n^3$, and rewriting in dimensionless form, the expressions become

$$\phi^{(\upsilon)} = 1 - \upsilon(1 - \phi^{(0)}),\ \alpha_\infty^{(\upsilon)} = 1 - \upsilon(1 - \alpha_\infty^{(0)}),\ \frac{\sigma^{(\upsilon)}}{\sigma^{(0)}} = \upsilon \tag{3.9}$$

$$\frac{\Lambda^{(\upsilon)}}{\Lambda^{(0)}} = \frac{1}{\sqrt{\upsilon}},\ \frac{\Lambda'^{(\upsilon)}}{\Lambda'^{(0)}} = \frac{1}{\sqrt{\upsilon}} \tag{3.10}$$

To examine validity of the extrapolations, finite element models were constructed of a 3D unit pore based on the Gibson model [5] which considers beam bending as the main deformation mechanism. Two stages of finite element analysis were done sequentially. First, an elasto-plastic deformation was performed to simulate crushing of the pore. One eighth of the model was meshed and symmetry boundary conditions were applied to three perpendicular faces. A displacement boundary condition was prescribed on faces of strut segments to induce uniform, triaxial compression. Nonlinear geometry and nonlinear material properties were used; plasticity data for aluminum was taken from measurement on individual aluminum foam ligaments [57]. Results from this simulation is shown in Figure 3·6.

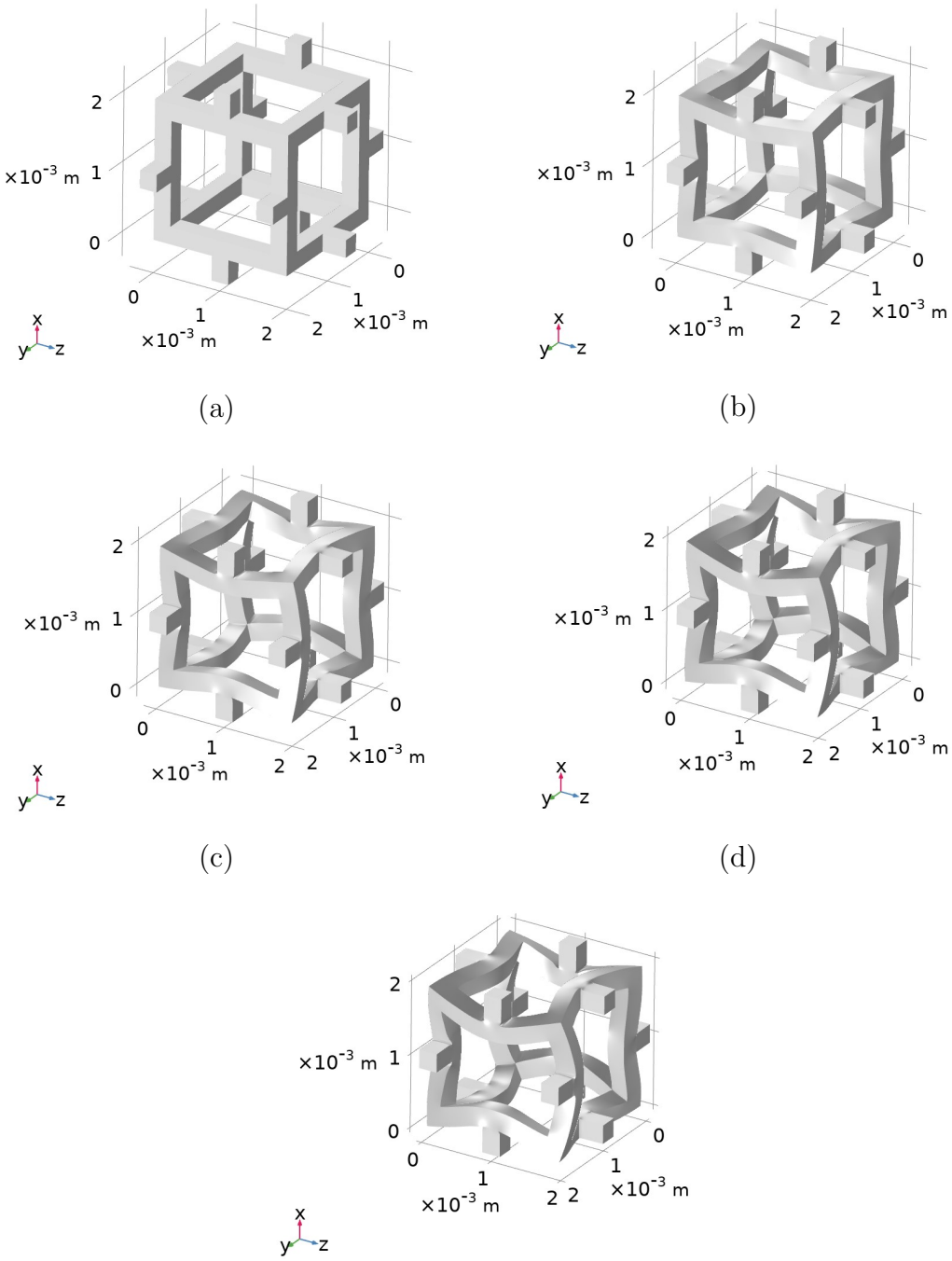

Figure 3·6: Elasto-plastic compression models of representative unit pores for varying volumetric compression ratios of approximately (a) 1.00, (b) 1.25, (c) 1.50, (d) 1.75, and (e) 2.00.

Second, a pair of simulations was done to estimate the five microstructure parameters from the unit pores. For these simulations, the geometry of the air surrounding the foam is created by subtracting deformed foam geometry from the bounding box volume of the cell. The simulations are 1) a steady state Stokes flow and 2) an electric conduction problem. These simulations represent opposite ends of the frequency spectrum: low frequency where viscous effects dominate and high frequency where bulk viscous effects become negligible. This method of estimating the foam microstructure parameters from electric and flow simluations has been well established in the literature [1], [2]. Results from the flow and electric simulations are shown in Figure 3·7.

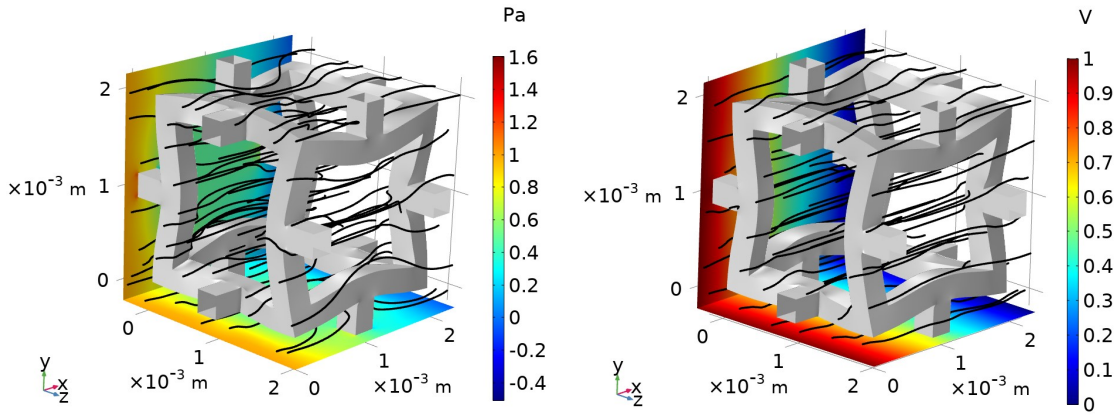

(a) (b)

Figure 3·7: Unit pore simulations showing (a) pressure difference contour across a pore and resulting velocity streamlines and (b) electric potential difference contour across a pore and resulting electric field streamlines.

The porosity and thermal characteristic length are purely geometrical properties that can be computed from the mesh by using:

$$\phi = \frac{V_{air}}{V_{bulk}}, \ \Lambda' = \frac{2V_{air}}{SA} \tag{3.11}$$

where V represents volume and SA represents the wetted surface area.

From the flow simulation, a pressure gradient is imposed on the pore, no-slip boundary conditions at the foam interface, and periodicity at lateral faces. The airflow resistivity can be computed by Darcy's law

$$\sigma = \frac{A\Delta p}{QL} \tag{3.12}$$

where A is the outlet cross sectional area, Δp is the prescribed pressure difference, Q is the outlet volumetric flow rate, and L is the thickness.

From the electric simulation a potential difference is imposed on the pore, insulating boundary conditions at the foam interface, and symmetry at the lateral faces. The viscous characteristic length and tortuosity can be computed from

$$\Lambda = 2\frac{\int_V \mathbf{E}^2 dV}{\int_{SA} \mathbf{E}^2 dSA}, \ \alpha_\infty = \frac{\langle \mathbf{E}^2 \rangle}{\langle \mathbf{E} \rangle^2} \tag{3.13}$$

where $\mathbf{E}$ is the electric field and $\langle\ \rangle$ indicates a fluid-average quantity.

For the conventional pore and four compressed pores, both of the described simulations are done to compute the change in foam microstructure parameters versus volumetric compression ratio. The results are plotted in Figure 3·8 in dimensionless form alongside the expressions in Equations (3.9) – (3.10).

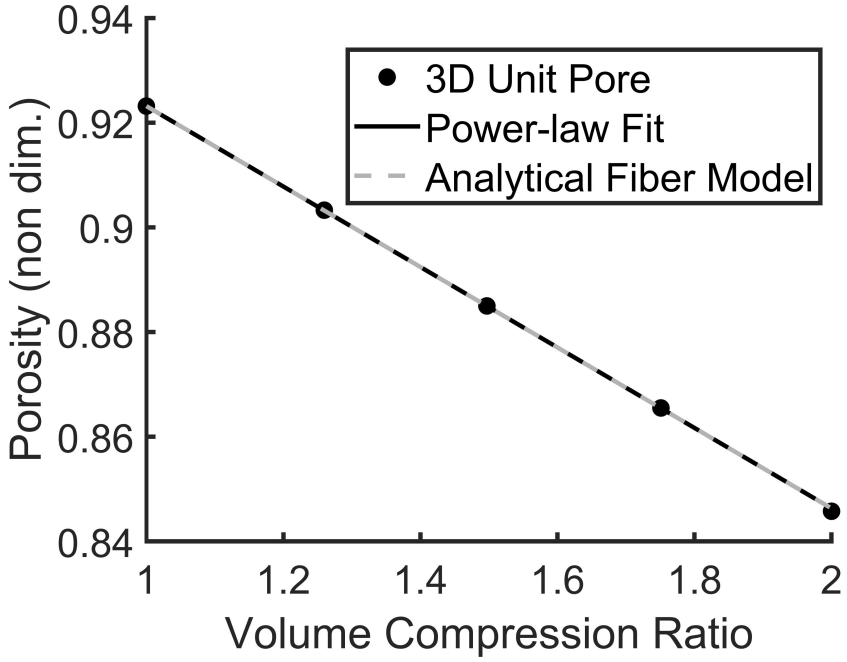
0.94
0.92
0.9
0.88
0.86
0.84
Porosity (non dim.)
1
1.2
1.4
1.6
1.8
2
Volume Compression Ratio
3D Unit Pore
Power-law Fit
Analytical Fiber Model

(a)

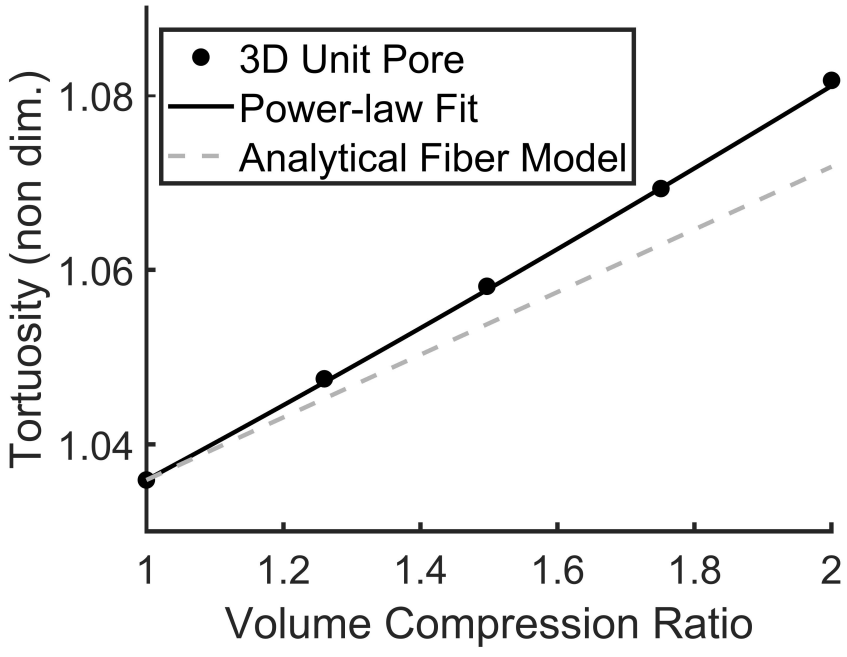
1.08
1.06
1.04
Tortuosity (non dim.)
1
1.2
1.4
1.6
1.8
2
Volume Compression Ratio
3D Unit Pore
Power-law Fit
Analytical Fiber Model

(b)

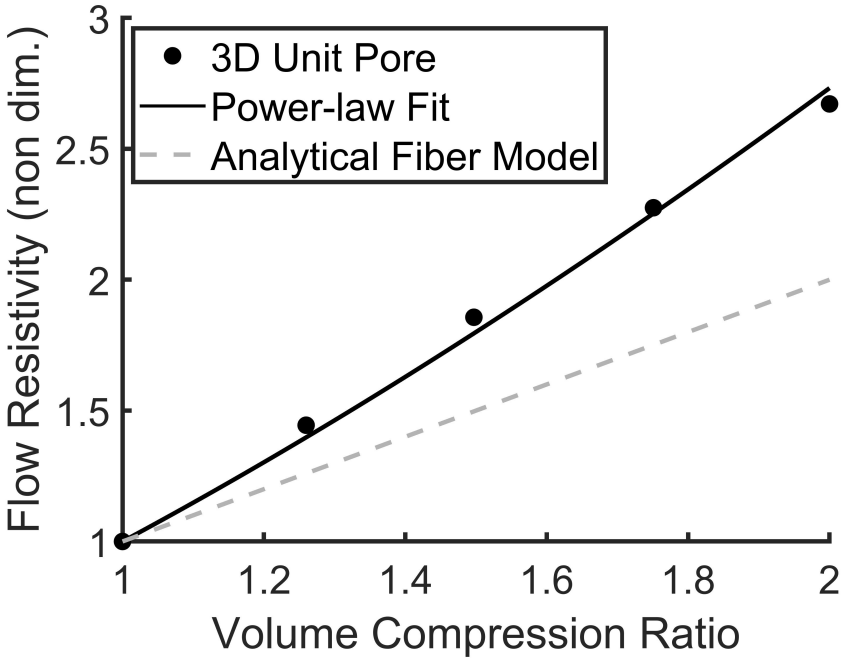
3D Unit Pore
Power-law Fit
Analytical Fiber Model
Flow Resistivity (non dim.)
Volume Compression Ratio
1
1.5
2
2.5
3
1
1.2
1.4
1.6
1.8
2

(c)

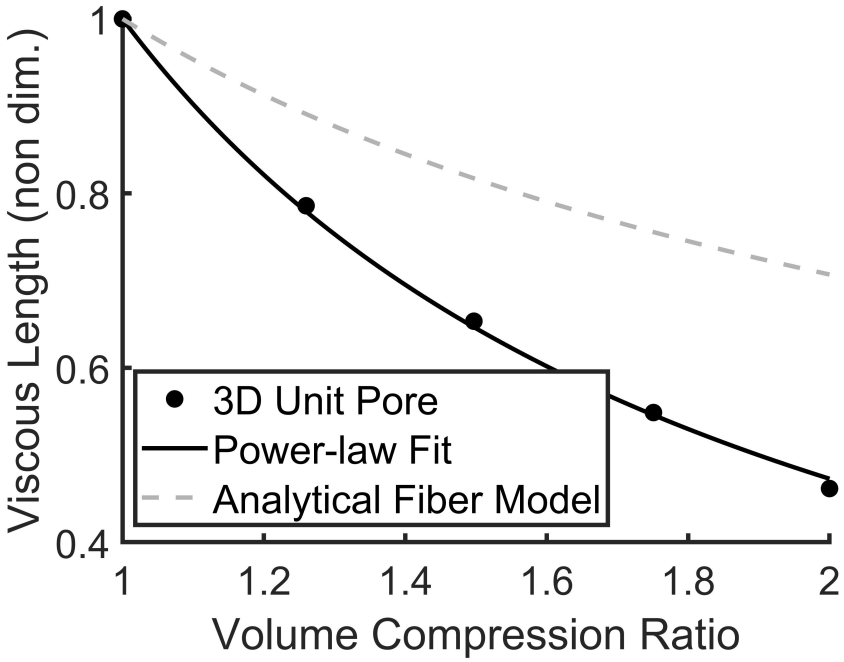
3D Unit Pore
Power-law Fit
Analytical Fiber Model
Viscous Length (non dim.)
Volume Compression Ratio
0.4
0.6
0.8
1
1
1.2
1.4
1.6
1.8
2

(d)

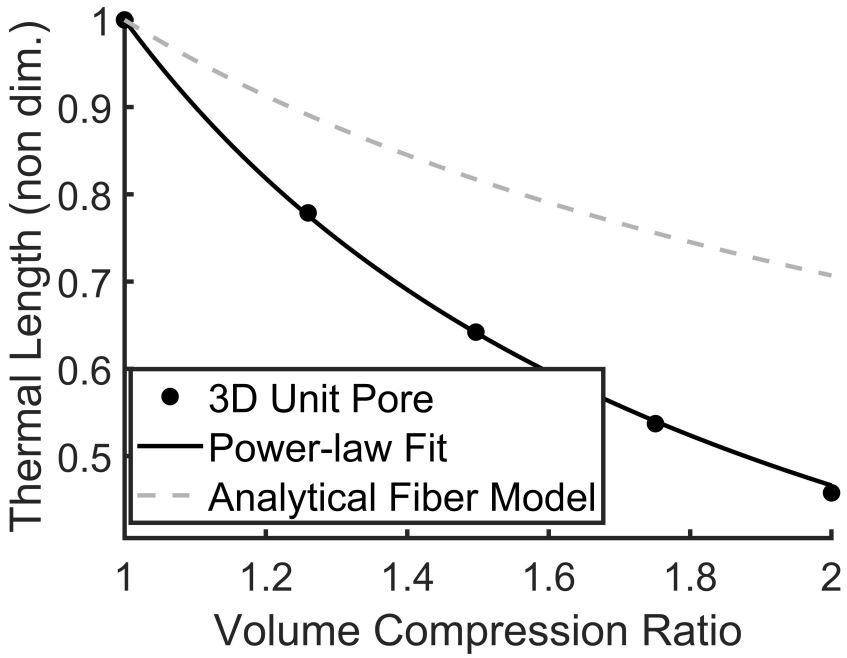

(e)

Figure 3·8: Variation of foam microstructure properties versus compression ratio resulting from finite element predictions of a 3D unit pore.

It can be seen that the porosity predicted by the analytical expression is in close agreement with that predicted by the 3D unit pore. This is essentially an expression of mass conservation during volumetric compression. The remaining parameters show substantial deviation from predictions based on the fibrous model, which can be attributed to differences in the structure of an array of parallel fibers versus a foam.

Based on the results of the 3D unit pore, a power scaling law was fitted for each parameter based on the same form as the analytical expressions. The power scaling laws are:

$$\phi^{(\upsilon)} = 1 - \upsilon(1 - \phi^{(0)}),\ \alpha_\infty^{(\upsilon)} = 1 - \upsilon^{1.175}(1 - \alpha_\infty^{(0)}),\ \frac{\sigma^{(\upsilon)}}{\sigma^{(0)}} = \upsilon^{1.45} \tag{3.14}$$

$$\frac{\Lambda^{(\upsilon)}}{\Lambda^{(0)}} = \frac{1}{\upsilon^{1.08}}, \ \frac{\Lambda'^{(\upsilon)}}{\Lambda'^{(0)}} = \frac{1}{\upsilon^{1.1}} \tag{3.15}$$

These expressions are useful for predicting changes in a foam's microstructure parameters as a function of compression ratio, thereby enabling the acoustic absorption of compressed foams to be predicted. In the next section, the results from the models are presented and discussed.

3.1.4 Results and Discussion

Using the conventional foam properties in Table 3.2, Equations (3.14)-(3.15), and measured compression ratios in Table 3.1, the acoustic absorption of compressed samples can be predicted with the JCA model as described in section 3.1.3. The modeling results are plotted over measurements in Figure 3·9. As mentioned in section 3.1.2, uncertainty of measurement in volumetric compression ratio from the samples' bulk dimensions will lead to a range in predicted microstructure parameters and absorption. This is represented by error bars in the plot.

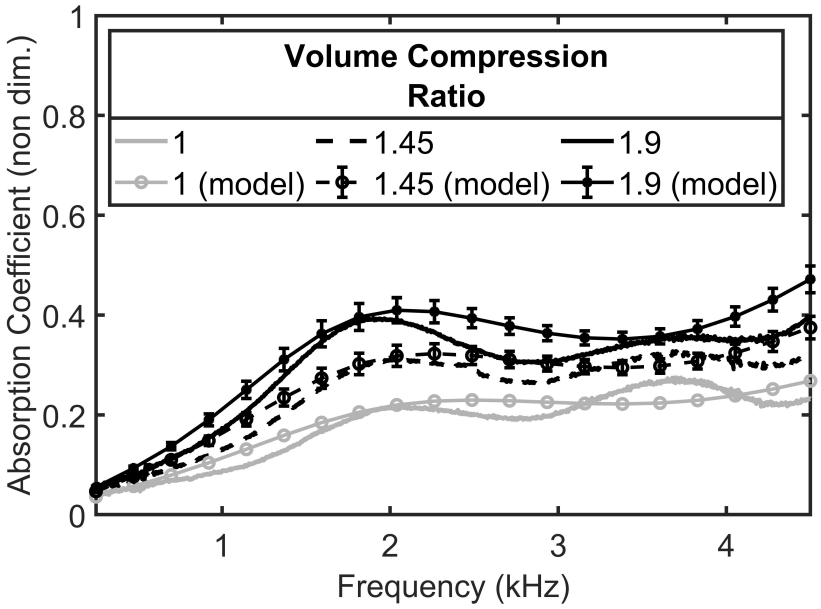
Volume Compression Ratio
1
1.45
1.9
1 (model)
1.45 (model)
1.9 (model)
Absorption Coefficient (non dim.)
Frequency (kHz)
0
0.2
0.4
0.6
0.8
1
2
3
4

(a)

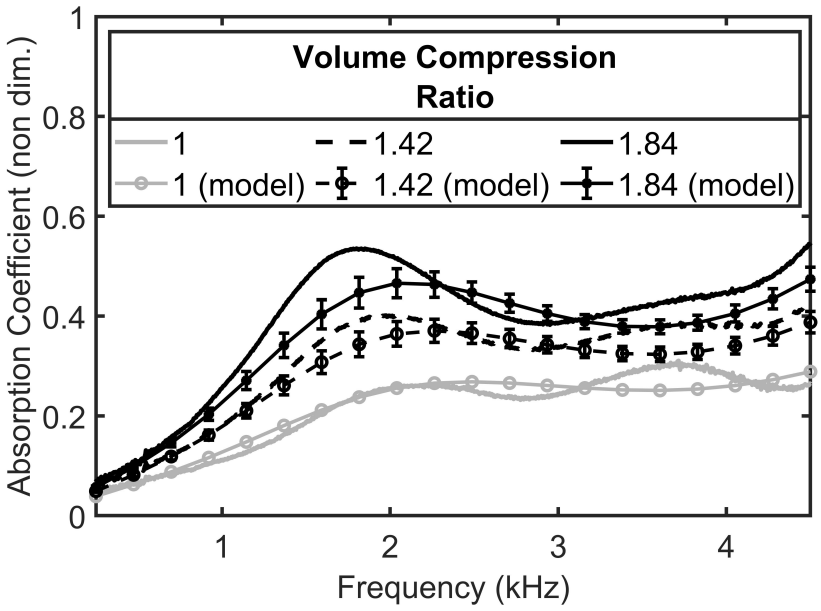
Volume Compression Ratio
1
1.42
1.84
1 (model)
1.42 (model)
1.84 (model)
Absorption Coefficient (non dim.)
Frequency (kHz)
0
0.2
0.4
0.6
0.8
1
2
3
4

(b)

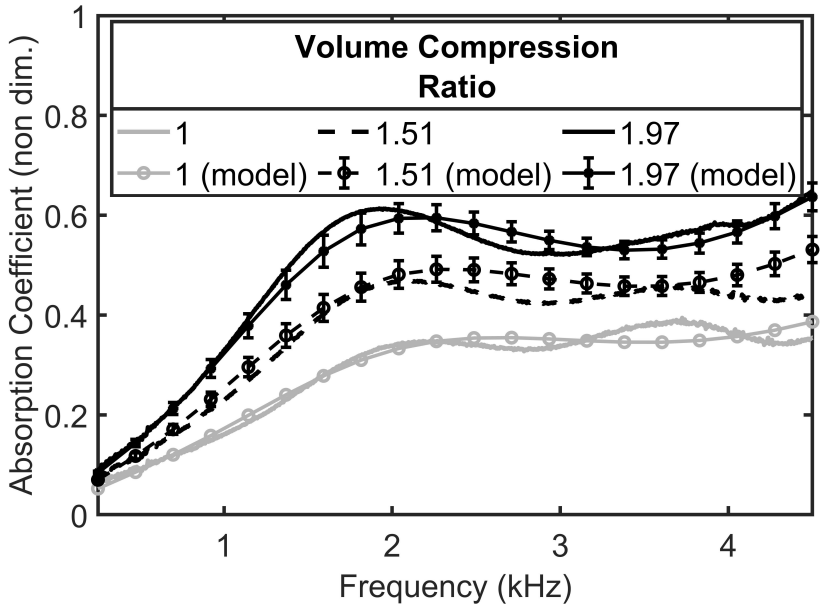

(c)

Figure 3·9: Normal incidence sound absorption coefficient measurements and modeling results for metallic foam samples (a) 5 PPI, (b) 20 PPI, and (c) 40 PPI. All samples approximately 45 mm thick.

The global trend of increasing absorption with increasing volumetric compression ratio is predicted correctly by the model, with the best agreement for the 40 PPI foams. There are, however, some underlying assumptions in the experiment and limitations of the model could be sources of error.

For the hydrostatic experiment, it is assumed that there is ideal, uniform compression across the entire sample. This could lead to uncertainty in measuring the compression ratio if certain regions of the foam compressed further than other regions. The model makes use of the Gibson unit cell, which is isotropic. It is known that some metallic foams are not isotropic due to effects of gravity on the manufacturing process. In addition, although the Gibson unit cell has been widely used in the literature for prediction of bulk properties for many types of open-cell foams, it does not, strictly speaking, represent the exact microstructure of foams produced by the

manufacturer.

The foam microstructure parameters in Equations (3.14)-(3.15) were predicted based on compression ratios up to 2. For greater than 2, it is not guaranteed that the trends will continue scaling in the same manner, since the deformation mechanisms change once self contact is initiated between foam ligaments, when stiffness of the foams begins to dramatically increase. Lastly, the model has assumed the rigid-framed acoustic absorption mechanism is maintained. Foams whose frame is not rigid (can be excited acoustically in air) or are closed cell have different absorption mechanisms and would require a modified analysis.

3.1.5 Conclusion

A method for triaxial deformation of metallic foam was presented which included preparation and sealing of the sample and hydrostatic pressure loading. For the application of sound absorption, compressed samples had higher measured sound absorption broadband than conventional samples. The best sound absorber was a 40 PPI foam compressed with a volumetric compression ratio of 2. The Johnson-Champoux-Allard model was used to model acoustic absorption trends. Five microstructure parameters of the foam used in the model were shown to change with volumetric compression ratio and were able to be predicted based on finite element simulations of a 3D unit pore.

3.2 Bulk Mechanical Loading of Metallic Foam after Triaxial Hydrostatic Compression

As seen in the previous section, the microstructure of open cell metallic foams can be transformed through plastic deformation which can significantly change acoustic properties. Additionally, this preferential buckling of the foam struts can lead to dramatically different ranges of structural properties such as elastic modulus and

Poisson ratio. In this section, foams that were hydrostatically deformed were tested using a load cell and digital image correlation. Details of the experiments and the resulting structural properties are reported in the remainder of this chapter.

3.2.1 Introduction

In this section, the bulk mechanical properties of conventional and compressed foams are compared by subjecting the materials to quasi-static loading. The compressed foams were created in the same way as described in section 3.1.2. The foams that were tested are shown in Figure 3·10. Due to the destructive nature of the testing, the samples used in this section were not the exact same samples as described previously for acoustic testing but were the same brand of aluminum foams.

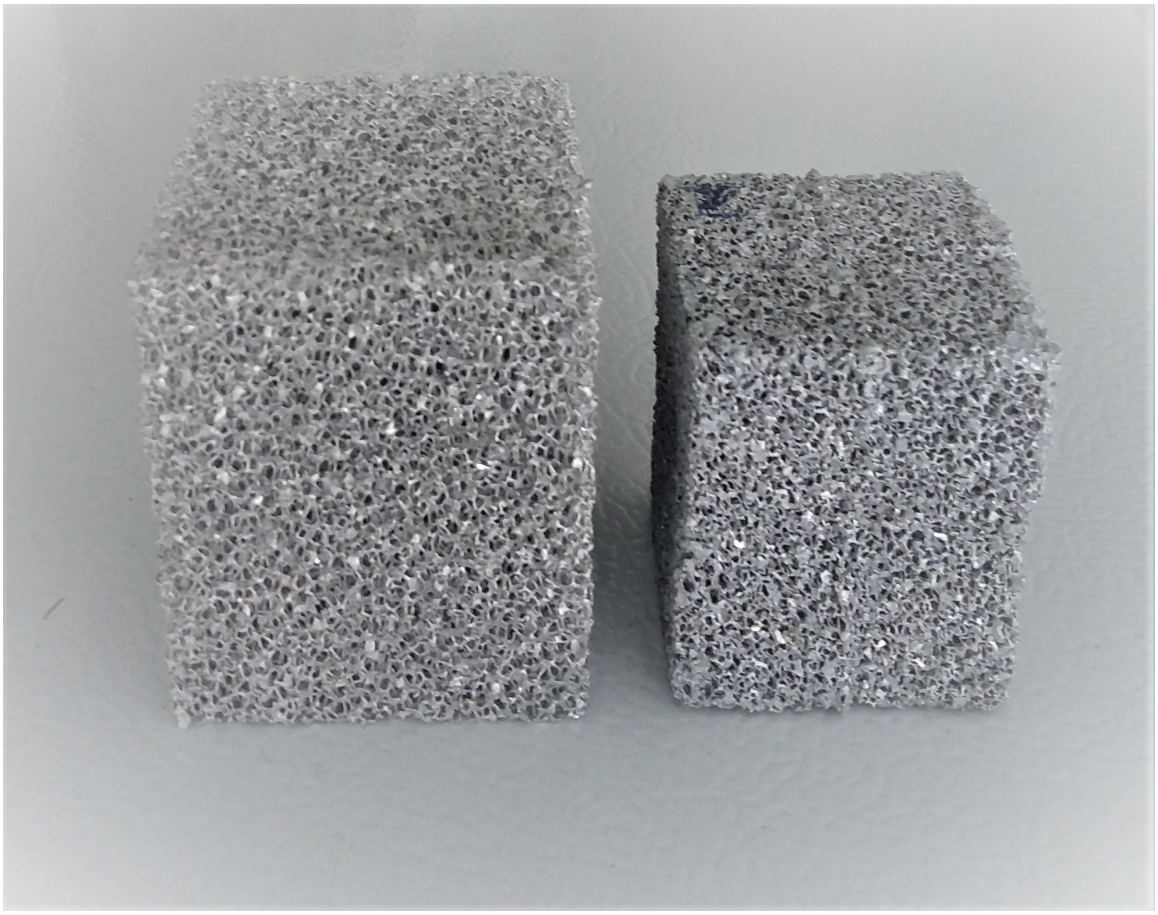

Figure 3·10: 40 PPI, 10% nominal relative density Duocel aluminum foam. Sample to the right is compressed with a volumetric compression ratio of approximately 1.96 using 10.3 MPa of hydrostatic pressure.

3.2.2 Experimental Setup

Compressive tests were performed using an 300 kN Instron load cell, similar to tests described in [58]. Samples were compressed along the height, and the corresponding faces in contact with the platens were sanded to be flush. The platens were lubricated with a think layer of molybdenum grease. Load cell displacement rates of 2×10^{-4} to 3×10^{-4} inches/second were used. Additionally, the displacement of the samples was measured using digital image correlation (DIC) with Instron's AVE2 camera in "speckle only" mode. This measurement technique allows for full field (in plane)

displacement and strain measurements. To prepare the samples for DIC, first the front surface of the specimen was filled with a thin (less than 3 mm) layer of flexible caulk. Since the foam is porous, the leading surface is difficult to detect with the camera thus the effect of the caulk is to create a flat leading surface that can be more easily detectable. The caulk was assumed to be soft enough to not effect the global displacement of the foam. After filling with caulk, a speckle pattern was spray painted on the sample with a base color in black and white speckles on top. The speckles were sized to have approximately 5-10 pixels across the diameter with approximately 50% black and 50% white. Samples were loaded to about 0.6 engineering strain. Force was measured by the load cell and displacements were measured both by the cross-head and using Instron DIC Replay software.

3.2.3 Results

DIC results for the conventional foam are shown in Figure 3·11. In the image, the foam is being compressed from the top down. Both profiles are typical of a material with a positive Poisson ratio that experiences axial contraction with transverse expansion.

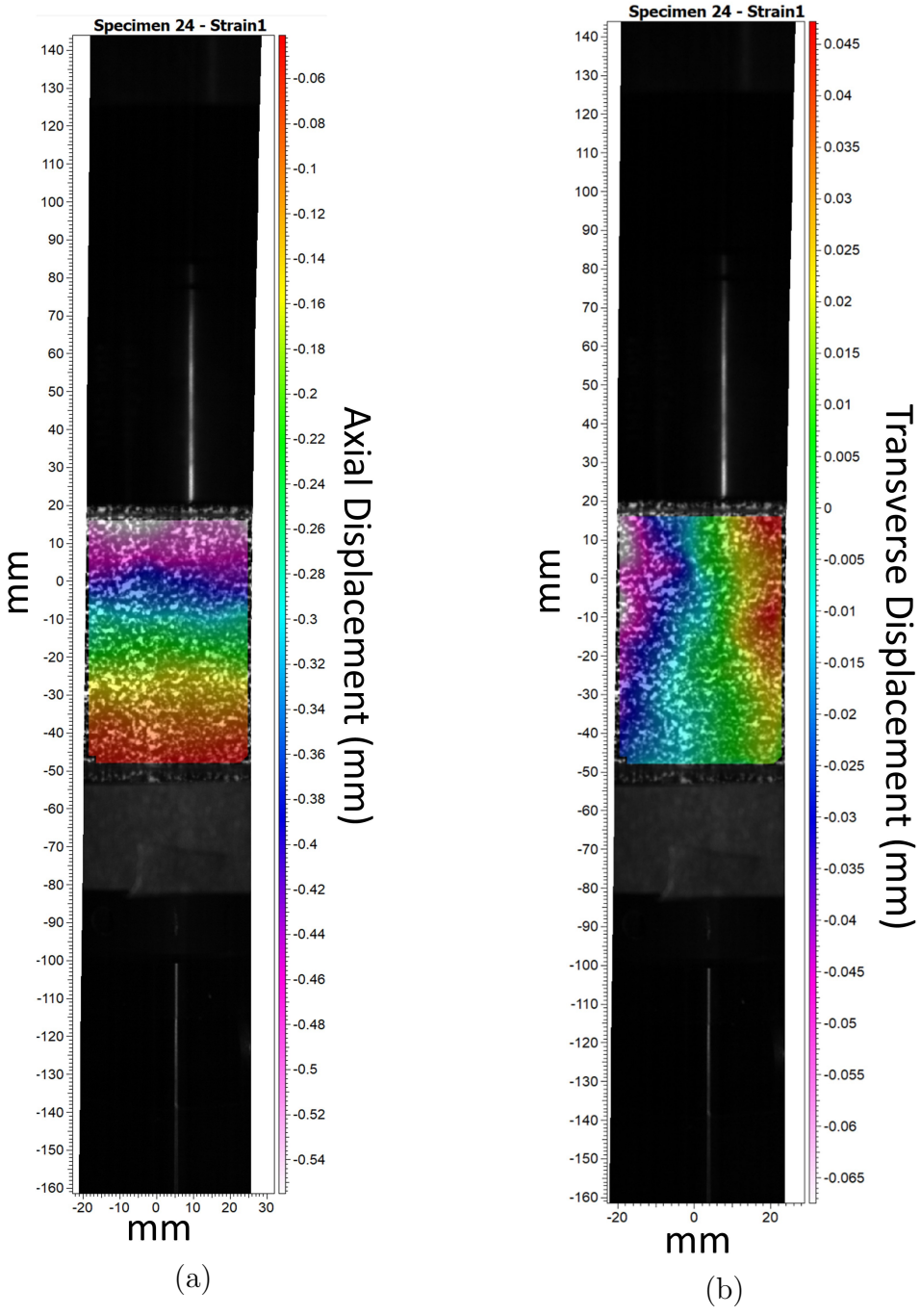

Figure 3·11: (a) Axial displacement (mm) and (b) transverse displacement (mm) for the conventional 40 PPI, 10% relative density aluminum foam at strain of 0.01.

Results for the compressed sample are shown in Figure 3·12. The axial displace-

ment appears uniform, however the transverse displacement does not. The top and bottom of the sample appear to be bulging outward while the middle is moving inward, almost forming an hour glass shape. This behavior is expected for a negative Poisson ratio material. In the next subsection, numerical results for each material will be discussed and compared.

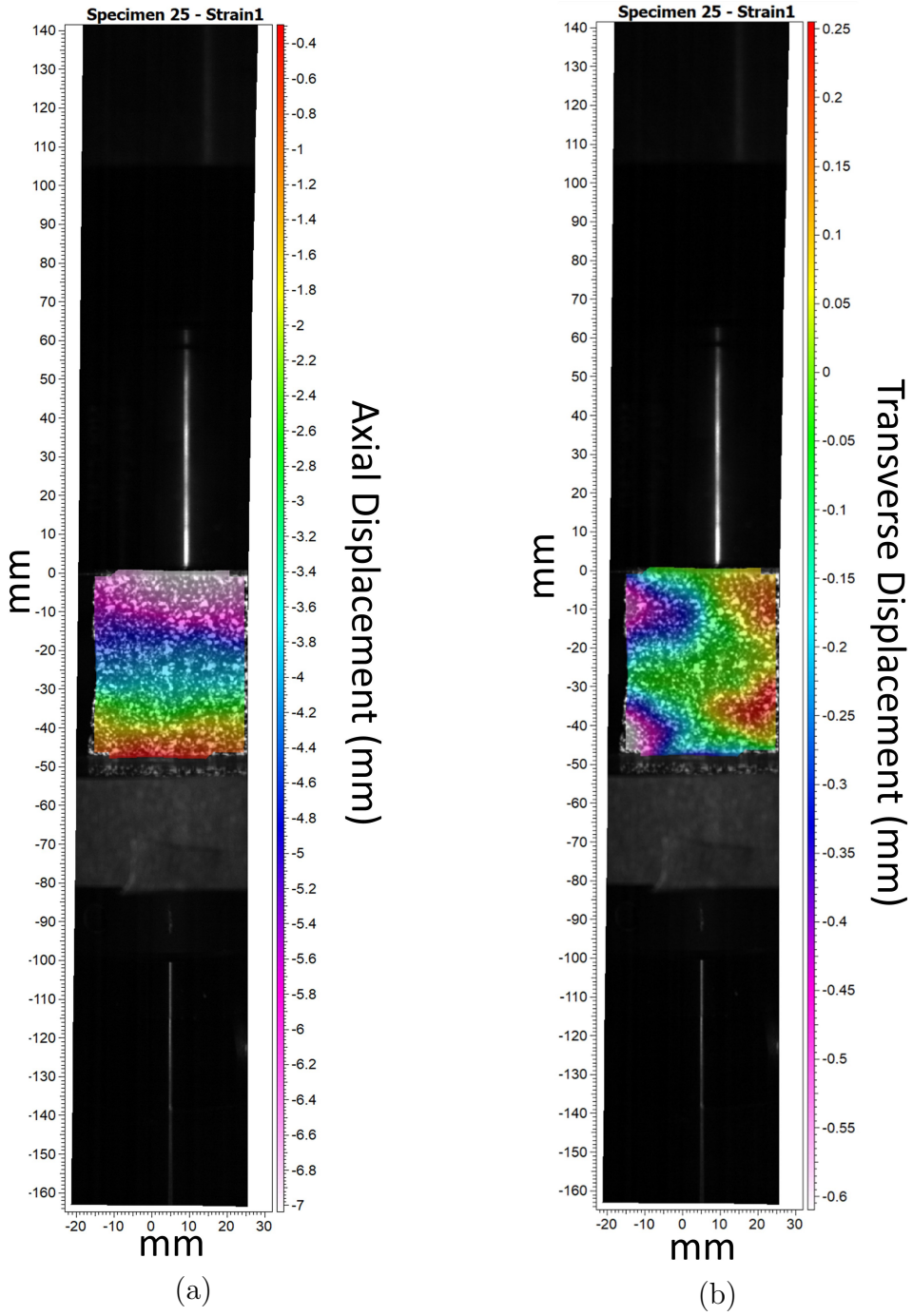

Figure 3·12: (a) Axial displacement (mm) and (b) transverse displacement (mm) for the compressed (volumetric compression ratio of 1.96) aluminum foam at strain of 0.13.

3.2.4 Discussion

The stress-strain curves as well as data for the Poisson effect are shown in Figure 3·13. In Figure 3·13 (a), 3 deformation regimes can be seen that are characteristic of cellular solids. For small strain, both foams have a linear elastic regime. This is followed by yielding and a flat plateau regime. The last regime, densification, is seen to start around strain of 0.6. This regime is characterized by a sharp increase in modulus where self contact between struts has initiated. The Poisson effect was measured using virtual gauges that were placed along the center lines, vertically and horizontally as shown in Figure 3·14. It is seen that the Poisson effect is strain dependent, and is near zero for the compressed sample and between 0.2 – 0.4 for the conventional sample. These results are consistent for what has been observed for copper foams [9]. The mechanical toughness or energy absorption capability per unit volume is computed by integrating the stress strain curve.

$$T = \int_0^{\epsilon_f} \sigma d\epsilon \tag{3.16}$$

The upper limit of integration is denoted by ϵ_f. For a material undergoing tension, this is usually taken as a fracture point. For many applications such as automotive bumpers, compressive strain greater than or equal to 0.5 can be achieved and that entire range of deformation is useful in terms or energy absorption. Therefore the mechanical toughness relative to $\epsilon_f = 0.5$ has been computed.

Results from Table 3.3 indicate that the compressed sample was approximately half as stiff as the conventional sample. Furthermore, the compressed sample had a higher yield stress (and strain). From Figure 3·13 (a), there is also a much larger area under the stress-strain curve for the compressed sample and a higher computed toughness.

Table 3.3: Quantitative results from compression experiments

	conventional	compressed
elastic modulus (MPa)	475	249
yield stress (MPa)	2.23	5.289
strain at yield	.005	.023
toughness (MJ/m^3)	1.51	5.51

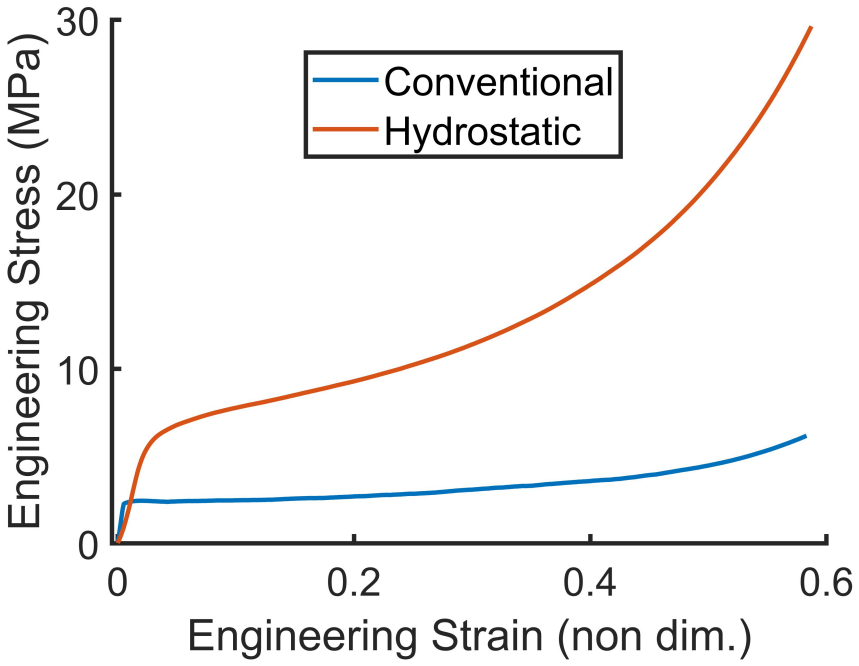
Engineering Stress (MPa)
30
20
10
0
0
0.2
0.4
0.6
Engineering Strain (non dim.)
Conventional
Hydrostatic

(a)

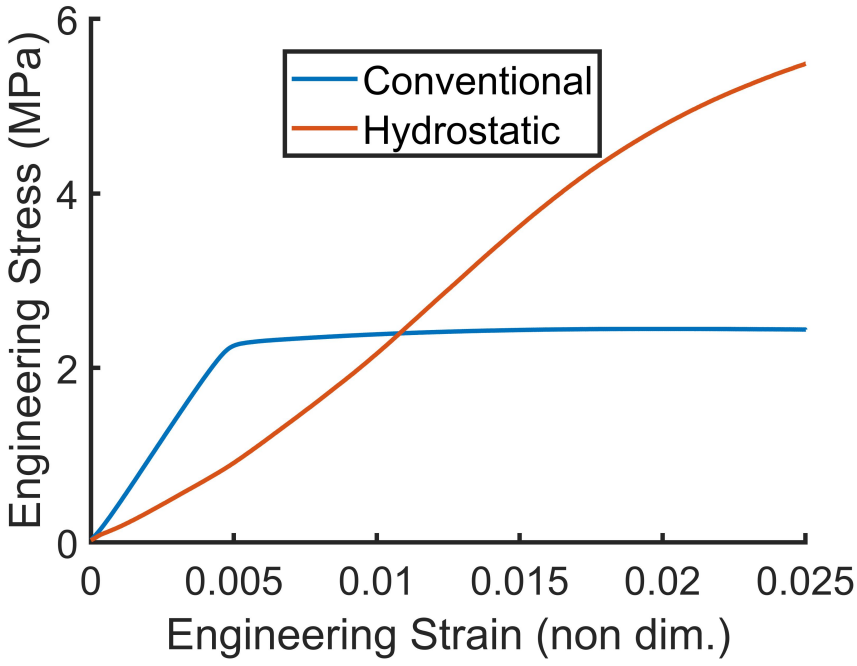
Engineering Stress (MPa)
6
4
2
0
0
0.005
0.01
0.015
0.02
0.025
Engineering Strain (non dim.)
Conventional
Hydrostatic

(b)

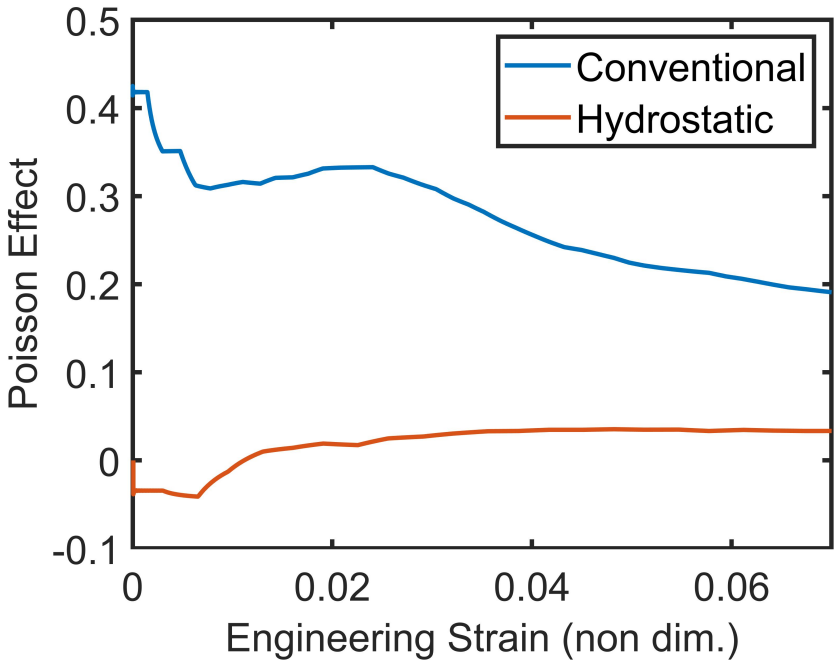

(c)

Figure 3·13: Comparison between the conventional and compressed sample for (a) stress-strain, (b) stress-strain linear elastic regime, and (c) Poisson effect

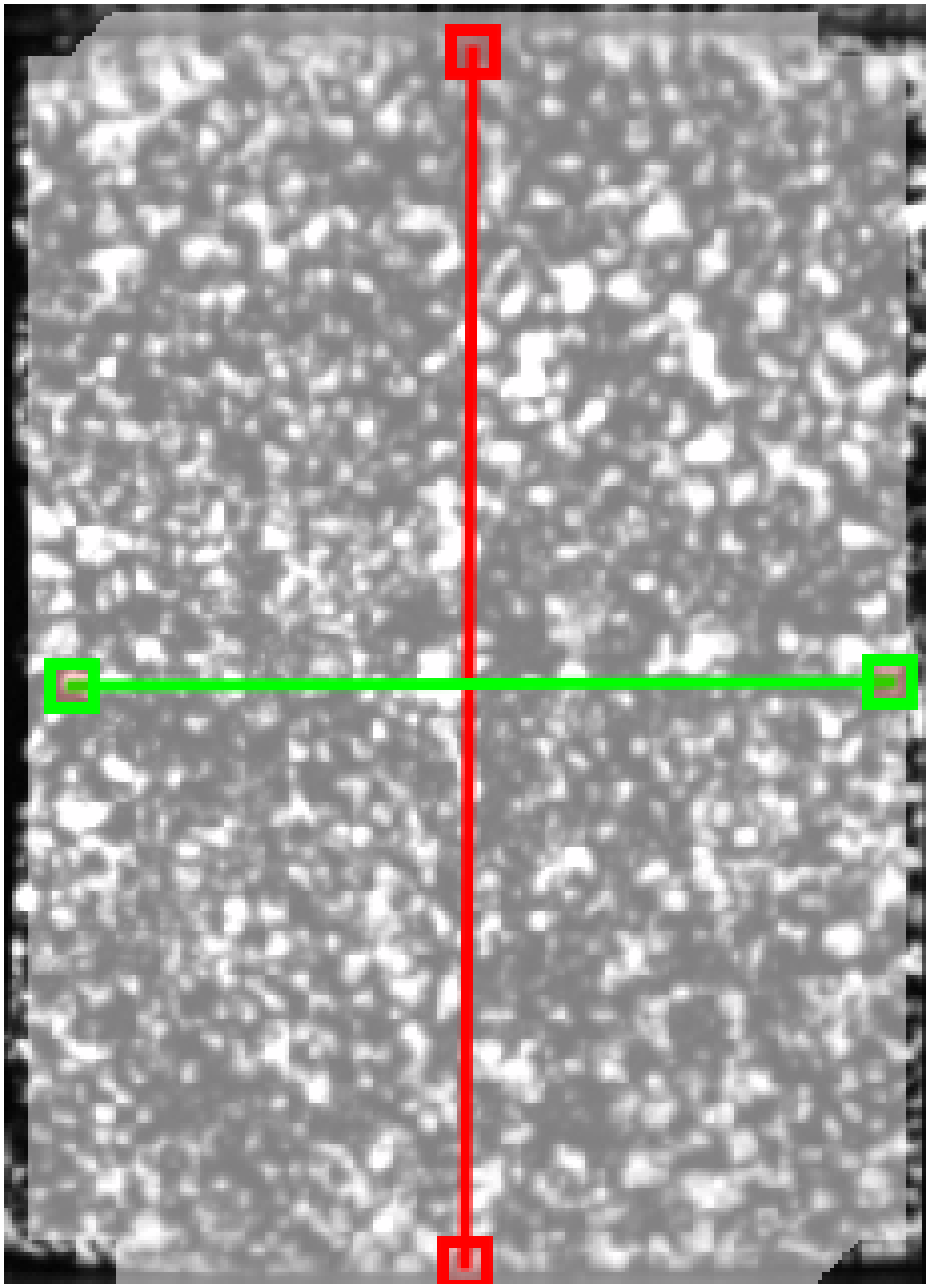

Figure 3·14: Location of virtual strain gauges which measure transverse and axial strains.

Similar results have been reported for copper foams; the mechanism has been explained by the formation of local plastic hinges in the foam [9]. Plastic hinges are regions of significant plastic deformation that result in decreased stiffness. To confirm

this hypothesis for aluminum foams, a numerical simulation was setup on a pore of aluminum foam constructed from micro-CT scans. The model simulated plastic crushing of the pore, using non-linear geometry and non-linear (plastic) material properties of aluminum taken from [57]. In the simulation, three sides of the pore were fixed and the remaining three sides were given a prescribed displacement. The plastic strain is shown in Figure 3·15 for a volumetric compression ratio near 1.5. This result confirms the formation of local plastic hinges (red spots in Figure 3·15) and furthermore it can seen seen that the hinges form near midpoints of the struts.

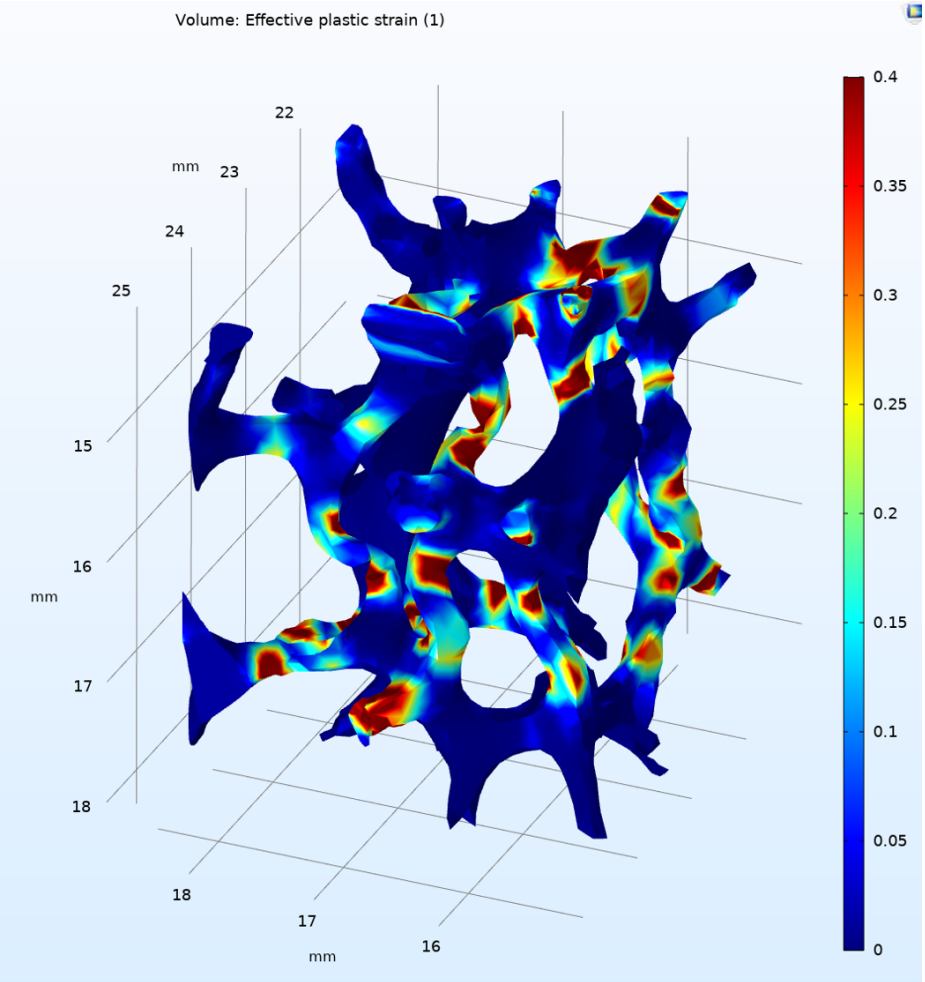

Figure 3·15: Effective plastic strain on an aluminum foam pore after volumetric compression.

3.2.5 Conclusion

Compression experiments were performed on a conventional aluminum foam and a foam that was crushed to half the bulk volume using hydrostatic pressure. The results indicate that hydrostatically compressed foams are less stiff, however they also have the potential to absorb more energy as seen by a sufficiently larger area underneath the stress-strain curve. The formation of local plastic hinges, which has been previously hypothesized in the literature, has been confirmed through numerical simulations.

Chapter 4

Acoustic Absorption and Vibration Damping by Saturated Metallic Foam

4.1 Acoustic Absorption of Metallic Foam Saturated by Polyurethane Foam

In this section, a composite foam consisting of open-cell metallic foam embedded with polyurethane foam is fabricated and evaluated for sound absorbing properties. The best performing composite foam increased the sound absorption by a factor of 6 (from 0.1 – 0.6) in the low frequency test range and by a factor of 2 (from 0.2 – 0.4) up to 4.50 kHz, compared to the original metallic foam. A lumped element model is used to predict and elucidate the absorption mechanisms for the composite, as well as for pure metallic foam and pure polyurethane foam. The model gives insight into the physical mechanisms that control acoustic absorption, including thermo-viscous effects at pore interfaces, structural damping effects due to foam elasticity, and coupling effects due to the interaction of air, metal, and polyurethane in the composite. Additionally, a simplified two parameter model was used to elucidate acoustic absorption trends for composite foams. The developed composite foams are advantageous for engineering and architectural applications where combined high stiffness and sound absorption are required.

4.1.1 Introduction

Foamed materials, such as those made from polymers, metals, ceramics, and fibers, find widespread use in many engineering applications requiring high energy absorption, strength, stiffness, thermal conductivity, or padding. This work investigates the use of metallic and polyurethane (PU) foams for structural acoustic applications, where it is desired to have multifunctional characteristics; i.e., be sufficiently stiff to support static load while also having high sound absorption to reduce noise. Metallic foams tend to excel in the former whereas PU foams the latter.

In this chapter, a composite foam consisting of metallic foam filled with a polyurethane foam is proposed and fabricated. The composites retain the high stiffness of the metal foam while improving the sound absorption, compared to the original metallic foam sample. The highest performing composite foam improved the sound absorption of metallic foam by a factor of 6 (from 0.1 – 0.6) in the low frequency range (near 600 Hz), and a factor of 2 (from 0.2 – 0.4) broadband. The polyurethane foam used in this study is shown experimentally to have a low frequency quarter wavelength resonance (characteristic of an elastic frame), whereas the metal foam does not (characteristic of a rigid frame). The composite material is shown experimentally to retain the low frequency resonance. This is evidence of the composite being acoustically compliant while maintaining exceptionally high static stiffness, a characteristic that could be leveraged for absorbing layers or walls under high static loading.

Furthermore in this chapter, a lumped element model is developed and utilized to accurately estimate acoustic impedance and absorption for 3 different types of foams: rigid frame, elastic frame, and the composite. The lumped element model used in this chapter is chosen because the fabricated composite foam is different from traditional foams. It consists of 2 different materials with 2 distinct porosities and 2 characteristic

pore sizes. Furthermore there is a mechanical bond that joins the PU to the metal in the foam, and this effect can be important to consider. The use of the lumped element model allows one to use properties of each constituent material independently, and is therefore advantageous for the fabricated foam-in-foam composite.The model is benchmarked to experimental measurements, and gives insight into the physical mechanisms that control acoustic absorption by treating segments of the foam as discrete masses, springs, and dashpots. The model also provides design insights.

An excellent review of sound absorbing foams is given by Arenas [59]. There are two dominant absorption mechanisms in the long wavelength, linear acoustic regime: viscous and thermal losses that occur at the porous frame and fluid interface and structural damping losses that occur due to motion of the frame. The type of foam, host material, and geometry all impact the effective contribution of each mechanism.

Metallic foams are porous metals that can be fabricated in both open and closed-cell configurations. Their high stiffness to weight ratio is derived from an interconnected metal framework surrounded by large volume fractions of air. The stiffness of metallic foams has been extensively studied in terms of mass and geometry scaling laws [5]. Acoustically, metallic foams (especially closed-cell) tend to have poor to fair sound absorption [1]. One reason for this is that the metal frame is much stiffer than the surrounding air, therefore when considering acoustic wave propagation essentially only one wave propagates through the fluid. The acoustic losses come from viscous and thermal effects that occur at the metal-air interface which depend on the foam pore shape and structure. Some metallic foam manufacturing processes are limited in producing foams with certain pore sizes and porosities, thereby limiting absorbing capabilities.

PU foams having fully and partially reticulated cells [60, 61] as well as completely closed-cells, [62] have been studied extensively for acoustic properties. A large range

of acoustic properties arise from these foams, depending on stiffness, pore size, and reticulation rate. For example, some open-cell PU foams have rigid frames, such that the acoustic loss mechanism is similar to that of metallic foams [63]. For closed-cell PU foams, elasticity of the foam and structural damping dominate, and the foam can be treated as an effective elastic material [62]. Many closed-cell foams, however, contain partially open cells at outer faces of the material due to the manufacturing process or sample preparation (cutting). This feature has been shown to significantly increase acoustic losses [64] because these cells have additional thermal and viscous effects. Partially reticulated PU foams with a flexible frame exhibit losses due to both structural and thermo-viscous effects.

Regarding structural losses, the vibration of the frame is often not appreciable when excited acoustically in air except for resonant conditions. When the frame resonates, it can have significant influence on the surface impedance and absorption capabilities. The effect of frame resonance depends on the microstructure, material composition, and overall thickness of the sample. For example as described in [65], a glass wool material much denser and stiffer than air exhibited a resonance in surface impedance around 850 Hz for a 54 mm thick sample (see their Figure 2). A resonant peak was also present in the absorption coefficient around this frequency, in which the absorption was 14% higher than predicted by a rigid-frame model. As studied in [66], the frame resonance can also be impacted by mounting conditions in the impedance tube. Vigran *et al.* [67] also studied this effect using a finite element model. For a polyurethane foam sample, a large peak in absorption coefficient was experimentally measured at low frequency (800 Hz) and identified as a frame resonance due to amplified displacement amplitude predicted by the finite element model at this frequency. Frame resonances were seen both in samples measured in the free field and in the impedance tube.

Many modeling efforts have been proposed to explain acoustic losses as functions of the foam's physical parameters. A simplified model to capture both of these effects was given by Kosten and Janssen [68]. The foam was considered to be very porous and very flexible, in which case two complex frequency dependent parameters (density and bulk modulus) can be computed. A more sophisticated theory, known as the Biot-Allard theory [65, 69–71] can be used to compute dissipation in multiple fluid and structural borne waves. For very stiff foams, this theory can be simplified to only include the thermal and viscous effects [44, 45]. Many of these models can be difficult to utilize because they require knowledge of the foam structural, geometrical, and transport properties. Simpler empirical models, for example the Delany and Bazley model [72], can estimate acoustic absorption in fibrous materials by correlating the characteristic impedance and wave number of the material to one physical parameter, flow resitivity. Brennan [73] developed expressions for effective density and bulk modulus of a rigid frame porous medium using lumped element concepts, in which there are certain regimes for which the entire foam sample resembles an acoustic mass, stiffness, or dashpot.

Researchers have developed a number of ways to improve sound absorption in lightweight, structural materials. For example, the acoustic effects of filling sandwich panels with strands of glass fiber was investigated by Yang et al. [74]. The filled sandwich panels had shifted resonances for the sound absorption coefficient, but did not have significant improvement broadband (e.g., see their Figure 4b). For closed cell metallic foams, absorption was improved by hole drilling and rolling processes, which increased viscous and thermal losses at the metal interface [21]. A metallic foam filled with multiple layers of solid PU (not foam) was developed as a composite for use in underwater absorption [75]. The absorption mechanism was hypothesized to be locally resonant metal-polyurthane-metal cells, with varying characteristic dimensions

that gave rise to broadband absorption.

The composite discussed in this chapter is different than the concept of double porosity media in the literature [20, 76]. Double porosity media usually refer to a single medium which has two characteristic pore sizes, occurring when the frame of the porous material is also porous, but at a smaller size scale. In contrast, the composite proposed here has 2 materials and 2 porosities.

This chapter is organized as follows. In the next section, the materials, fabrication methods, and test methods are described. Experimental results for normal incidence acoustic absorption coefficient are presented in Section 4.1.3. In Section 4.1.4, a simplified lumped parameter model is used to model acoustic losses in metal foam, polyurethane foam, and the composite foam. The physical mechanisms of the absorbed power are discussed in Section 4.1.5. Application of a rigid-framed, ideal porous model is investigated in Section 4.1.6, and in Section 4.1.7 is the conclusion.

4.1.2 Materials and Methods

Duocel aluminum metallic foam samples with 10 and 40 pores per inch (PPI) and with a nominal void fraction of 0.91 were obtained from ERG Aerospace for this study. The foam samples were cut using electrical discharge machining into cylinders 34.92 mm outside diameter by 48.00 mm length. A polyurethane foam (FlexFoam-iT!^{TM} III, Smooth-On), referred to as flex foam in this chapter, was also obtained. Flex foam is a pourable foam which expands approximately 15 times the volume during the curing process. A flex foam sample of approximately 34.92 mm outside diameter by 48 mm length was also prepared by pouring the foam into an appropriately sized mold and allowing it to cure.

A composite foam, consisting of flex foam embedded into the pores of the metallic foam was prepared for both the 10 and 40 PPI samples. The small pores in the metal foam produce high flow resistance for the liquid flex foam (prior to curing). In

order to fully saturate the metal foam, it was placed in a cylindrical casting chamber where a plunger was used to apply a pressure to force the liquid through the entire metal structure. The flex foam was allowed to expand and cure, and then excess was trimmed.

The surface impedance and normal incidence acoustic absorption coefficient of all samples was measured at Acentech in Cambridge, MA, according to ASTM Standard E1050-12 [47]. The metal foam and flex foam samples were tested first; composites were fabricated from the same metal foam samples and later tested.

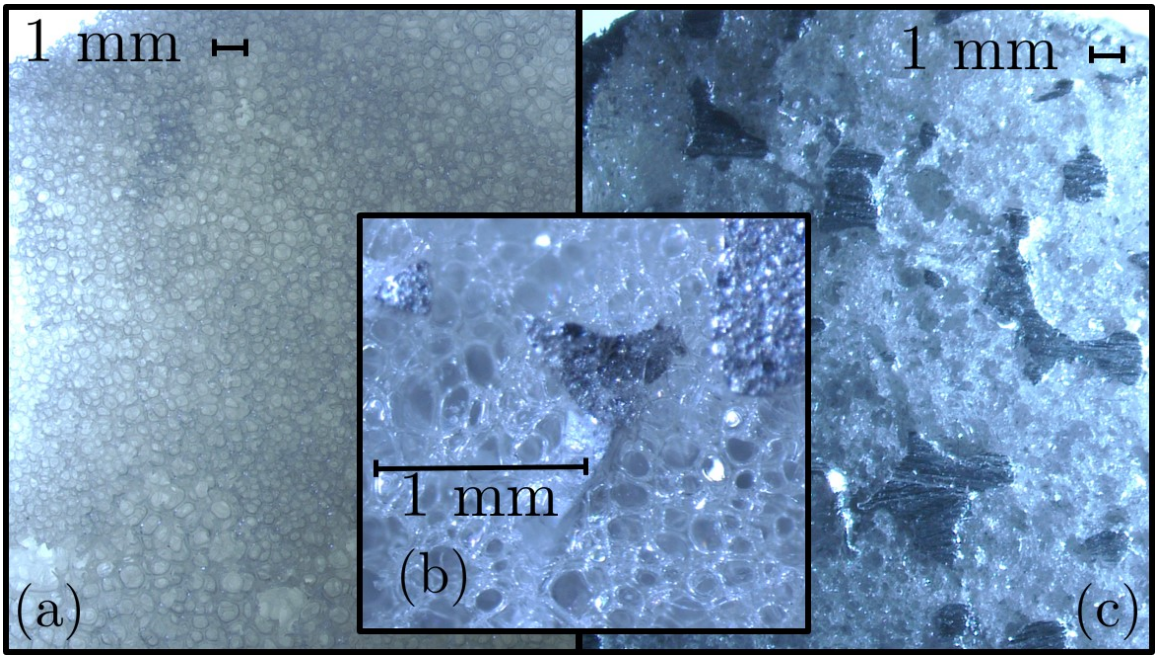

Figure 4·1: Optical microscope images of (a) pure flex foam, (b) zoomed in 10 PPI composite filled with flex foam, and (c) 10 PPI composite filled with flex foam.

After testing, all samples were sliced down the center length-wise, and imaged under an optical microscope (Figure 4·1) to confirm full saturation of the flex foam into the metal foam. From Figure 4·1, it is clear that the flex foam has much smaller pores (sub mm) compared to the metal foam. Furthermore, it was seen that flex foam has a partially reticulated microstructure. There was evidence that the faces of some

pores were completely sealed off with a thin membrane. Other faces were partially open. Also, on inspection of the composite, the flex foam had bonded consistently to the metal around the interface.

4.1.3 Experimental Results

The normal incidence, sound absorption coefficient for flex foam is plotted in Figure 4·2. The shaded region represents measured uncertainty in absorption when flipping the sample end for end. The flex foam has a relatively high sound absorption, greater than 0.8 for most of the frequency range. There is a low frequency resonance around 680 Hz. that is characteristic of a quarter wavelength elastic frame resonance [20].

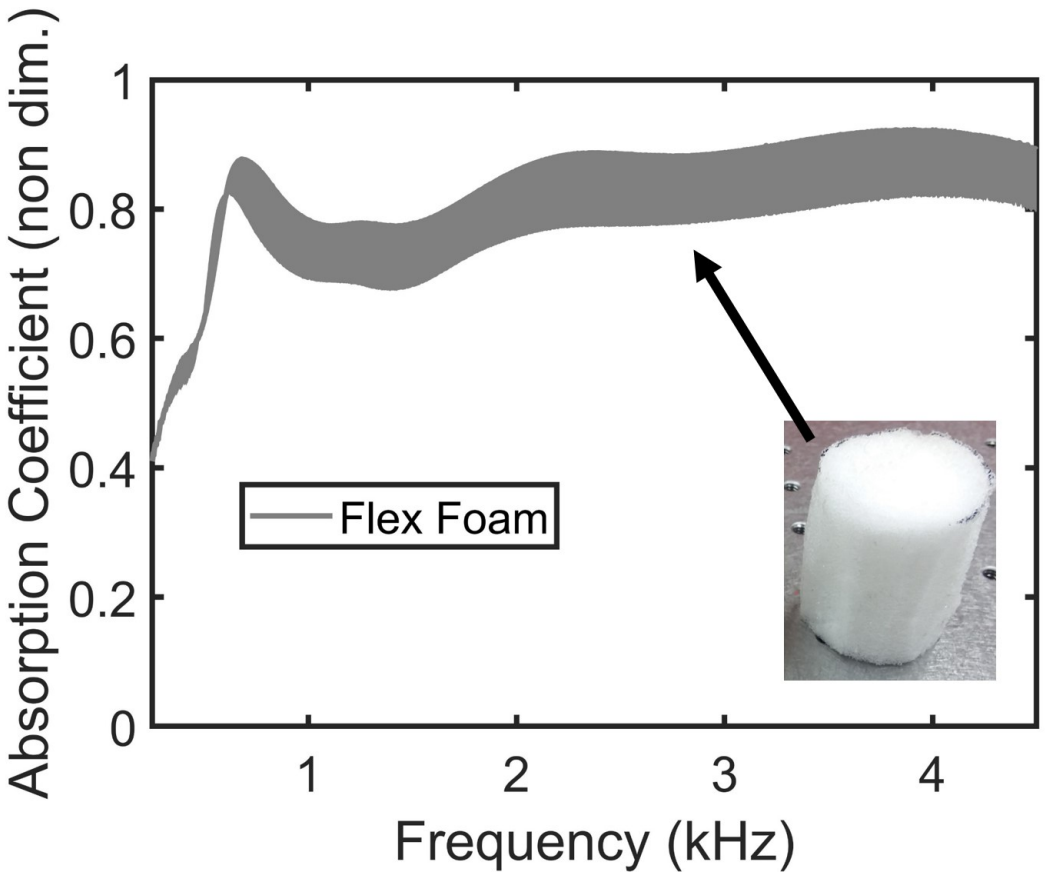

Figure 4·2: Measured absorption coefficient of flex foam, layer thickness of 48 mm. Shading represents measured absorption variation from flipping sample end for end.

Figure 4·3 shows the measured sound absorption for the 10 PPI metal foam and 10 PPI filled composite foam. For the filled composite, again the shaded region represents measured uncertainty in absorption when flipping the sample end for end. The metal foam showed nearly identical absorption when flipped end for end (indicated by nearly no shading). The composite foam retained the low frequency resonance of flex foam. This improved the sound absorption approximately 6 times (from 0.1 to 0.6) in the low frequency test range, around 600 Hz. In the broadband response, the sound absorption improved by a factor of about 2.

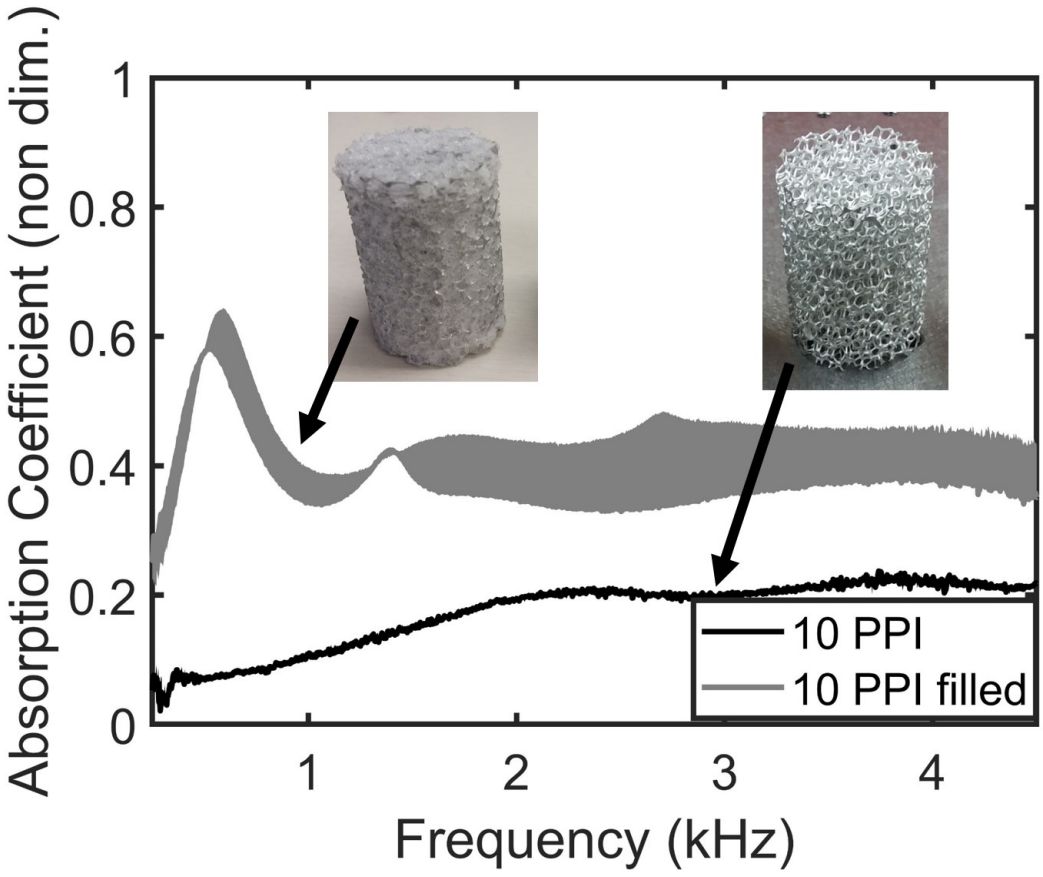

Figure 4·3: Measured absorption coefficient of 10 PPI metal foam and 10 PPI filled composite foam, layer thickness of 48 mm. Shading represents measured absorption variation from flipping sample end for end.

Lastly, Figure 4·4 shows the measured sound absorption coefficient for the 40

PPI metal foam and the 40 PPI filled composite foam. Again, there is a significant improvement in sound absorption at low frequencies, however, not as dramatic of an increase in the broadband response.

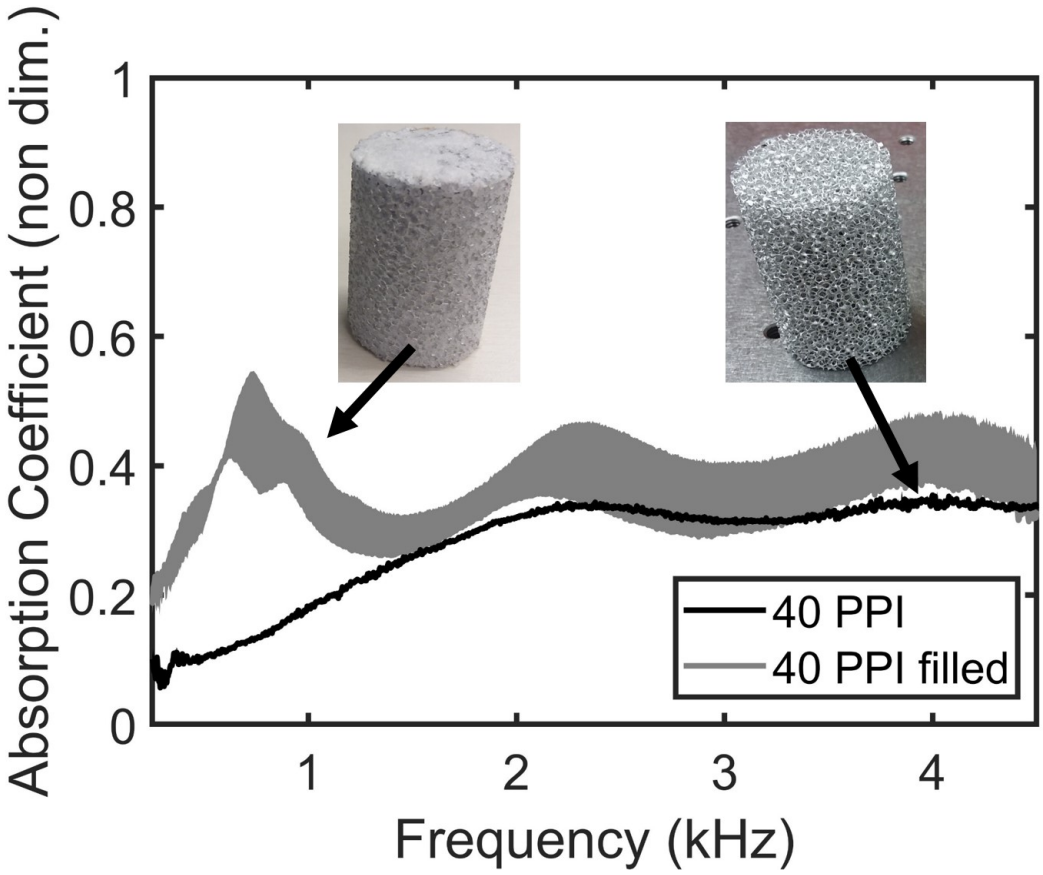

Figure 4·4: Measured absorption coefficient of 40 PPI metal foam and 40 PPI filled composite foam, layer thickness of 48 mm. Shading represents measured absorption variation from flipping sample end for end.

In the next section, a lumped element model will be used to independently analyze the sound absorption mechanisms.

4.1.4 Lumped Element Models

In this section, a lumped element model for the flex foam is developed. The model is then simplified to deal with the case of a rigid foam and extended to deal with the

case of the composite foam. Finally, the results of all three models are compared to experimental measurements.

Flex foam: complex lumped element model

Consider a porous material consisting of air and skeletal frame. A longitudinal wave can propagate in both the air and the frame (a shear wave is assumed not to propagate due to normal incidence) [69–71]. Figure 4·5 is a schematic of a lumped parameter model meant to capture both of these waves. The model can have N chains; the top chain represents air (subscript a) and the bottom chain represents the frame (subscript f). The entire sample has cross sectional area A, length L, void fraction, ϕ, densities of air and the frame ρ_a and ρ_f and bulk moduli K_a and K_f. The individual spring stiffness of air, k_a, is calculated by splitting up the entire stiffness of air in the volume over all the chains (series arrangement, $k_a = NK_aA\phi/L$). The stiffness is assumed to be a real number for air. In a similar way, the mass of air is computed based on sample dimensions and divided among each chain ($m_a = \rho_aAL\phi/N$). The force is applied to the end of both masses. The end masses are not fixed together, both maintain independent degrees of freedom.

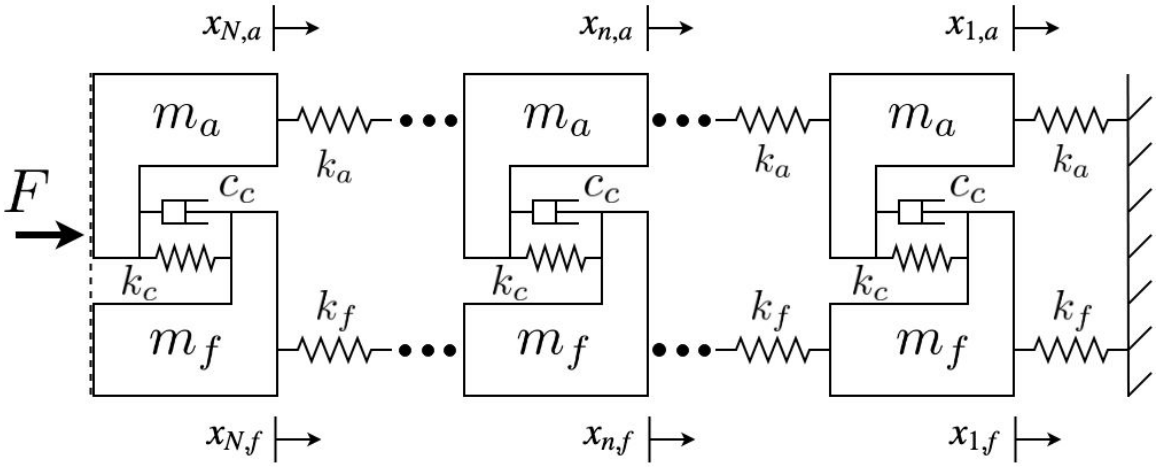

Figure 4·5: Lumped element model for sound propagation for flexible, porous media saturated with air.

For the frame, effective springs and masses can be computed the same way, however the spring constant can be complex to include structural damping.

For a flexible porous material, the movement of air is coupled to the displacement of the frame moving around it. The relative motion between the air and frame is controlled by a dashpot c_c and spring k_c. For air, the coupling spring is taken to be zero, however if both phases were solids, the coupling spring k_c would model the bond at the material's joining interface. The dashpot models the viscous and thermal losses that occur when the air moves past the frame.

The parameters used in this model are given in Table 4.1. Most of the parameters can be directly measured or easily calculated using the material properties and sample dimensions. The bulk modulus of polyurethane was estimated using a measurement of the foam modulus and mass scaling laws [5]. The loss factor was taken to be 0.5 which is in the range of reported measured values for similar types of foam [60]. The coupling dashpot was a manually fitted parameter in this model. The number of stages was initially chosen to be $N = 96$, to model approximately one pore of polyurethane foam per stage.

Table 4.1: Parameters used in lumped parameter model for flex foam (fit parameters are marked).

density of air	ρ_a	1.2	kg/m^3
cross sectional area	A	9.6×10^{-4}	m^2
length	L	0.048	m
bulk modulus of air	K_a	1.41×10^5	Pa
volume fraction of air	ϕ	0.933	-
stage air spring stiffness	k_a	2.5×10^5	N/m
stage air mass	m_a	5.36×10^{-7}	kg
stage coupling dashpot (fit)	c_c	0.0313	N s/m
number of stages	N	96	-
bulk modulus of polyurethane	K_f	10×10^6	Pa
density of polyurethane	ρ_f	1065	kg/m^3
loss factor (fit)	η	0.5	-
stage flex spring stiffness	k_f	$1.28 \times 10^6(1 + .5i)$	N/m
stage flex mass	m_f	3.42×10^{-5}	kg
stage coupling spring	k_c	0	-

Metal foam: rigid frame model

For a rigid frame material, the model can be simplified to Figure 4·6. There is no coupling spring for the rigid frame and air ($k_c = 0$) and the frame stiffness k_f appears infinite. This grounds the coupling dashpot. Furthermore any disturbance will only excite the air chain, thus the displacement of the free end of the sample is x_{Na}. The only unknown is the coupling dashpot, which represents the viscous and thermal loss that occur between the air and the rigid frame. The parameters used in this model are given in Table 4.2. The number of stages was initially chosen to be $N = 12$, to model one pore per stage of the 10 PPI foam (4 mm pore diameter). It should also be noted that for the rigid model considering no damping, the model would converge to the wave equation as $N \to \infty$.

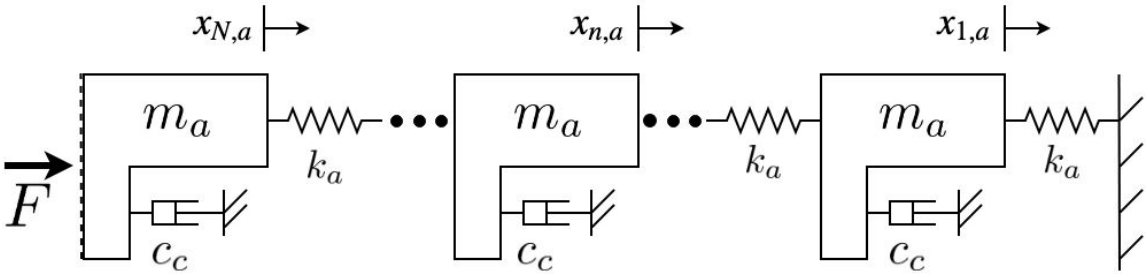

Figure 4·6: Lumped element model for sound propagation for rigid, porous media saturated with air.

Table 4.2: Parameters used in lumped parameter model for a the metal foam rigid frame models (fit parameters are marked).

density of air	ρ_a	1.2	kg/m^3
cross sectional area	A	9.6×10^{-4}	m^2
length	L	0.048	m
bulk modulus of air	K_a	1.41×10^5	Pa
volume fraction of air	ϕ	0.91	-
stage air spring stiffness	k_a	2.56×10^3	N/m
stage air mass	m_a	4.18×10^{-6}	kg
stage coupling dashpot (fit) $\times 10^{-3}$	c_c	3.3 [10PPI]; 5.4 [40 PPI]	N s/m
number of stages	N	12	-

Composite foam: extension of the complex lumped element model

Consider the flex foam embedded into metallic foam. This is now a 3 medium problem, consisting of air, polyurethane, and metal. One could construct a lumped element model consisting of 3 chains. From the rigid frame analysis presented earlier, it can be seen that the effect of the rigid material is to add a grounding dashpot and spring to the mass of the embedded material. Since the metal foam can couple to the air and the flex material, 2 additional coupling systems are added to the complex model, as shown in Figure 4·7. Since the air is not attached to the metal, the coupling spring is zero, the same as the rigid case. However since the flex foam is bonded to

the metal foam, there can be both a coupling spring and dashpot. The composite material is broken up into $N = 96$ stages, again, one pore of flex foam is represented by each stage. Not every stage will get grounded by the metal foam, only stages that correspond to the spacing of the metal foam pores. For example, the 10 PPI foam has a pore diameter of 4 mm, so every 12 out of 96 stages is grounded by the metal. The parameters used in this model are given in Table 4.3.

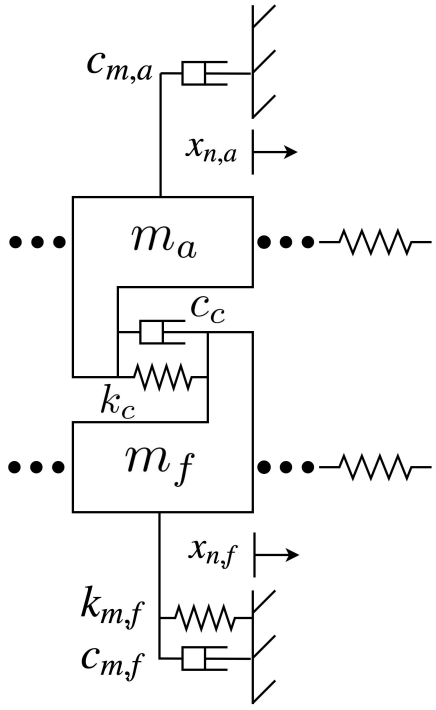

Figure 4·7: Modification of complex model in Figure 6, for section of the composite foam in contact with metal foam.

Table 4.3: Parameters used in lumped parameter model for composite foams (fit parameters are marked).

density of air	ρ_a	1.2	kg/m^3
cross sectional area	A	9.6×10^{-4}	m^2
length	L	0.048	m
bulk modulus of air	K_a	1.41×10^5	Pa
volume fraction of air	ϕ	0.85	-
stage air spring stiffness	k_a	2.09×10^5	N/m
stage air mass	m_a	4.44×10^{-7}	kg
stage coupling dashpot (fit)	c_c	0.0313	N s/m
number of stages	N	96	-
modulus of polyurethane	K_f	10×10^6	Pa
density of polyurethane	ρ_f	1065	kg/m^3
loss factor (fit)	η	0.5	-
stage flex spring stiffness	k_f	$1.17 \times 10^6(1 + .5i)$	N/m
stage flex mass	m_f	3.1×10^{-5}	kg
stage coupling spring	k_c	0	-
metal/air coupling dashpot (fit)	c_{ma}	3.5 [10 PPI] 2.5 [40 PPI]	N s/m
metal/frame coupling dashpot (fit)	c_{mf}	0.02 [10 PPI] 0.05 [40 PPI]	N s/m
metal/frame coupling spring (fit) $\times 10^3$	k_{mf}	1.0 [10 PPI] 1.2 [40 PPI]	N/m
volume fraction of metal	ϕ_m	0.091	-

Modeling results

The equations of motion for the lumped element models can be assembled into the global system $\mathbf{F}(\omega) = \mathbf{D}(\omega)\mathbf{x}(\omega)$, where $\mathbf{F}$ is the forcing vector, $\mathbf{D}$ is the dynamic stiffness matrix, and $\mathbf{x}$ is the displacement vector. For the rigid model, the dynamic stiffness matrix is

$$\mathbf{D}(\omega) = \begin{bmatrix} \Delta_a & -k_a & \mathbf{0} \\ -k_a & \ddots & \ddots \\ \mathbf{0} & \ddots & \Delta_a - k_a \end{bmatrix}$$

where the displacement vector corresponding to degrees of freedom in Figure 4·6

is

$$\mathbf{x} = \begin{bmatrix} x_{1,a} \\ x_{n,a} \\ x_{N,a} \end{bmatrix}$$

and $\Delta_a = -\omega^2 m_a + i\omega c_c + 2k_a$. For the flex foam, the dynamic stiffness matrix is

$$\mathbf{D}(\omega) = \begin{bmatrix} \Delta_a + k_c & -i\omega c_c - k_c & -k_a & \mathbf{0} & \mathbf{0} & \mathbf{0} \\ -i\omega c_c - k_c & \Delta_f + k_c & 0 & -k_f & \mathbf{0} & \mathbf{0} \\ -k_a & 0 & \ddots_a & \ddots_a & \ddots_a & \mathbf{0} \\ \mathbf{0} & -k_f & \ddots_f & \ddots_f & \ddots_f & \ddots_f \\ \mathbf{0} & \mathbf{0} & \ddots_a & \ddots_a & \Delta_a - k_a + k_c & \ddots_a \\ \mathbf{0} & \mathbf{0} & \mathbf{0} & \ddots_f & \ddots_f & \Delta_f - k_f + k_c \end{bmatrix}$$

where the displacement vector corresponding to degrees of freedom in Figure 4·5 is

$$\mathbf{x} = \begin{bmatrix} x_{1,a} \\ x_{1,f} \\ x_{n,a} \\ x_{n,f} \\ x_{N,a} \\ x_{N,f} \end{bmatrix}$$

and $\Delta_f = -\omega^2 m_f + i\omega c_c + 2k_f$. In both systems, $\mathbf{0}$ represents filling the remainder of the matrix of appropriate dimensions with zeroes. In this formulation, rows alternate degrees of freedom from 1:N, the number of stages for the air and the polyurethane. This is designated by $\ddots_a$ and $\ddots_f$, respectively, which indicate repetition of every other row.

The dynamic stiffness matrix for the composite foam is similar to that for flex foam. The difference is that for stages that are grounded by the metal foam, additional terms are added to the diagonal elements. For odd row diagonal elements, the added term is $+i\omega c_{ma}$ and for even row diagonal elements it is $+i\omega c_{mf} + k_{mf}$. Grounded stages correspond to relative size differences between the metal and polyurethane pores, for example the 10 PPI foam has a pore diameter of approximately 4 mm

while the overall sample length is 48 mm, therefore one quarter of the stages are grounded.

To compute the response of the system, a unit force is applied to the Nth degree of freedom and the linear system is solved. Afterward, the acoustical indicators can be computed. For example, for the rigid case the surface impedance is

$$Z_s = \frac{F}{A\dot{x}_{Na}}. \tag{4.1}$$

The absorption coefficient is calculated as

$$\alpha = 1 - |R|^2, \tag{4.2}$$

where R is the reflection coefficient computed by

$$R = \frac{Z_s - Z_{air}}{Z_s + Z_{air}}. \tag{4.3}$$

and Z_{air} is the characteristic impedance of air.

Figure 4·8 shows the normalized surface impedance and absorption coefficient for flex foam predicted by the model overlaid on the experimental measurements. The agreement is evidence that the lumped element model can accurately model the sound absorption. The advantage in using this lumped element model is that the number of unknown foam parameters is greatly reduced.

For example, to use the Biot-Allard theory [65], one would need knowledge of the foams transport properties, e.g. flow resistivity, tortuosity, thermal characteristic length, and viscous characteristic length. These are typically difficult to estimate and measure for a foam without specialized equipment. Using a lumped element model is a simple way to group all the loss mechanisms into one loss constant, the coupling dashpot.

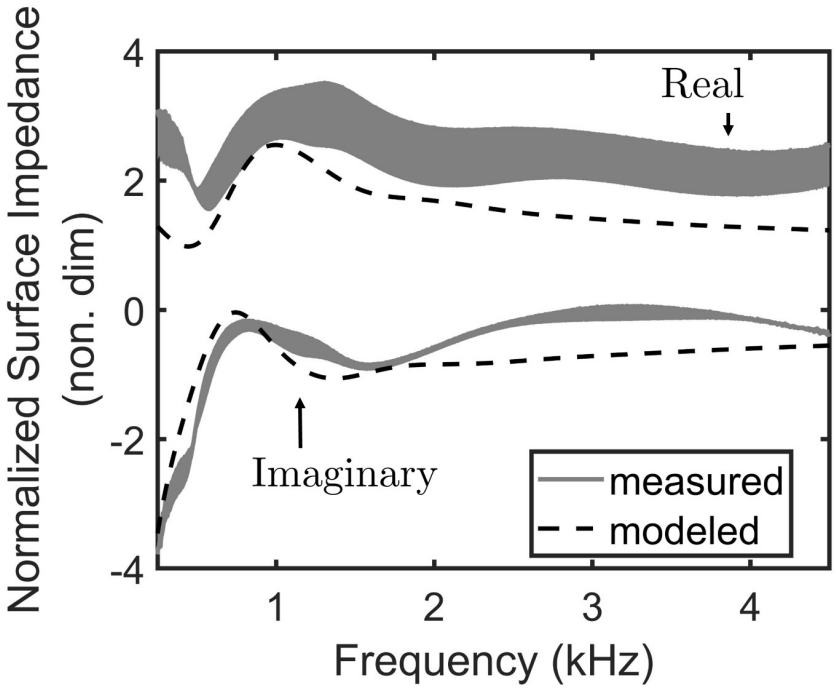

(a) Normalized surface impedance (by air) versus frequency.

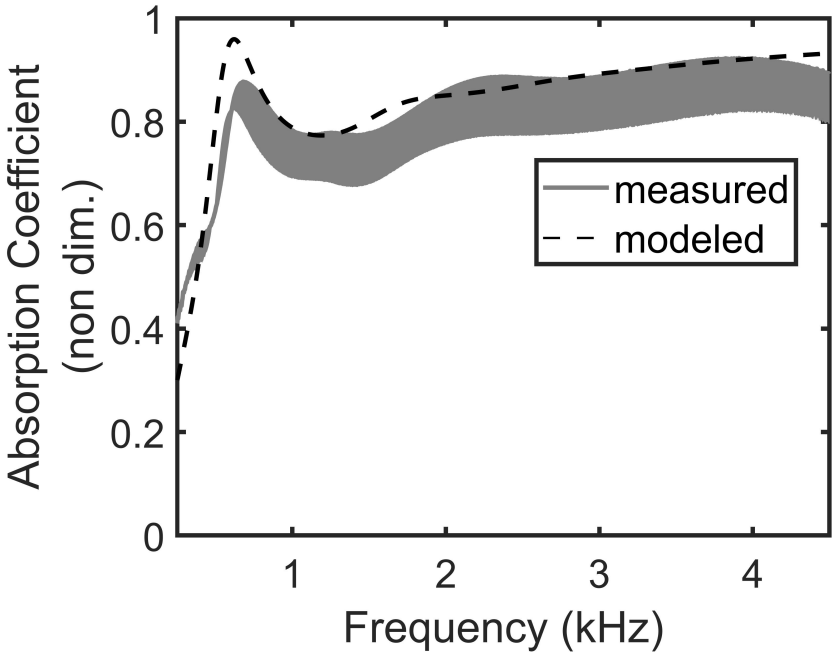

(b) Absorption coefficient versus frequency.

Figure 4·8: Lumped element modeling results for flex foam

Figures. 4·9 and 4·10 show the normalized surface impedance and absorption coefficient predicted by the rigid lumped element model overlaid on the experimental measurements for metal foam. There is a resonance in surface impedance that occurs around 3.6 kHz. For a homogeneous medium, the analytical expression for impedance at a surface, rigidly backed, is $Z = -iZ_0 \cot(kL)$ [20]. Consider a column of pure air, equal in size to the test samples. The first non-zero resonance occurs when cotangent is undefined at $kL = \pi$, where k is the wavenumber and $L = 48$ mm is the sample thickness. Solving for the frequency, one obtains $f = c/(2L) = 3.57$ kHz, where c is the sound speed in air. Thus as expected for the rigid metal foam, it acoustically behaves similarly to a damped air column.

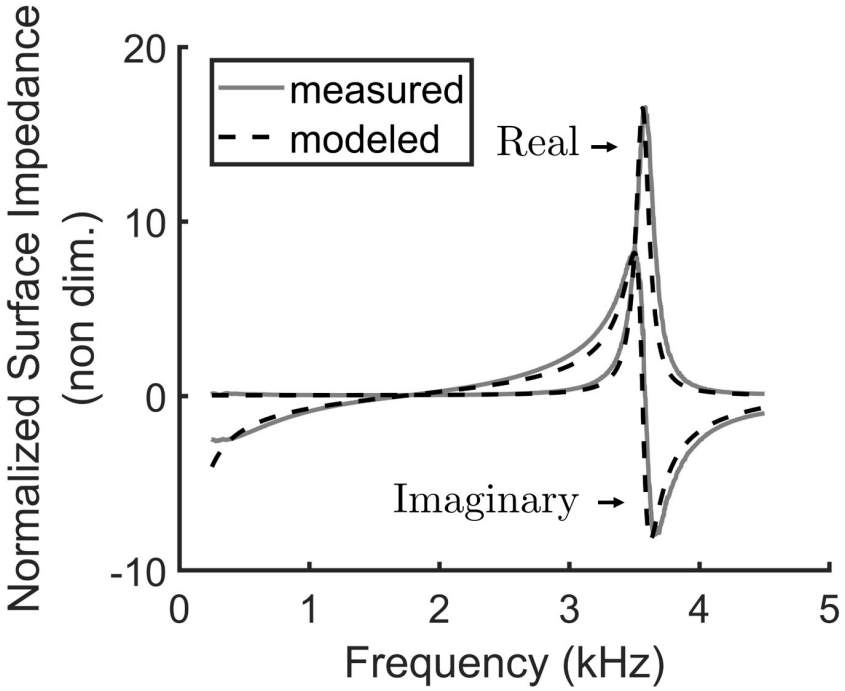

(a) Normalized surface impedance (by air) versus frequency.

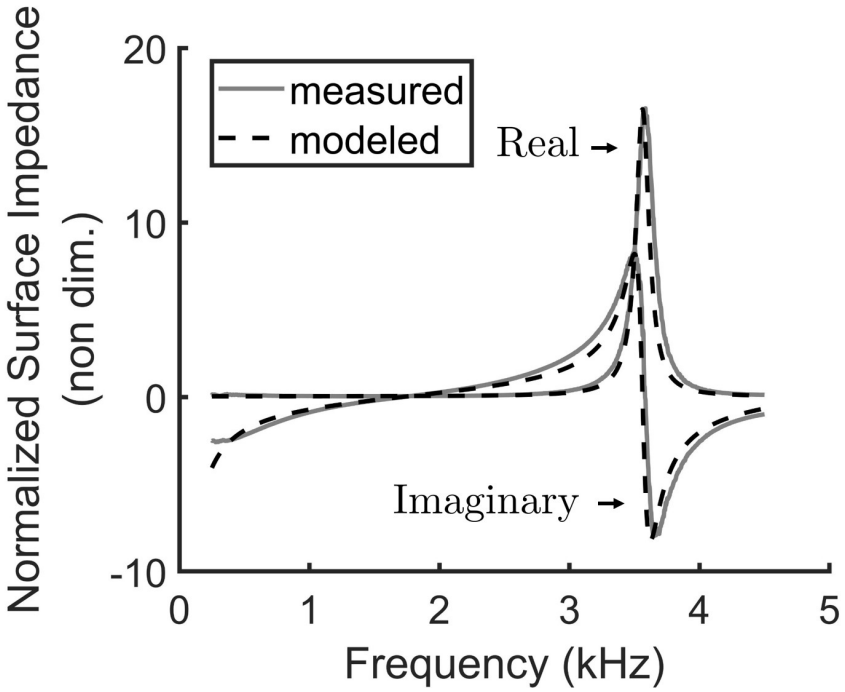

(b) Absorption coefficient versus frequency.

Figure 4·9: Lumped element modeling results for 10 PPI aluminum foam.

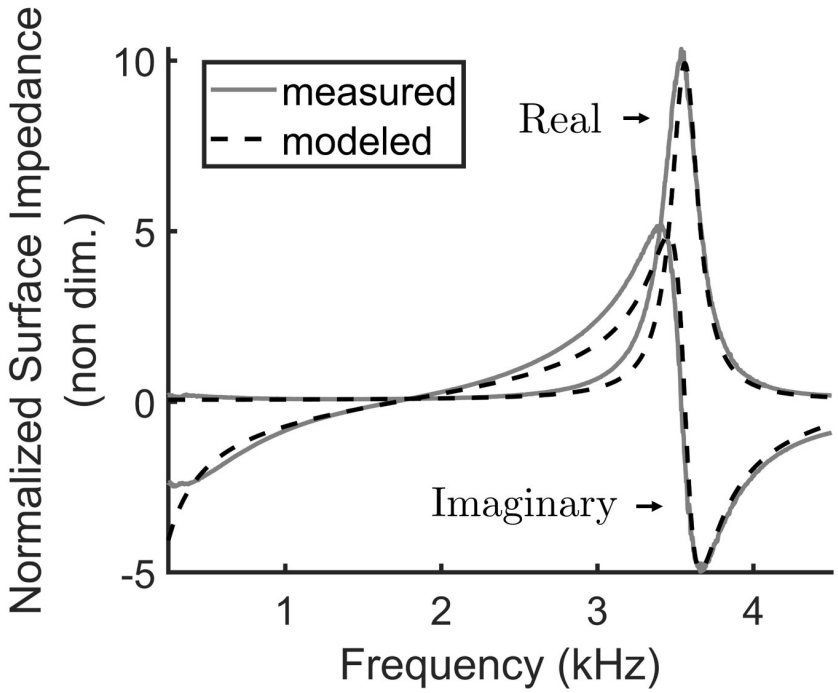

(a) Normalized surface impedance (by air) versus frequency.

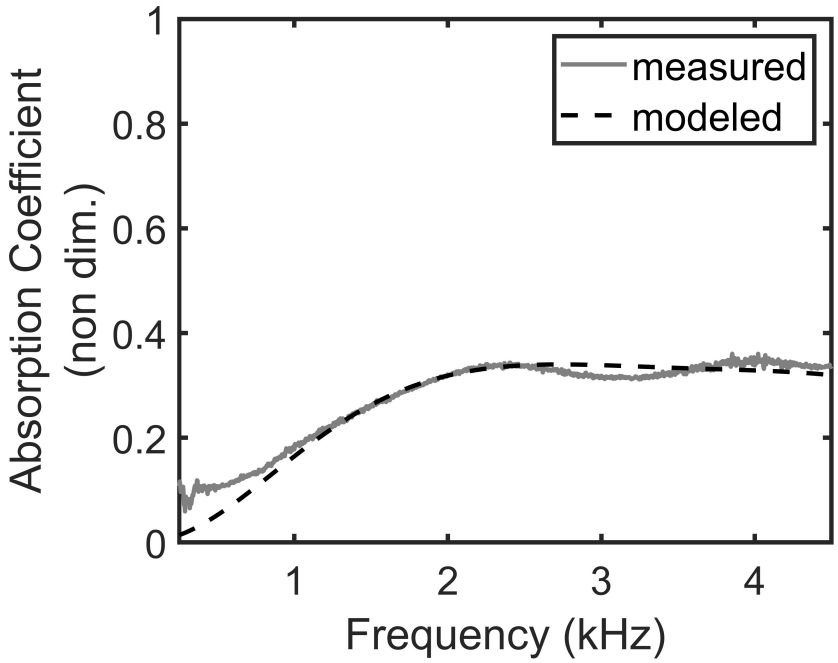

(b) Absorption coefficient versus frequency.

Figure 4·10: Lumped element modeling results for 40 PPI aluminum foam.

Lastly, Figures. 4·11 and 4·12 show the modeling results for the composite foams. Comparing surface impedance of the composites to the pure flex foam in Figure 4·8 (a), it can be seen that the imaginary part remains relatively the same. The largest effect is an increase in the real part of impedance, approximately 4 – 5 times higher for the composite.

There are more unknown parameters for this case, specifically k_{mf}, c_{mf}, c_c and c_{ma}. The coupling dashpot c_c between the flex foam and air is taken to be the same value as for just the pure flex foam case. While the other parameters are fitted, the physical explanation for these lumped elements is clear. The flex foam is bonded to the metal foam at discrete locations. This bond is modeled by containing some stiffness k_{mf} and damping c_{mf}. Furthermore there is now an interaction between air and metal, c_{ma}, and the metal and frame c_{mf}. The relative contribution of each absorption mechanism is not clear by only looking at the magnitude of the dashpot and spring constants. The velocity profiles need to be examined throughout the length of the sample, from which the power loss from each element can be computed and summed, whether it be a structural or viscous loss. This is discussed in the next section.

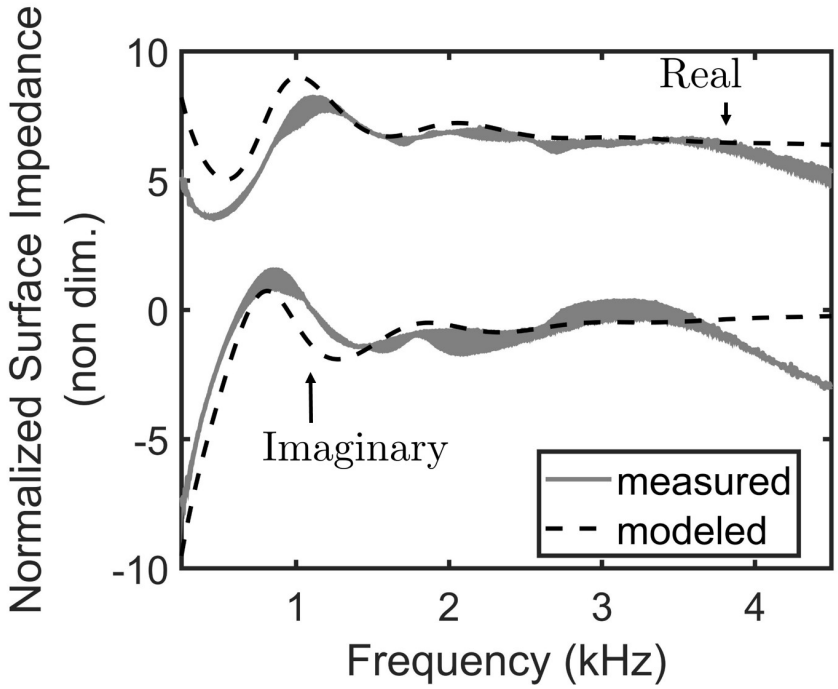

(a) Normalized surface impedance (by air) versus frequency.

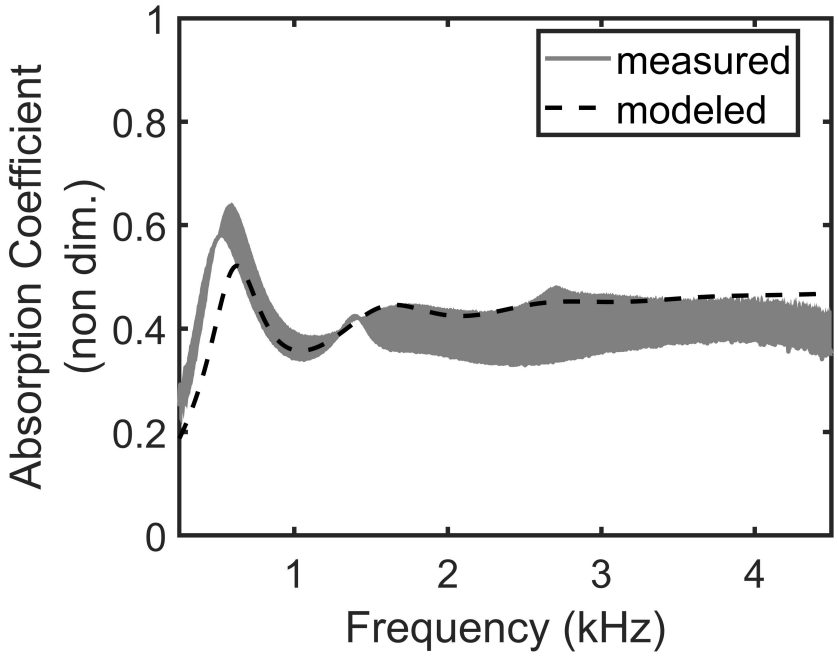

(b) Absorption coefficient versus frequency.

Figure 4·11: Lumped element modeling results for 10 PPI composite foam

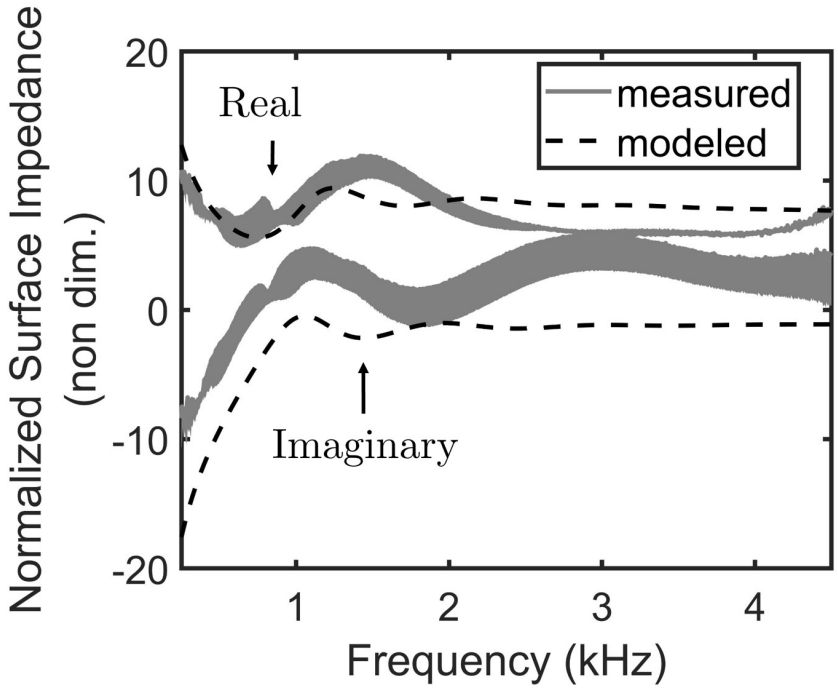

(a) Normalized surface impedance (by air) versus frequency.

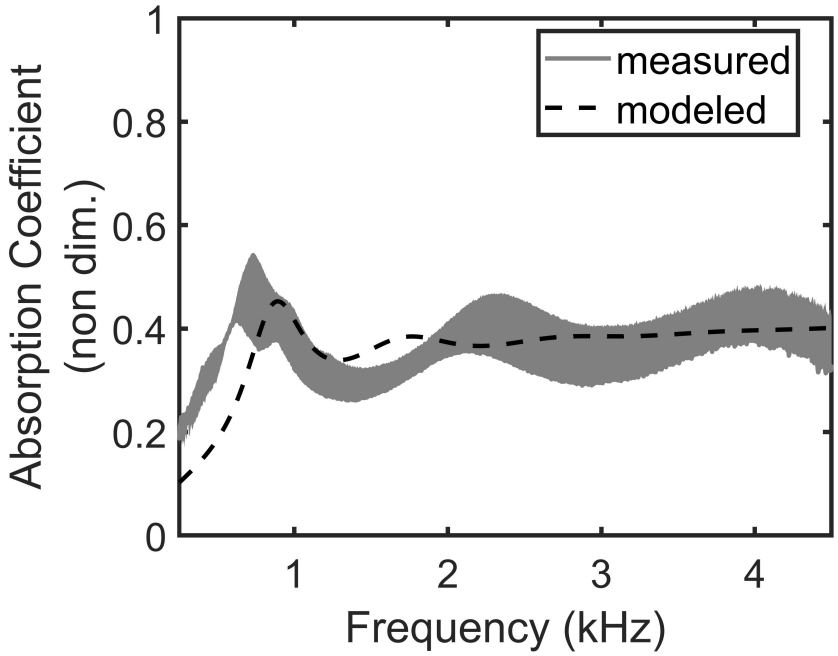

(b) Absorption coefficient versus frequency.

Figure 4·12: Lumped element modeling results for 40 PPI composite foam

4.1.5 Discussion

For the pure flex foam, there are two distinct mechanisms for absorption, the acoustic thermo-viscous effects, and the structural damping effects. The thermo-viscous effects are modeled by one dashpot; the time-average dissipated power can be computed from the complex velocity amplitude, v, by $P = (1/2)\, c_c \mathrm{Re}\{vv^*\}$. The structural damping effects are modeled through a complex stiffness; the time-average power dissipated can be computed by $P = (1/2)\,\mathrm{Re}\{k_f x v^*\}$, where x is the complex displacement amplitude. Note that if k_f were purely real, no power would be absorbed by the spring. The velocity profile is important in determining the relative contribution for each mechanism. Figure 4·13 shows the velocity profile $(20 \log_{10} |v|/|v_{max}|)$ for both the air and the frame. Both profiles are in dB, where the velocity has been normalized to the same maximum velocity v_{max} of both the air and frame over all frequency and space.

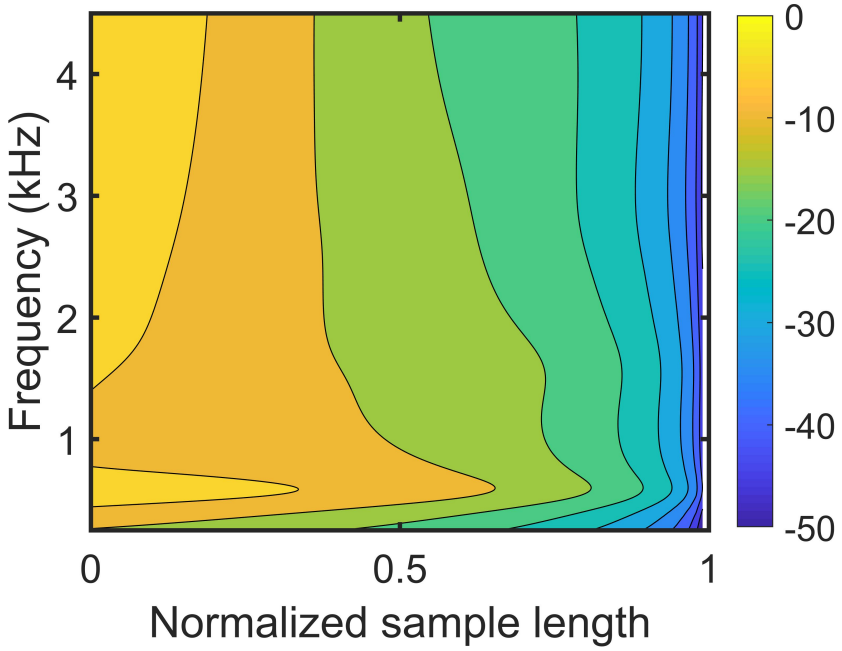

(a) Air

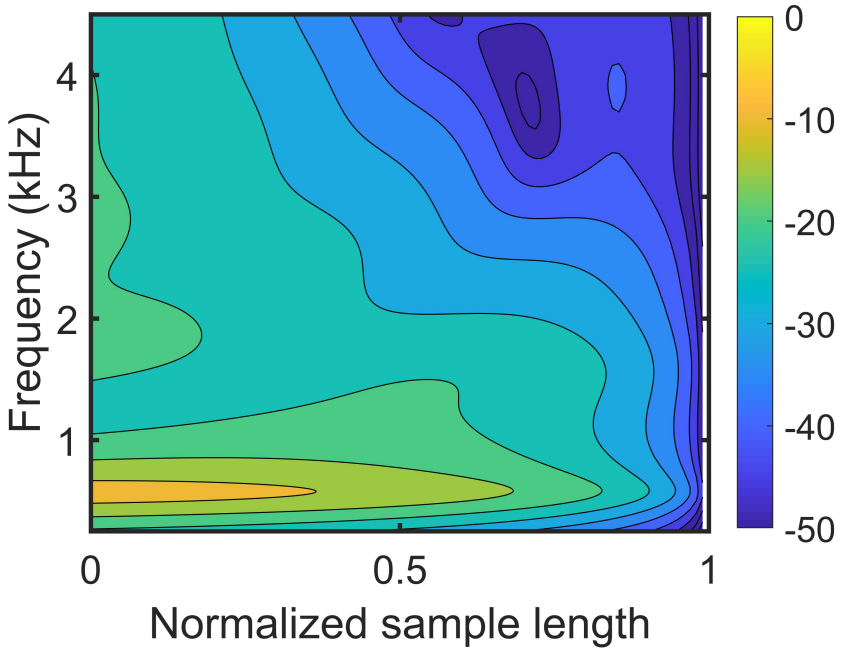

(b) Frame

Figure 4·13: Velocity profile ($20\log_{10}|v|/|v_{max}$) in dB for the flex foam model.

The velocities approach zero at the rigid wall where the normalized sample length approaches 1. The power absorbed by each mechanism is computed individually and normalized by the incident power (which is by definition, the absorption coefficient). This result is shown in Figure 4·14. At low frequency, the structural effects dominate, while at higher frequency, the thermo-viscous effects dominate.

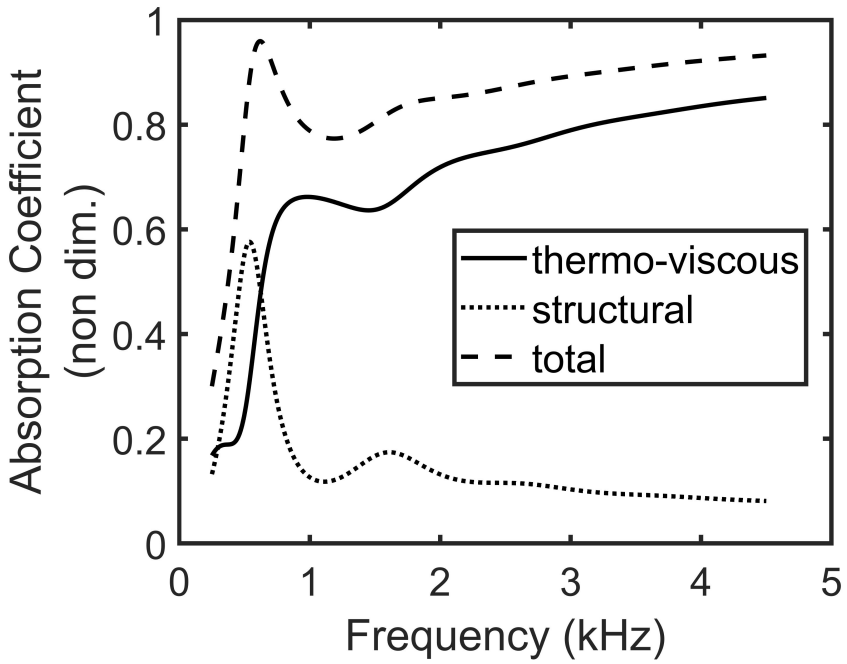

Figure 4·14: Power absorption mechanisms for the flex foam model.

For the metallic foam, all of the absorbed power is attributed to viscous and thermal losses at the air and metal interface. This is modeled by a number of discrete dashpots, positioned throughout the length of the sample. The time-average dissipated power can be computed by $P = (1/2)\, c_c \mathrm{Re}\{vv^*\}$, which is the total dissipated power in this case. Figure 4·15 shows a color contour of the velocity profile over frequency and sample length for the 10 PPI metal foam model (the white space is because the normalized length equal to 1 position is not a degree of freedom in the model nor is the logarithm of the velocity defined; the velocity is zero at the rigid

wall.)

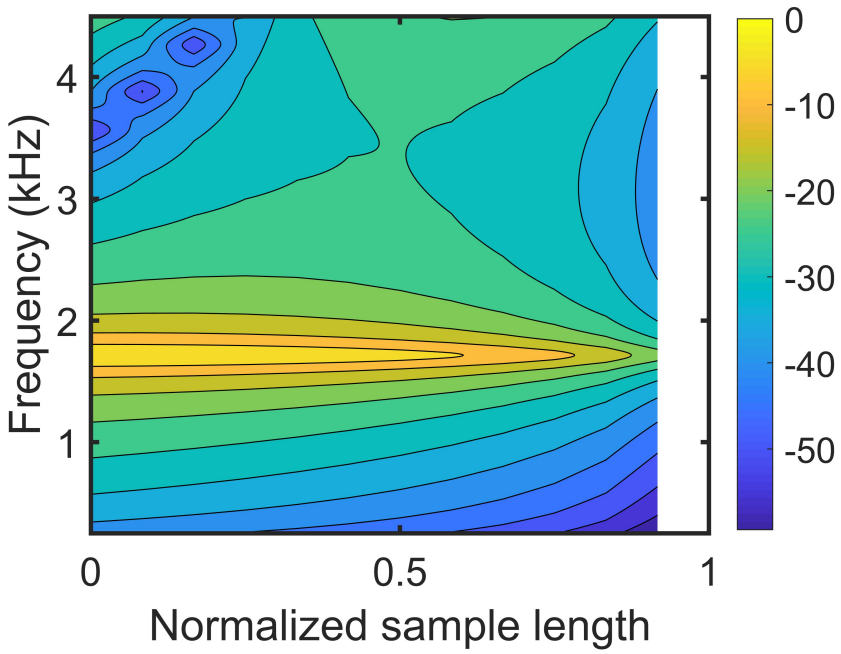

Figure 4·15: Velocity profile ($20\log_{10}|v|/|v_{max}$) in dB for the 10 PPI metal foam model.

The velocity is seen to be maximized near 1.7 kHz. Again, comparing to a column of air, the analytical solution for the standing velocity profile in a homogeneous medium that is rigidly backed is

$$v = \frac{-P_0}{iZ_{air}} \frac{\sin\left(k(L-x)\right)}{\cos\left(kL\right)}, \tag{4.4}$$

where P_0 is a source pressure amplitude. This is maximized for the denominator equal to zero, or $kL = \pi/2$. Solving for the frequency, one obtains $f = c/(4L) = 1.786$ kHz.

For the composite, the 10 PPI model will be considered. The velocity contours are plotted in Figure 4·16. For this case, the velocity of the frame is generally higher than air. There are a total of four distinct power absorption mechanisms that have been identified in the model. Two are the same as pure flex foam, while the additional

two are the metal to air effects and the metal to flex foam bonding effects.

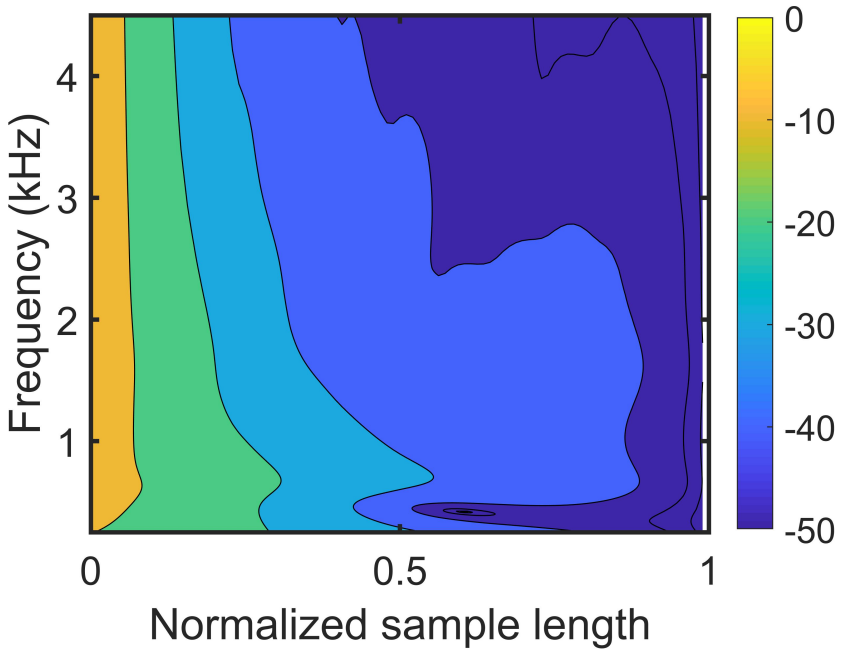

(a) Air

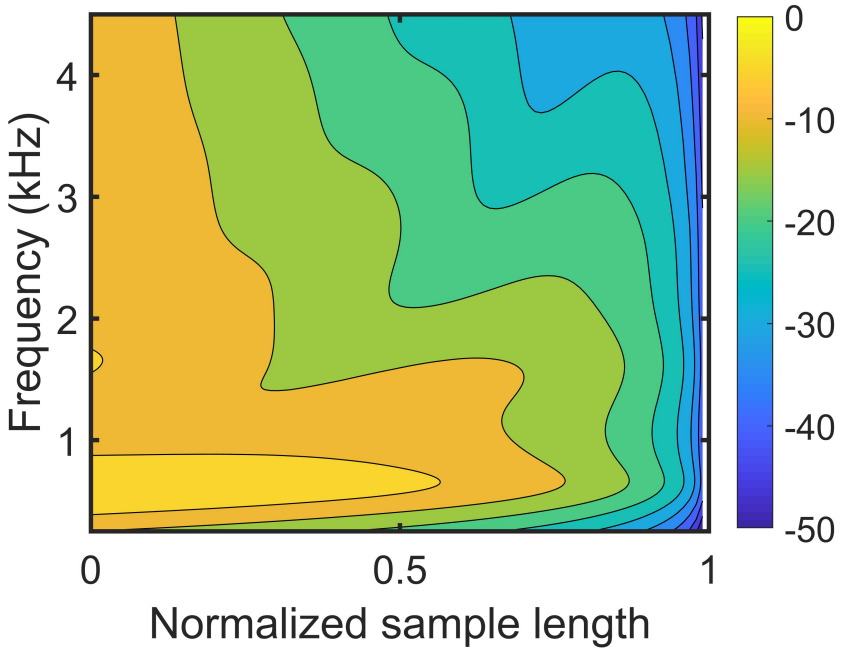

(b) Frame

Figure 4·16: Velocity profile ($20\log_{10}|v|/|v_{max}$) in dB for the 10 PPI composite foam model.

Similarly to what was done with the flex foam, the individual absorbed power for each mechanism is computed and plotted in Figure 4·17.

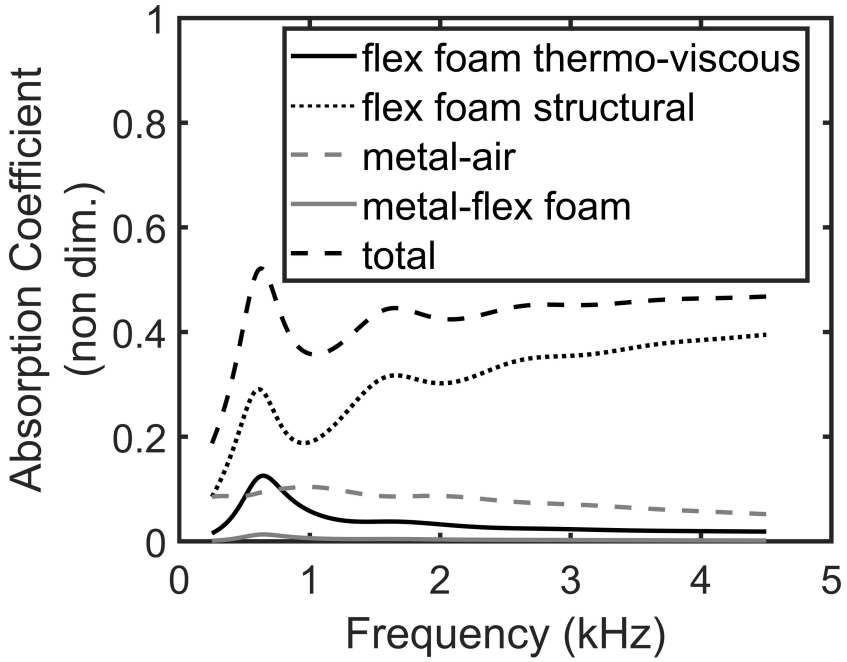

Figure 4·17: Power absorption mechanisms for 10 PPI composite foam model.

For this case, the main absorption mechanism is the structural damping of the flex foam. The effects of the thermo-viscous damping have been greatly reduced in the flex foam. This can be explained physically by considering that the metal greatly reduces the relative velocity of the air and flex foam.

4.1.6 Rigid-Framed Model

In this section, a rigid-framed, two parameter model is used to further study the effects of the composite foam. The model used considers an ideal porous material made up of uniform cylindrical holes [77]. The inputs to the model are only the diameter and porosity, in addition to the standard properties of air. Although this model does not exactly represent the microstructure of the metal and polyurethane

foams, it has been used previously for these types of foams [21], has the advantage of fewer parameters, and can be used to elucidate global trends in sound absorption for composite foams. Other simplified models such as [78] have been shown to very accurately model porous materials provided they follow a log-normal distribution. In the present study, this model was not used, however, because the pore size distribution of the metallic foam is known to follow a bimodal distribution [79]. The composite foam is also not expected to follow a log-normal distribution since it is comprised of the metallic foam and flex foam, with two distinct pore sizes.

A detailed derivation of this model can be found in Chapter 4 of [20]. For this model, the surface impedance is given as

$$Z_s = -iZ_c \cot(kL)/\phi. \tag{4.5}$$

The characteristic impedance Z_c and the complex wave number are

$$Z_c = \sqrt{\tilde{K}\tilde{\rho}}, \qquad k = \omega\sqrt{\tilde{\rho}/\tilde{K}}. \tag{4.6}$$

To compute the complex bulk modulus $\tilde{K}$ and complex density $\tilde{\rho}$ for the fluid-equivalent layer, the following equations can be used:

$$\tilde{\rho} = \rho_a \Bigg/ \left[1 - \frac{2}{s\sqrt{-i}} \frac{J_1(s\sqrt{-i})}{J_0(s\sqrt{-i})}\right] \tag{4.7}$$

$$\tilde{K} = K_a \Bigg/ \left[1 + (\gamma - 1)\frac{2}{Bs\sqrt{-i}} \frac{J_1(Bs\sqrt{-i})}{J_0(Bs\sqrt{-i})}\right] \tag{4.8}$$

where the intermediate variable $s = \sqrt{\frac{8\omega\rho_a}{\sigma\phi}}$ and the flow resistivity $\sigma = \frac{8\eta}{R^2\phi}$ for the circular pores. Furthermore, B is the Prandtl number squared($.707^2$ used for air), γ is the specific heat ratio (1.4 used for air), η is the dynamic viscosity (18.18×10^{-6}N s/m^2 used for air), R is the pore radius, and J_1 and J_0 are Bessel functions of the first kind of order 1 and 0, respectively. Equations (4.2) and (4.3) can then be used to compute

the acoustic absorption.

For this comparison, 3 foams will be identified. Foam A has a porosity of 0.91 and characteristic diameter of 4 mm, similar in scale to the 10 PPI metallic foam. Foam B is scaled similarly to the polyurethane foam, with a porosity of 0.933 and diameter of 0.5 mm. Lastly, foam C represents the composite foam. The composite consists of aluminum and polyurethane foam, with volume fractions of 0.09 and 0.91, respectively. To determine the characteristic diameter, the diameters of foams A and B are weight averaged by volume fraction. The characteristic diameter is computed as

$$d_C = \phi_A d_A + \phi_B d_B \tag{4.9}$$

$$0.82\,\text{mm} = (0.09)(4.0\,\text{mm}) + (0.91)(0.5\,\text{mm}) \tag{4.10}$$

All foams are plotted in the Figure 18, alongside the experimental data.

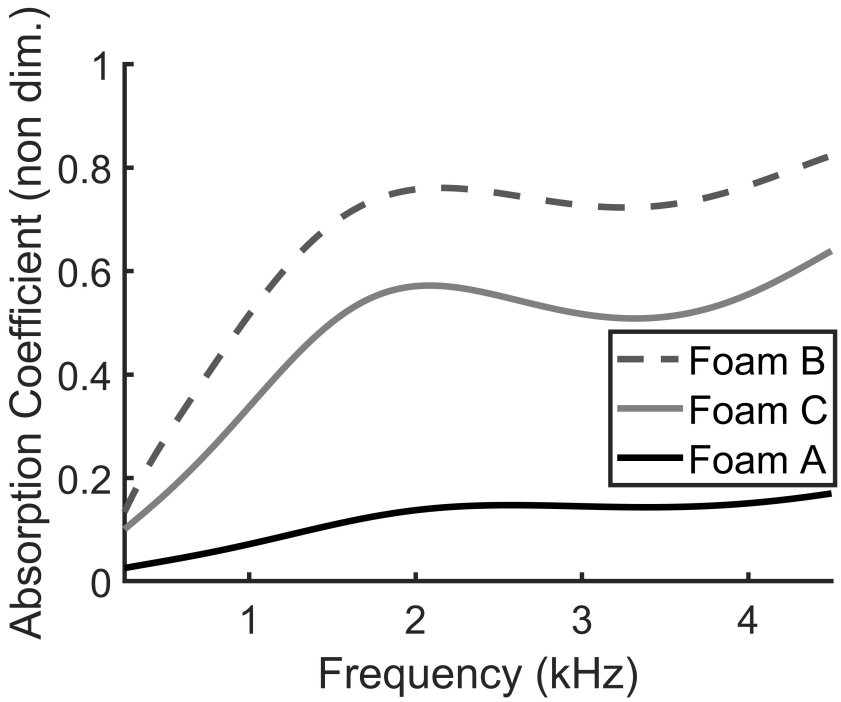

(a) Absorption coefficient versus frequency for the cylindrical pore model.

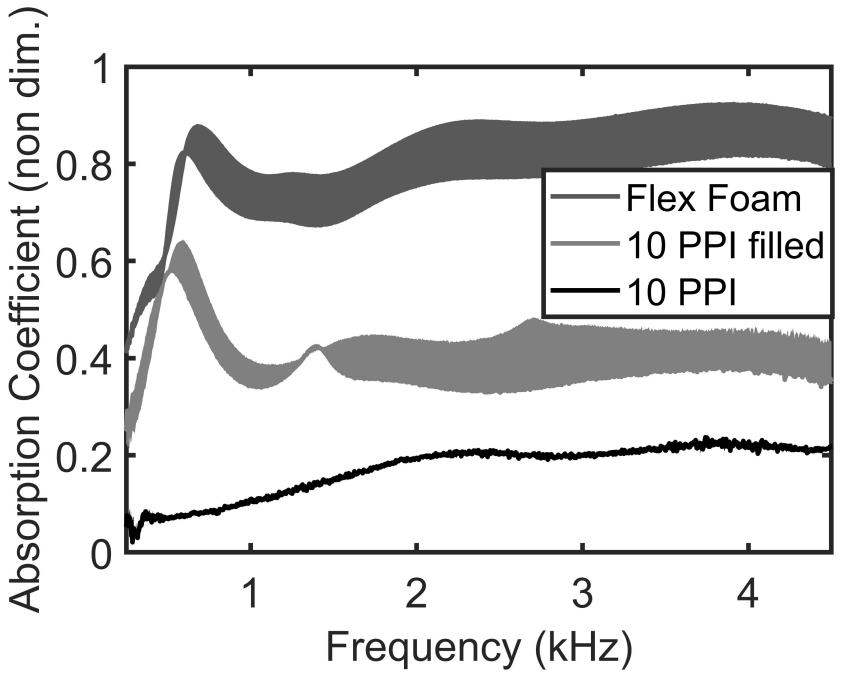

(b) Experimental absorption coefficient versus frequency.

Figure 4·18: Absorption coefficient comparison for the rigid-framed model.

It can be seen that the rigid cylindrical pore model best matches the experimental results for the pure metallic foam (comparing Foam A with 10 PPI). Globally, compared to foam A, the composite foam C has a significantly increased absorption coefficient which is due to the composite being filled with another foam that has a smaller pore size, even thought the volume fraction of air decreases. This is modeled by a decrease in characteristic diameter in foam C compared to foam A, which increases the boundary layer thermal and viscous losses and therefore increases the absorption coefficient. Foam C does not perform as well as foam B because a fraction of the volume is occupied by a different solid material (metal) rather than the porous material, and this lessens the absorption capability of the material.

4.1.7 Conclusion

A composite foam was fabricated by embedding a soft, polyurethane foam into an open-cell metallic foam. The composite retained the high static stiffness of the metal foam while significantly improving the sound absorption compared to metal foam. A lumped element model was used to compute the surface impedance and absorption coefficient for three different types of foams: pure metal foam, pure polyurethane foam, and the composite. The model shows good accuracy compared to experimental measurements and can be used to understand the different absorption mechanisms that occur in foams. Finally, the two parameter rigid cylindrical model used in this section provided insight into acoustic absorption trends for foam-in-foam composites.

4.2 Vibration Damping of Fluid-Saturated Metallic Foam

The remainder of this chapter presents an investigation into vibration damping of metallic foams that are saturated by viscous liquids. For open-cell foams, a fluid is able to completely saturate the metal skeleton. This allows for increased energy transfer and therefore increased damping for a foam that is saturated with a viscous

liquid. Two sets of experiments and analysis are discussed. First, results for steady-state transmissibility for fluid saturated metallic foams are given. Finally, results for transient ring-downs are examined.

4.2.1 Introduction

Some of the first investigations into damping of fluid saturated foams were done by Kosten and Zwikker [12] for sponge rubber. They developed an impedance model to take into account both the effects of the sponge as well as effects of the air based on a piston cylinder arrangement with relief tube. This model is discussed further in detail by Gent and Rusch [13], who identify two frequency regimes of interest. At low frequency, the flow resistivity through the foam pores is sufficiently low that will allow air to be forced through the foam and contribute to damping. At high frequency, the "piston" is moving too fast to force any air through the foam such that the air contributes mostly to added stiffness. They indicate experimentally as well as theoretically that there is a frequency between the two regimes for which the damping is maximized. Modifications to the Gent and Rusch theory were added later in [14] to include inertial effects of vibrating foams. The theory is validated experimentally using a flexible foam saturated with oil.

Limitations of the piston-cylinder model developed by Kosten and Zwikker come from difficulty in mathematically mapping parameters in the model (tube length, radius) to parameters of real foams such as pores size and porosity. Patten et. al [80] developed a mechanistic model of a seat cushion which took into account linear and non-linear damping effects which were linked to the constitutive properties of the foam. This model was used [81] to study vibration transmissibility of conventional as well as negative Poisson ratio foams. Experimental results showed that the foam with negative Poisson ratio had a higher dynamic stiffness and a higher damping ratio. Energy dissipation mechanics in porous solids in terms of Biot theory were

described in a 2006 paper by Goransson [82].

Lastly, a polymer-metal composite foam was fabricated and tested by Yin and Rayess [19]. The composite showed increased stiffness and damping compared to both host materials, however it was only tested up to 2 Hz.

4.2.2 Steady State Vibration

When a structure is subject to base excitation, some of the energy is transmitted through the structure and some of the energy is lost to heat due to damping. To determine the transmitted vibration, a common experimental method is to excite the base of a structure over a desired frequency range and then measure acceleration at the top and at the base of a structure. The ratio of the accelerations is known as the transmissibility. The mass, stiffness, and damping properties of the structure all determine how much energy is transmitted and how much energy is dissipated.

Experimental Setup

The experiments described in this section were designed to enable measurement of steady state vibration transmissibility through fluid saturated aluminum foams subjected to a frequency dependent base excitation. Two inch cube foam samples were specially prepared for these tests. To enable mounting and attaching of masses, aluminum discs (3 inch outside diameter and 1/4 inch thick) were bonded to the top and bottom of foam samples with a two-part, slow-setting structural epoxy. Additionally, the aluminum discs were tapped with 1/4-20 holes at the center. This allowed for threaded connections to masses and support structures. The prepared foam samples are shown in Figure 4·19.

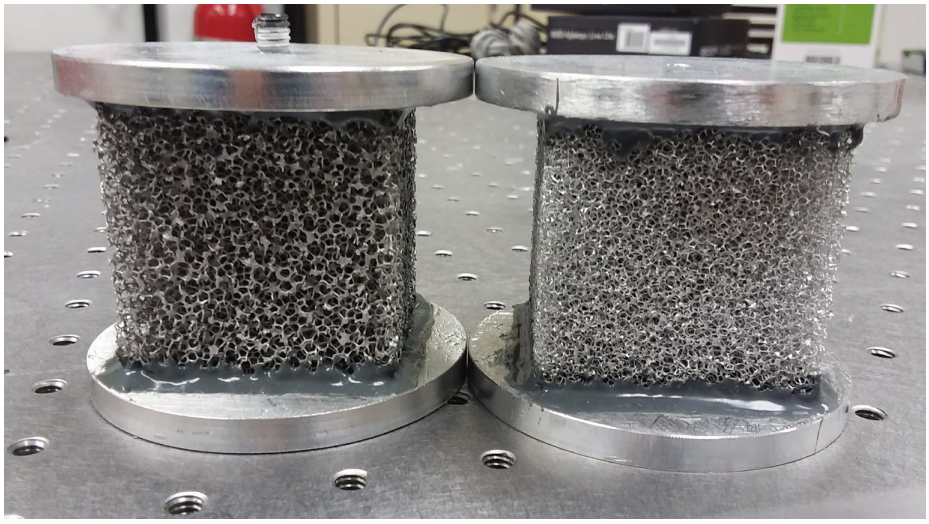

Figure 4·19: 20 PPI (left) and 40 PPI (right) aluminum foam samples bonded to 3 inch diameter aluminum discs. The discs are tapped with 1/4-20 threads allowing the foam to mounted.

The experimental setup is shown in Figure 4·20. The foam was seated in a small tub, approximately 2 liters in volume. The tub had a small through hole and seal at the bottom, which allowed the foam to be fastened to the shaker stinger underneath the tub. Modular steel masses (3 inches outside diameter and 2 inches tall) were also machined with threaded ports on the top and bottom, allowing for interconnecting arrangements of masses to be added on top of the foam.

The entire setup was attached to the shaker by a 4 inch long stinger, approximately 1/8 inch outside diameter. The shaker used in this experiment was a permanent magnetic shaker, model LDS V408, with a specified useful frequency range of 5 Hz - 9 kHz. The shaker was not designed to support any static load. As a result, the entire static weight was loaded on a support structure, which was comprised of an 80/20 frame and rubber padding. This support structure protected the shaker from the high static load while still enabling the shaker to exert a dynamic load. The accelerometers used in this experiment were Brüel & Kjær type 4534-B. They were

mounted with beeswax to the top dead center of the mass and bottom dead center underneath the the foam tub.

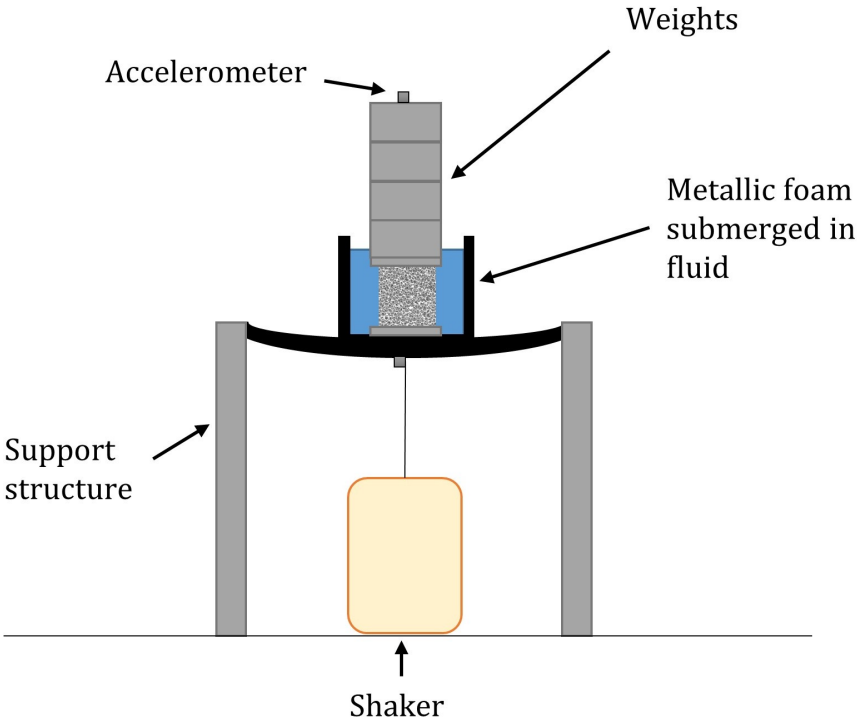

Figure 4·20: Schematic of experimental setup for steady state vibration experiments. The metallic foam is supported from the bottom, attached to a shaker, and placed in a tub allowing for complete fluid saturation.

The shaker was connected to an amplifier type PA500L. Additionally both the amplifier and accelerometer signals were connected to the data acquisition box, module LAN-XI. This acquisition hardware was connected to a desktop computer and had 3 inputs and 1 output, which simultaneously controlled the shaker and recorded acceleration levels from both accelerometers. For the tests described in this section, a payload of approximately 2.7 kg was attached to the foam. The excitation to the shaker was a white noise signal in the range of 5-800 Hz. In this frequency range,

the amplitude of base displacement did not exceed 2 microns. The Brüel & Kjær software PULSE Reflex was used to control the shaker and record the acceleration measurements. Post processing of the data was done in MATLAB.

This experimental setup allowed for many different experiments by varying the saturating fluid. First, a control test was run with air as the saturation fluid. Subsequent tests were done with other saturating fluids by filling and emptying the tub and drying out the foam. Descriptions of the fluids and resulting vibration characteristics are presented in the next section.

Experimental and Analytical Results

An image of the test setup with motor oil as the saturating fluid is shown in Figure 4·21. Five separate tests were run with 5 different fluids: air, motor oil, water, glycerol, and petroleum jelly. For all fluids except the petroleum jelly, it was straightforward to saturate the foam by pouring the liquid and filling the tub. The flow resistivity of the foam was sufficiently low enough to allow these fluids to completely fill the pores. Since the petroleum jelly is a semi-solid, it was first melted down, poured in the foam pores, and then allowed to cure within the foam pores. In a similar way for removal, the foam was heated, changing the petroleum jelly to a liquid and allowing it to drip out.

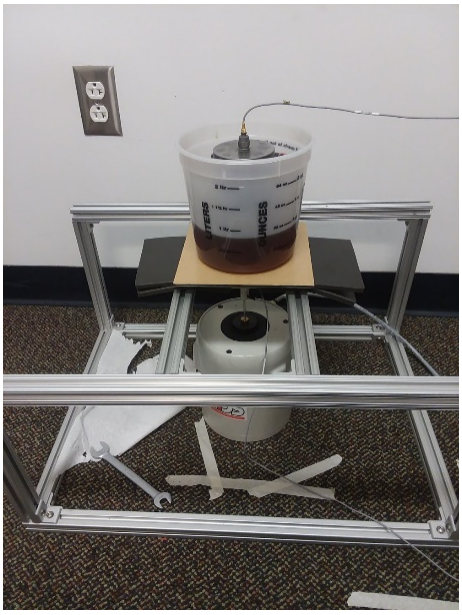

Figure 4·21: Shaker setup with a 20 PPI aluminum foam saturated with motor oil. The mass load is approximately 2.7 kg.

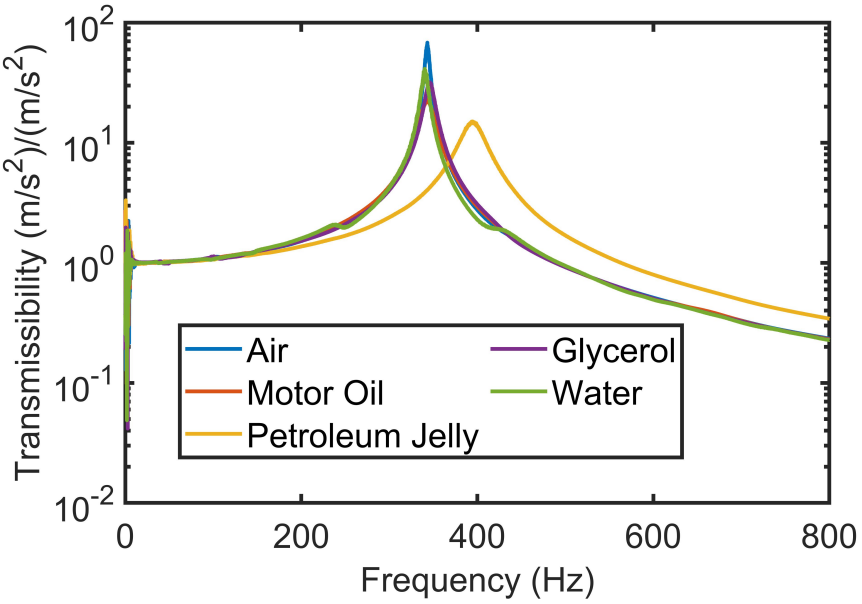

(a)

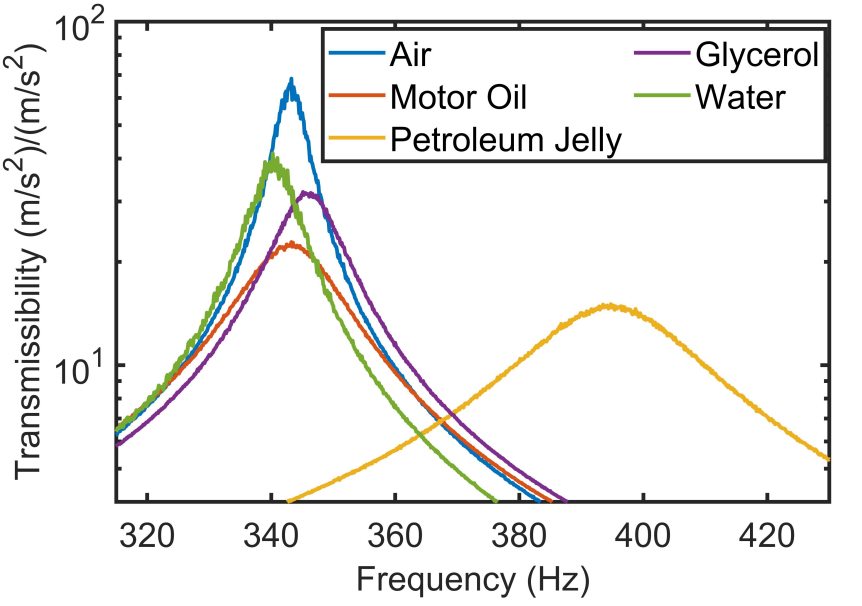

(b)

Figure 4·22: Acceleration transmissibility versus frequency for a 20 PPI aluminum foam saturated with various fluids for (a) the entire test frequency range, and (b) zoomed in near resonance.

The acceleration transmissibility magnitude for the five different saturating materials is shown in Figure 4·22. At low frequency it continues to approach one, indicating a rigid body motion where the top and bottom of the structure move in unison. For all materials there is one resonance, occurring near 340 Hz for all except the petroleum jelly which is near 395 Hz. This resonance is similar in characteristics to the resonance of a single degree of freedom harmonic oscillator, when the base is nearly stationary and most of the energy has been transmitted to the top of the structure, resulting in a local large amplitude of vibration. The frequency of this resonance is determined by the payload mass on the foam as well as the apparent stiffness of the foam. Since the petroleum jelly is a semi-solid, it likely contributes greater to the bulk stiffness of the foam, thereby pushing the resonance to higher frequency.

The magnitude of transmissibility at resonance is determined by the damping. When the foam is vibrating, it is globally compressing and expanding which causes some of the fluid to move relative to the foam. Depending on the viscosity of the fluid, more or less energy may be dissipated to the fluid. Therefore, the entire system may be approximately modelled and understood as a mass-spring-dashpot system excited at its base. In this model, the top weights are the mass, the metallic foam is the stiffness, and the saturating fluid interacting with the metallic foam is the dashpot.

To quantify damping for a transfer function in the frequency domain, the half power bandwidth method method can be used. Considering light damping, the damping ratio, ζ, can be computed by

$$\zeta = \frac{1}{2}\left(\frac{\omega_2 - \omega_1}{\omega_n}\right), \tag{4.11}$$

where ω_n is the natural frequency and ω_1 and ω_2 are frequencies above and below resonance where the amplitude drops by a factor of $(1/\sqrt{2})$ (3 dB). The computed damping ratios as well as approximate fluid properties are given in Table 4.4.

From the table, it is clear that the metallic foam saturated with petroleum jelly has the highest damping with a damping ratio approximately 5 times greater than the control sample.

Table 4.4: Damping properties for a 20 PPI aluminum foam saturated with various fluids.

Fluid	Dynamic Viscosity (Pa s)	Damping Ratio (non.dim)	Frequency (Hz)
Air	1.98×10^{-5}	0.0068	343.2
Motor oil	8.00×10^{-2}	0.0237	343.1
Petroleum Jelly	6.40×10^{1}	0.0352	394.1
Glycerol	1.00	0.0137	346.4
Water	8.90×10^{-4}	0.0101	340.3

Figure 4·24 shows the non dimensional damping ratio plotted versus the dynamic viscosity of the saturating fluid for all of the experiments (dynamic viscosities of the fluids are plotted on a logarthmic scale because the values span nearly 6 orders of magnitude).

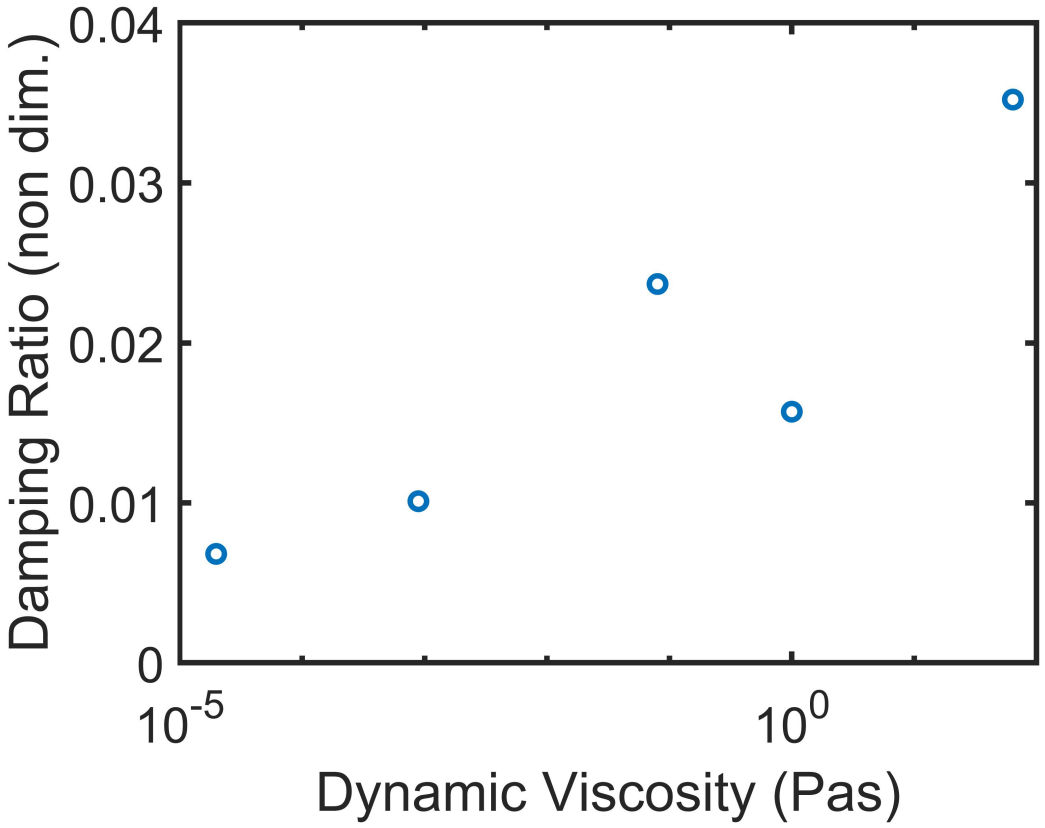

Figure 4·23: Damping ratio versus dynamic viscosity for five different saturating materials.

The calculations of damping ratio implicitly assume a lumped parameter model of the experiment in which the saturated foam is modeled as a spring in parallel with a dashpot between two rigid masses. An analytic model of this system gives the transmissibility T as

$$T = \left| \frac{\omega_n^2 + i2\zeta\omega\omega_n}{\omega_n^2 + i2\zeta\omega\omega_n - \omega^2} \right| \tag{4.12}$$

This model was fit to the experimentally measured transmissibility for petroleum jelly. The fit was performed by estimating ω_n and ζ in the model and computing the root-mean-square error between the measured transmissibility and the model in (4.12). The values of ω_n and ζ were automatically varied by a simplex search algorithm

to minimize the error. The resulting modal properties are listed in the captions of Figures 4·28 and 4·29.

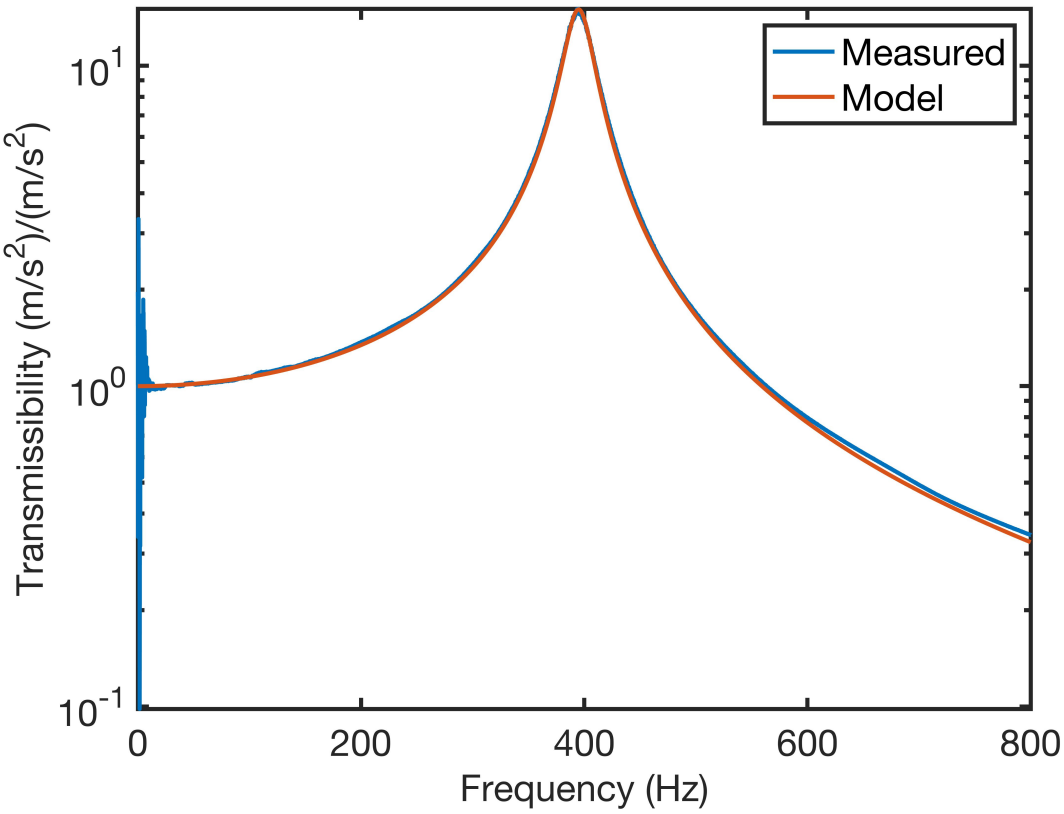

Figure 4·24: Comparison between experimentally measured transmissibility for metallic foam saturated with petroleum jelly and an analytical model given in (4.12). Parameters in the model are $f_n = 395\,\text{Hz}$ and $\zeta = 0.033$.

4.2.3 Transient Vibration

Transient vibration occurs when a structure is subject to an initial condition which causes some time dependent response prior to reaching a steady state. The initial condition may be a force, displacement, or velocity that is applied somewhere on the structure.

Experimental Setup

The experiments described in this section were designed to enable measurement of transient vibration through saturated metallic foams subject to an impact force. The same metallic foam specimens with bonded aluminum discs (described in section 4.2.2) were used again. For this test, first a 0.9 kg mass was attached to each end of the control sample (air saturated metallic foam). The assembly was then suspended by two elastic supports. This was meant to test the assembly in a configuration with free-free boundary conditions for longitudinal vibration. A single accelerometer was placed dead center on one of the masses. The other mass was struck dead center by an instrumented impact hammer (Brüel & Kjær type 8206-002).The test setup is shown in Figure 4·25.

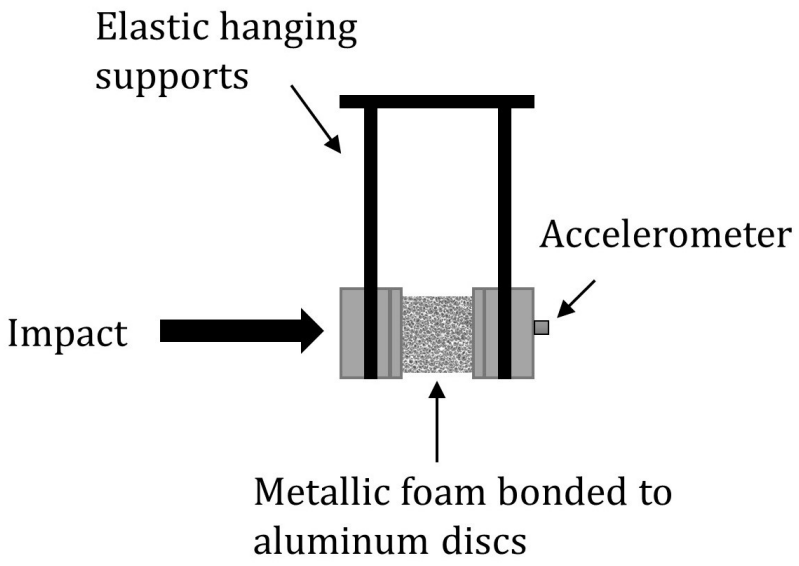

Figure 4·25: Schematic of experimental setup for transient impact experiments. The metallic foam is mass loaded and suspended by elastic supports. The foam is struck at one end by a hammer and the acceleration is measured at the opposite end.

In addition to the control test, the metallic foam was saturated with petroleum jelly as described in section 4.2.2. Since the petroleum jelly is a semi-solid, it was self contained within the foam and did not require an additional housing to support the saturating material. The metallic foam saturated with petroleum jelly is shown in Figure 4·26.

In the next section the measured acceleration versus time data is presented for both the control sample and the sample saturated with petroleum jelly.

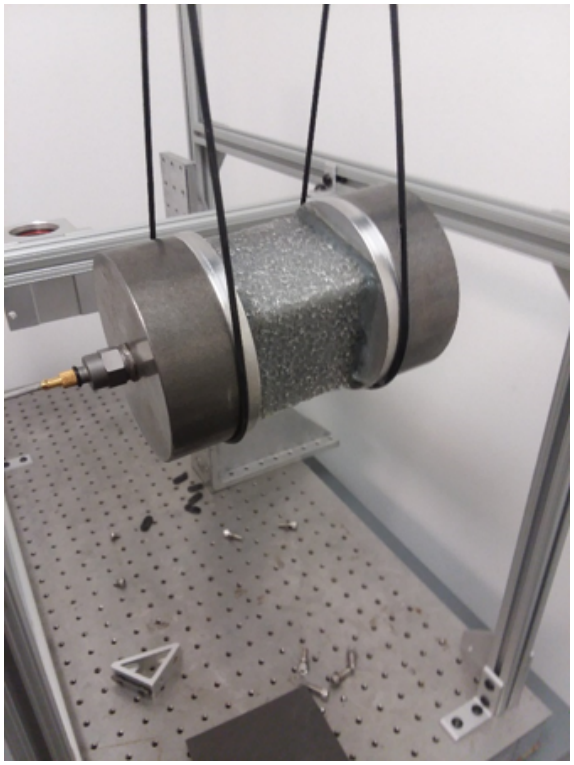

Figure 4·26: A 40 PPI, 92% porosity aluminum foam saturated with petroleum jelly that is mass loaded at each end and suspended by elastic supports.

Experimental and Analytical Results

The results for the impact experiments are shown in Figure 4·27. The acceleration versus time plots indicate that the assembly is ringing down in a single mode. In terms of lumped elements, the assembly can be thought of as two masses that are connected with a spring and dashpot. It can be seen that the petroleum jelly greatly reduces the number of cycles and therefore the amount of time to reach resting position (steady state).

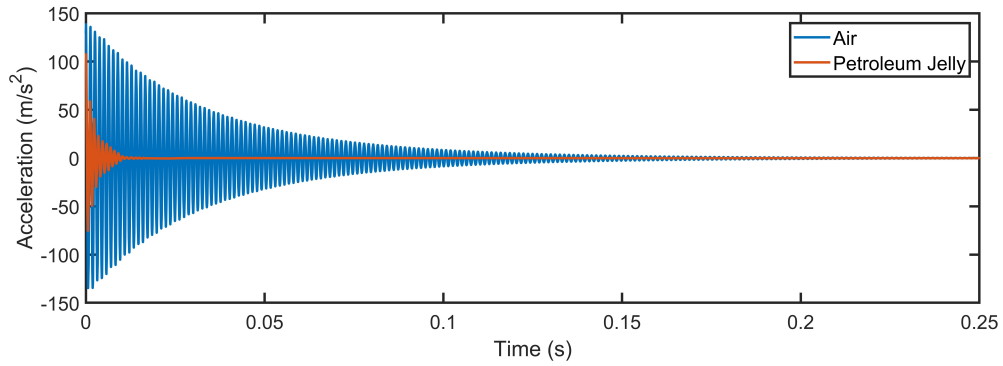

(a)

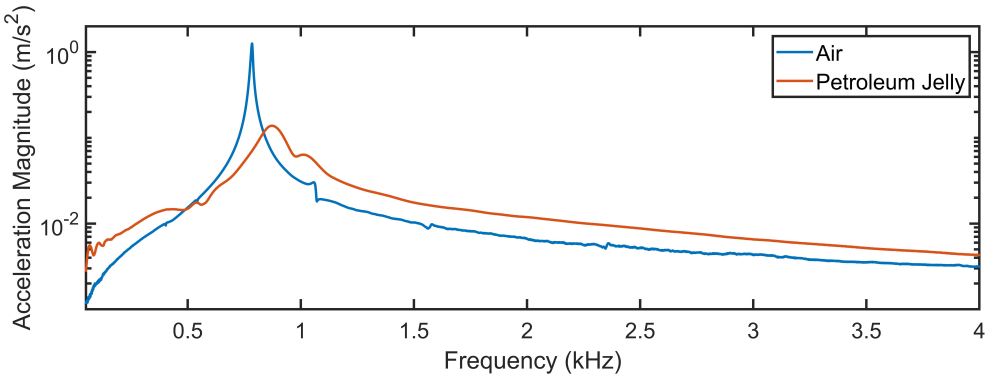

(b)

Figure 4·27: (a) Comparison of transient ring-downs for a 40 PPI, 92% porosity aluminum metallic foam, saturated first by air, and secondly by petroleum jelly. The decay time to nearly zero acceleration is reduced from approximately 0.18 seconds to 0.015 seconds by saturating the foam with petroleum jelly. (b) Fast Fourier Transform of the ring-downs in the top plot.

For each experiment, a modal fit was performed to determine modal properties. The modal fit had the form

$$a(t) = [A\cos(\omega_d t) + B\sin(\omega_d t)]\exp(-\zeta\omega_n t), \tag{4.13}$$

where the undamped and damped frequencies are related by

$$\omega_d = \omega_n\sqrt{1-\zeta^2} \tag{4.14}$$

The fit was performed by estimating ω_n and ζ and performing a least-squares fit to data to determine A and B. Next, a root-mean-square error was computed between the modal fit and the data. The values of ω_n and ζ were automatically varied by a simplex search algorithm to minimize the error. The resulting modal properties are listed in the captions of Figures 4·28 and 4·29.

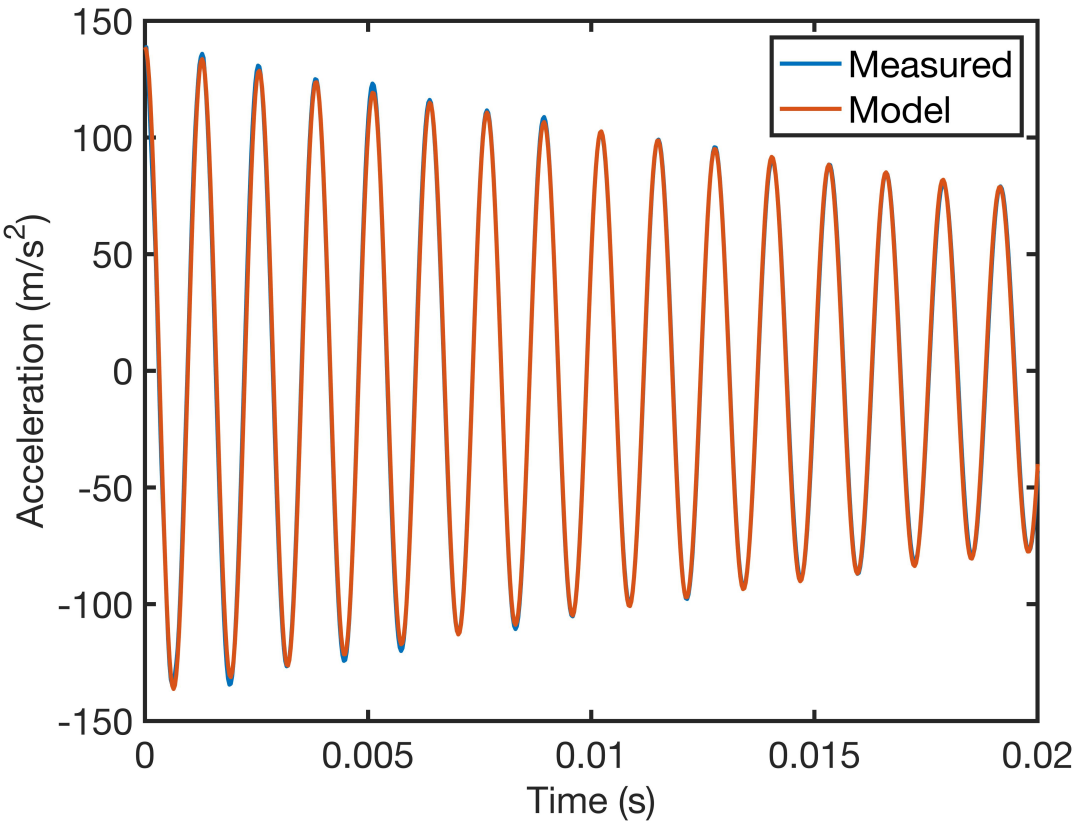

Figure 4·28: Transient ring-down for a 40 PPI, 92% porosity aluminum metallic foam saturated by air. Parameters in the model are $f_n = 783\,\text{Hz}$, $\zeta = 0.006$, and $a_{max} = 139\,\text{m/s}^2$.

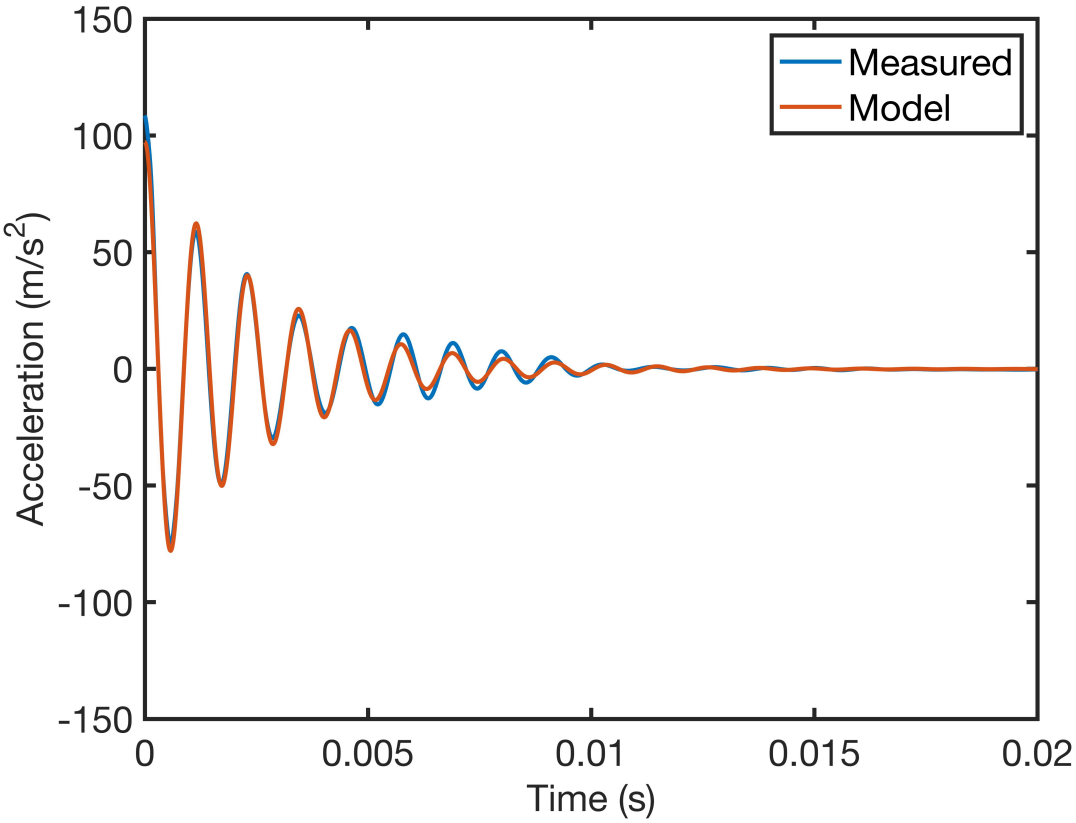

Figure 4·29: Transient ring-down for a 40 PPI, 92% porosity aluminum metallic foam saturated by petroleum jelly. Parameters in the model are $f_n = 874\,\text{Hz}$, $\zeta = 0.070$, and $a_{max} = 108\,\text{m/s}^2$.

For the petroleum jelly saturated foam in Figure 4·29, it can be seen that the damping ratio is over an order of magnitude greater than the control sample. Also the natural frequency is higher for the petroleum saturated foam, consistent with the same trend observed in section 4.2.2. Because of the different mass loading in this experiment compared to the shaker experiment, the natural frequencies were different and the damping ratios, although both higher than the control samples, were also different. These results suggest that the petroleum jelly filled metallic foam has a frequency dependent damping ratio.

The model described above is now used to estimate the natural frequency of 783 Hz

that was observed in Figure 4·28 for the aluminum foam saturated by air. The mode shape associated with the fundamental frequency is symmetric about the midpoint of the foam. The fundamental frequency is thus approximated by

$$f_n \approx \frac{1}{2\pi}\sqrt{\frac{k}{m}} \tag{4.15}$$

where the stiffness of the foam is approximately [83]

$$k \approx \frac{EA}{L}, \tag{4.16}$$

and where L is half the length of the foam due to symmetry, the measured mass is $m = 0.9\,\text{kg}$, and E denotes the elastic modulus.

As discussed in Chapter 2, there is a large range of measured elastic moduli for foams of the similar relative densities. Using a value of $E = 200\,\text{MPa}$, near the lower end of the range, gives a natural frequency of $f_n = 802\,\text{Hz}$, which yields a 2.4% difference between the estimated and measured natural frequencies.

4.2.4 Conclusion

In this section, vibration damping and isolation were investigated experimentally for fluid saturated metallic foams. Five fluids were tested on a shaker setup to measure steady state vibration trasmissibility. For four of the fluids, an increase in damping ratio was seen with increasing dynamic viscosity. A metallic foam was also saturated with petroleum jelly and tested for transient response to an impact. For this material, the damping was shown to increase by an order of magnitude compared to the conventional foam. Damping ratios were found to be frequency dependent and further experimental work would be needed to characterize the optimal frequency range, similar to as discussed in [13].

Chapter 5

Estimating Acoustic Absorption in Foams Using Finite Element Analysis and Boundary Layer Theory

5.1 Approximations for Acoustic Absorption in Foams using an Infinite Planar Model

In this chapter, a method for estimating acoustic absorption in foams is presented using a combination of micro-computed tomography, finite element analysis, and boundary layer loss theory. In the method, the foam is assumed to be rigid framed and the viscous and thermal boundary layers at the fluid and frame interface are assumed to be small compared to foam dimensions. The boundary layer losses are approximated using an infinite planar model. The method is demonstrated for a commercially available open-cell metallic foam and allows for absorption to be estimated without determination of any intermediate variables that are required in existing methods. Enhancement of sound absorbing properties by selection of foam properties, such as porosity and pores per inch, is discussed. Furthermore, predicted absorption trends agree with other published models and experimental data. A simplified, two-dimensional geometry is presented in which the assumptions of this method are analyzed.

5.1.1 Introduction

Metallic foams are composites that consist of a complex porous metal microstructure saturated by a fluid. A number of manufacturers of metallic foam exists, however there is limited technical information available regarding vibration or acoustic properties from these manufacturers. This section proposes a method to characterize acoustic properties in porous materials. The method consists of four steps. The first step is creating a high-fidelity representation of the foam geometry using micro-computed tomography (micro-CT). The second step is the construction of a finite element model whose mesh includes the saturating fluid. The third step is an acoustic analysis using the finite element method. The fourth step is an estimate of dissipation using existing boundary layer theory [84], [85]. Using this method, acoustic absorption trends are predicted and modeled for a commercially available metallic foam. The sound absorption as a function of common foam specifications such as relative density and pores per inch (PPI) is discussed.

This method is demonstrated by considering a normally incident pressure excitation on a layer of metallic foam. The metallic foam is not a periodic structure. However, there are approximate finite element methods [86] which enable use of periodic boundary conditions with mismatching geometries. Therefore the proposed method could be utilized with more general excitations such as oblique incidence.

The complex microstructure of metallic foams makes them difficult to analyze numerically; however, techniques have been developed to mesh and model exact microstructures. Using a combination of micro-CT scanning, image processing, and meshing software, complete three-dimensional meshes can be created from physical samples and imported into finite element analysis (FEA) software to study microstructural phenomena. The advantages of this method are the ability to capture the true microstructure of the material and to visualize the solution field of interest. This

technique has been used in the literature, for example, to examine elastic and plastic behavior of an open-cell metallic foam subject to tension [87] and a closed-cell metallic foam in compression [88]. Micro-CT scans have also been used for studying foam statistics and constructing representative unit cells [89].

Experimental measurements have been used to characterize sound absorption in both open-cell and closed-cell foams. In general, open-cell foams have superior sound absorption because they allow propagation of the acoustic wave further into the material, whereas much of the energy is purely reflected for closed-cell foams. Lu et al. [21] improved sound absorption in a closed-cell aluminum foam by modifying the foam through rolling and hole drilling processes. Han et al. [22] looked at effects of pore size, sample thickness, and inclusion of an air-gap backing for an open-cell aluminum foam fabricated through a high-pressure infiltration process. They found that smaller pore sizes had the best absorption when there was no gap, while inclusion of an air gap increased absorption because it changed the resonant conditions.

Additionally, Ke et al. [90] fabricated an open-cell foam which had a graded microstructure. This gradual decrease in pore size across the thickness of the sample led to superior absorption compared to a foam with larger uniform pore size fabricated by the same method. Experimental difficulties can, however, arise from limited test frequency range due to impedance tube constraints, limited sample size, difficulty machining metallic foam samples to exact dimensions, and definition of the front (leading) surface for porous materials in an impedance tube [47].

To overcome these difficulties and to provide further insight on absorption mechanisms, many modeling efforts have been proposed. Most modeling efforts for metallic foams have relied on the assumption that the foam skeleton acts as a rigid frame, and there is one acoustic wave that propagates through the fluid surrounding the foam [21]. In this way, the foam and surrounding fluid can be treated as an effec-

tive fluid medium, [20] in which two frequency dependent complex parameters are necessary to characterize the foam absorption.

One of the most prevalent models is the Johnson-Champoux-Allard (JCA) model [44], [45], which uses five independent properties of the foam (porosity, permeability, tortuosity, thermal characteristic length, viscous characteristic length) to characterize the viscous and thermal acoustic losses. This model was extended by Lafarge [48] to include an additional term, the static thermal permeability (JCAL model), and by Pride [49] to include two additional tortuosity terms (JACPL model). Use of these models requires either direct measurement or computational modeling to determine the five to eight material parameters that describe the foam. These models have also been used to propose absorbing layer designs, for example closed-cell metallic foams with perforations [91] and lattice type fibrous materials [2]. Furthermore, Wang et al. [92] proposed a point-matching method for optimizing acoustic properties for some cellular solids, but was limited to 2D structures. Lu et al. [93] developed an analytical model for idealized foams made through a negative-pressure infiltration process; however, they were limited in looking at foams of void fractions up to 0.7 while many metallic foams are made from different processes, have different microstructure, and can have void fractions up to 0.97.

In the next section, the materials and method used to estimate absorption are described. The advantage of the method is the ability to create high fidelity finite element models of metallic foam from micro-CT scans and use those models to estimate sound absorption without the determination of any intermediate variables. Section 5.1.3 presents results of the method with comparisons to published theory and experimental data. By using the method, effects of viscous and thermal losses can be analyzed independently. Finally, section 5.1.4 presents a study on the accuracy of the method on a two-dimensional geometry designed to represent a foam pore.

5.1.2 Numerical Analysis

Materials and methods

Aluminum foam samples with approximately 9 percent nominal relative density and 40 pores per inch were obtained from ERG Aerospace Corp. (Duocel) for this study. Samples were cut smaller than 1 cubic inch and imaged (Figure 5·1) with a Scanco micro-computed tomography scanner at Boston University.

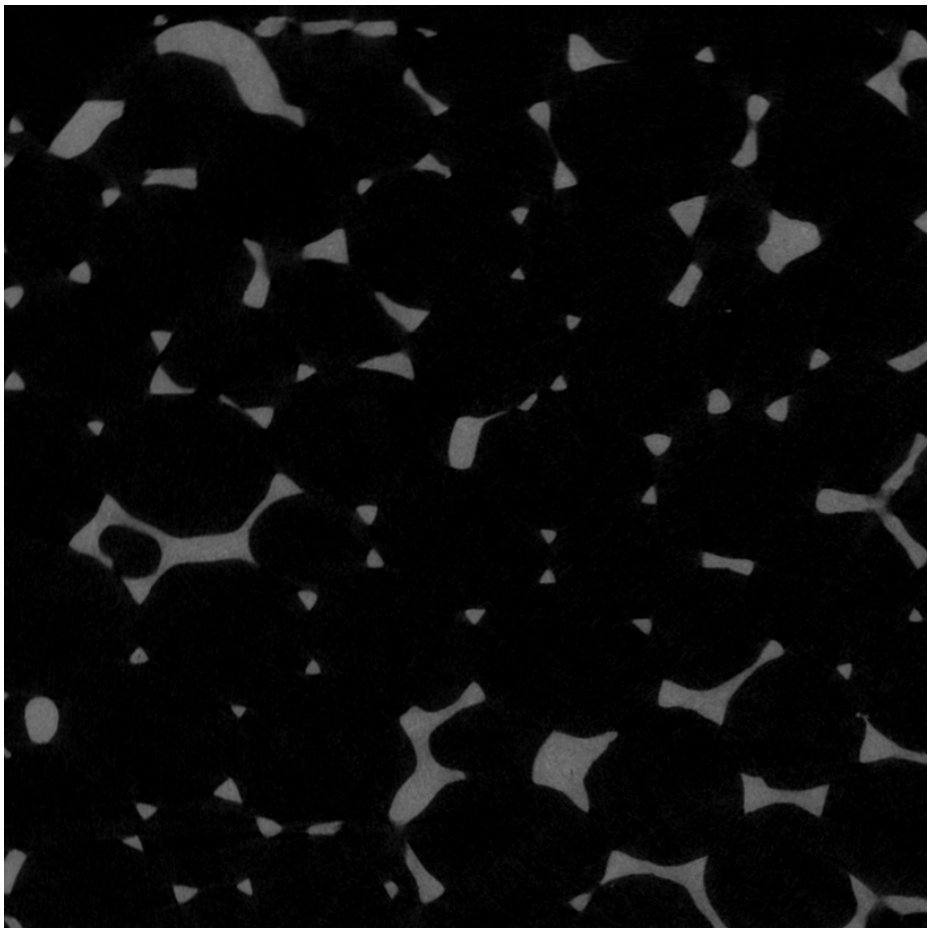

Figure 5·1: Single image from a micro-CT scan showing cross sectional view of a Duocel 40 PPI aluminum foam. Light region is the aluminum and dark region is the air.

The commercial software Simpleware ScanIP was utilized to create FEA meshes, utilizing image thresholding and smoothing filter algorithms available with this soft-

ware. Meshes of both the foam and void space surrounding the foam were created, as shown in Figure 5·2. For the acoustic analysis presented here, the rigid frame assumption is employed due to the high stiffness of metallic foam relative to air, [92] thus only the air in the void region is used in the analysis.

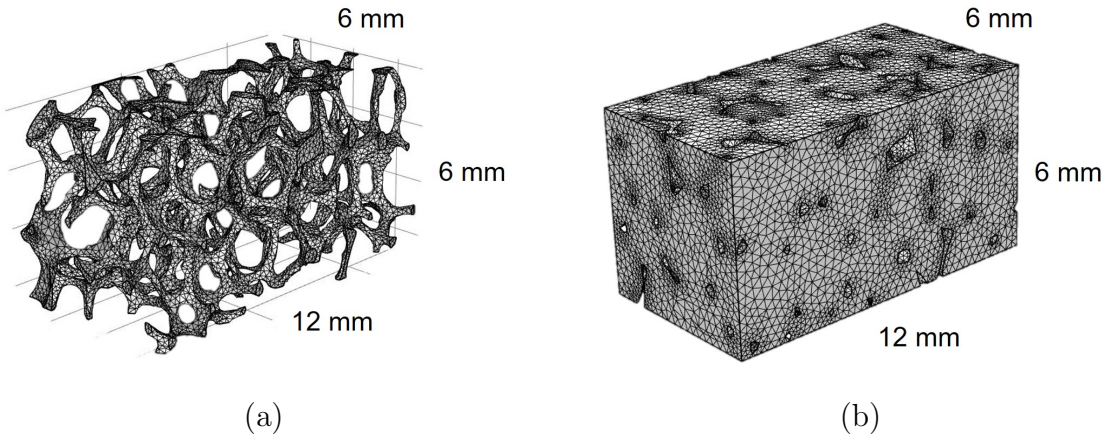

Figure 5·2: Meshes constructed from micro-CT scans for (a) the metal foam and (b) the void space.

Acoustic finite element analysis

In this section, the normal incidence absorption coefficient is considered in air. A metallic foam layer 6 mm by 6 mm in cross section and 48 mm in thickness was constructed from the mesh in Figure 5·2 (b) for later comparison to published data. The Helmholtz equation is solved in the void region of the foam, applying a specified pressure amplitude at one end of the layer and rigid boundary condition at the other end. The lateral faces of the layer had zero-normal-velocity imposed. The mesh is resolved such that there are at least 10 nodes per acoustic wavelength at the highest frequency, 6 kHz in this study. The commercial software COMSOL Multiphysics was used. The solution fields are shown in Figure 5·3 for 6 kHz. In this analysis, the applied pressure amplitude was real, the sample was rigidly backed, and there was

no intrinsic material damping in the finite element model. Therefore, the velocity everywhere is out of phase with the pressure. As a result, the complex pressure field is purely real and the complex velocity field is purely imaginary. At 6 kHz, the acoustic wavelength in air is 5.7 cm. This is greater than the sample thickness of 48 mm and much greater than the pore diameter of approximately 1 mm, thus the acoustic field is not strongly affected by the foam microstructure. However, there is a three-dimensional velocity field at the fluid and frame interface from which both an accurate tangential velocity profile and corresponding surface area of the mesh are needed from the finite element solution.

Note that damping in the air is ignored in this step. The calculation of losses is discussed in the next section below. One could consider utilizing a complete numerical thermoviscous acoustic solver for this case, solving a form of the linearized Navier-Stokes equations in the frequency domain. However, this method is computationally intensive because the mesh must resolve spatial variations in the boundary layer, which decreases with an increase in frequency. For example, at 0.5 kHz the viscous boundary layer is 98 microns, and at 5 kHz it is 31 microns in air. Thus for a complex microstructure with dimensions on the order of 50 mm, a complete thermoviscous solution is computationally infeasible. In the next section, an alternative, computationally efficient method is presented which leverages boundary layer theory for the case of small boundary layer to estimate acoustic losses.

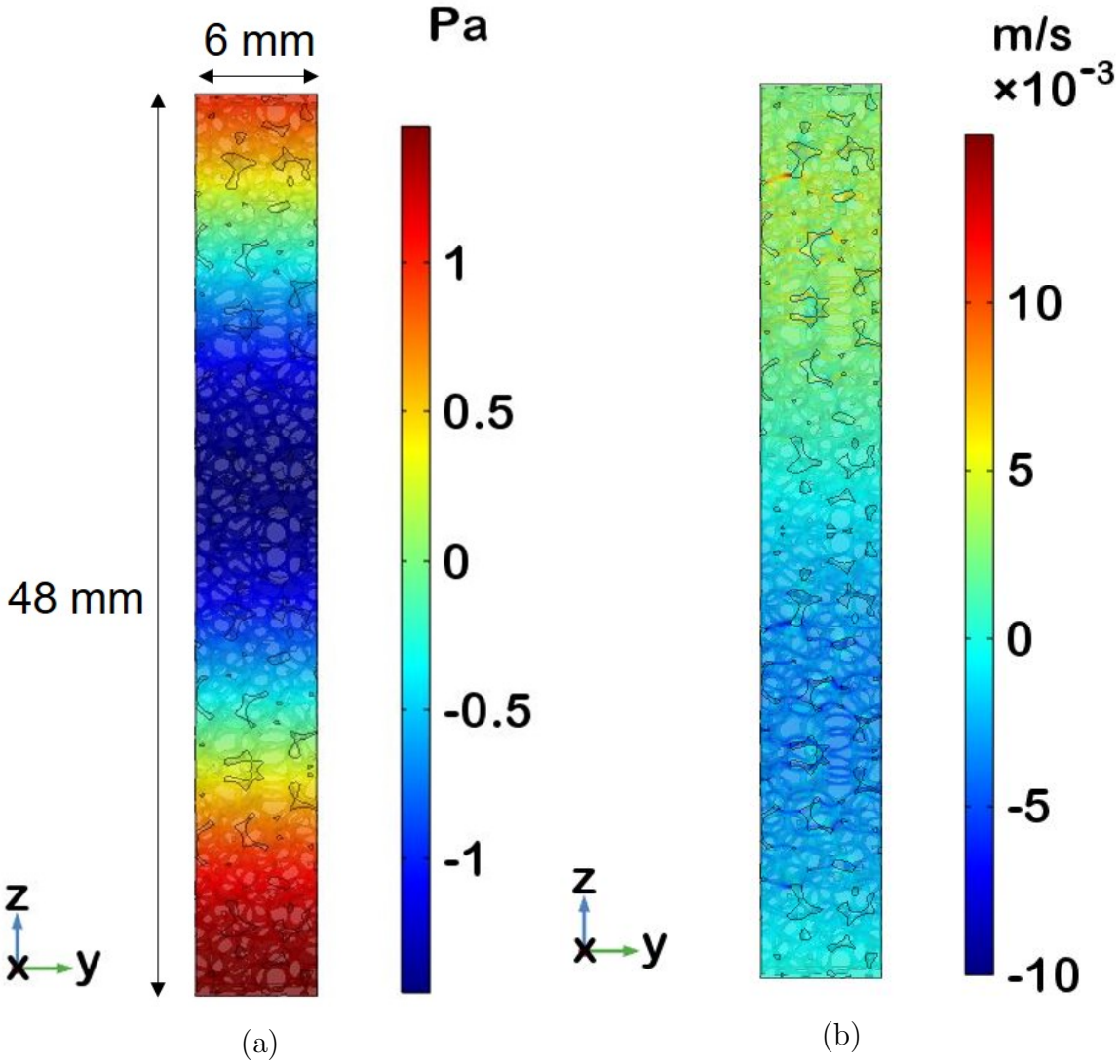

Figure 5·3: Semi-transparent view of solution field at 6 kHz for (a) real component of pressure and (b) imaginary component of velocity. The applied pressure is at the top of the figure.

Thermal and viscous losses

The estimation of absorption from thermal and viscous losses is carried out in the regime where the boundary layer is small compared to geometry. This method has been predominantly used for resonators and cavities with relatively simple ge-

ometries [84], [85], [94]. To the authors' knowledge, this method has been partially discounted [94] and not been previously used elsewhere for estimating absorption in porous materials. This is likely due to either difficulty modeling the exact microstructure or the porous absorbers themselves having geometry at similar length scales to the boundary layer. Indeed for some foams, the latter can be true over a large frequency range. However many foams (including metallic foams) can have pores sizes on the mm scale and boundary layers on the order of 15-100 microns between .5-20 kHz. This means the foam dimensions are 1-2 orders of magnitude larger than the boundary layers, which warrants investigation of using the boundary layer loss theory for porous materials.

The analysis begins by considering a fluid oscillating over a rigid flat wall. Following previous derivations, [95], [84] the solution for the tangential or shearing velocity profile is

$$u(y,t) = u_t[e^{-y/\delta_v}\cos(\omega t - \frac{y}{\delta_v}) - \cos(\omega t)], \tag{5.1}$$

where δ_v is the viscous boundary layer thickness

$$\delta_v = \sqrt{2\nu/\omega}, \tag{5.2}$$

and the tangential velocity u is a function of height y above the wall and time t. The velocity u_t is the fully developed tangential velocity amplitude just outside the boundary layer, ν is the kinematic viscosity, and ω is the angular frequency. The shear stress at the wall is

$$\tau = \mu\frac{du}{dy} = \rho\nu\frac{u_t}{\delta_v}(\sin(\omega t) - \cos(\omega t)), \tag{5.3}$$

where ρ is the density and μ is the dynamic viscosity. Approximating the boundary layer as small, one can write an expression for the dissipated power per unit area,

averaged over one acoustic period as [84]

$$\langle \frac{dE_s}{dt} \rangle_v = \frac{1}{2} \rho u_t^2 \sqrt{\frac{\omega \nu}{2}}. \tag{5.4}$$

From Equation 5.4, it is clear that the viscous power dissipated per unit area is a function of the velocity just outside of the boundary layer, u_t, thereby allowing velocity fields computed from an undamped acoustic analysis to be used as an approximation in the limit of small boundary layer.

The analysis for thermal losses is similar to that of viscous losses. Temperature fluctuations give rise to pressure fluctuations, and using an ideal gas relationship, the resulting thermal power dissipated per unit area can be written as [84]

$$\langle \frac{dE_s}{dt} \rangle_{th} = \frac{1}{2} (\gamma - 1) \frac{p^2}{\rho c^2} \sqrt{\frac{\omega D}{2}}, \tag{5.5}$$

where γ is the specific heat ratio, p is the pressure right outside the boundary layer, c is the sound speed, and D is the thermal diffusivity. The thermal boundary is

$$\delta_t = \sqrt{2D/\omega}. \tag{5.6}$$

To calculate the total power absorbed, Equations 5.4 and 5.5 are integrated over the appropriate surface area. For a metallic foam, this is the outer surface area of the foam. For viscous losses, only the tangential component of velocity across a surface contributes to losses, and this must be tracked in the integration. By definition, the absorption coefficient is the ratio of absorbed power to incident power, and can be estimated from the acoustic analysis and implementation of boundary layer loss theory:

$$\alpha = \frac{\int_S \langle \frac{dE_s}{dt} \rangle_v + \langle \frac{dE_s}{dt} \rangle_{th} \, dS}{P_{in}}, \tag{5.7}$$

where P_{in} is computed from the acoustic analysis boundary condition of applied

pressure. All properties used for air in the simulation and loss calculations are listed in Table 5.1.

Table 5.1: Air properties used in simulations and loss calculations.

Variable	Value	Unit
ρ	1.2	kg/m^3
c	343	m/s
D	2.170×10^{-5}	m^2/s
ν	1.515×10^{-5}	m^2/s
γ	1.4	-

5.1.3 Results and discussion

Absorption results and model verification

The absorption coefficient versus frequency for the aluminum metallic foam is shown Figure 5·4. An important capability of this approximate analysis is the ability to independently analyze the viscous and thermal losses. It can be seen that viscous effects dominate. In general, the directionality of the foam microstructure would affect the thermal losses. However, for air at the frequencies studied in this section, the thermal boundary layer is so small (e.g. approximately 80 microns at 1 kHz) that the thermal losses are not highly due to local effects, but are dominated by changes in the overall pressure field (through ideal gas relationships). Also, there appears to be an onset of two peaks (at 2.4 and 5.8 kHz); these are related to damped resonances of the layer. Specifically, consider a tube of air closed at one end and open at the other, with a thickness of 48 mm. If damping is neglected, the standing modes can be computed from $f_n = \frac{nc}{4L}$, where n is an odd integer (1,3,...), c is the sound speed, and L is the length. The first two modes are $f_1 = 1.79\,\text{kHz}$ and $f_2 = 5.36\,\text{kHz}$. Although it is not expected that the undamped modes match the absorption modes exactly, it can be seen that the periodicity of the absorption peaks can be attributed to sample

length due to a very similar change in frequency between the first two modes for both cases.

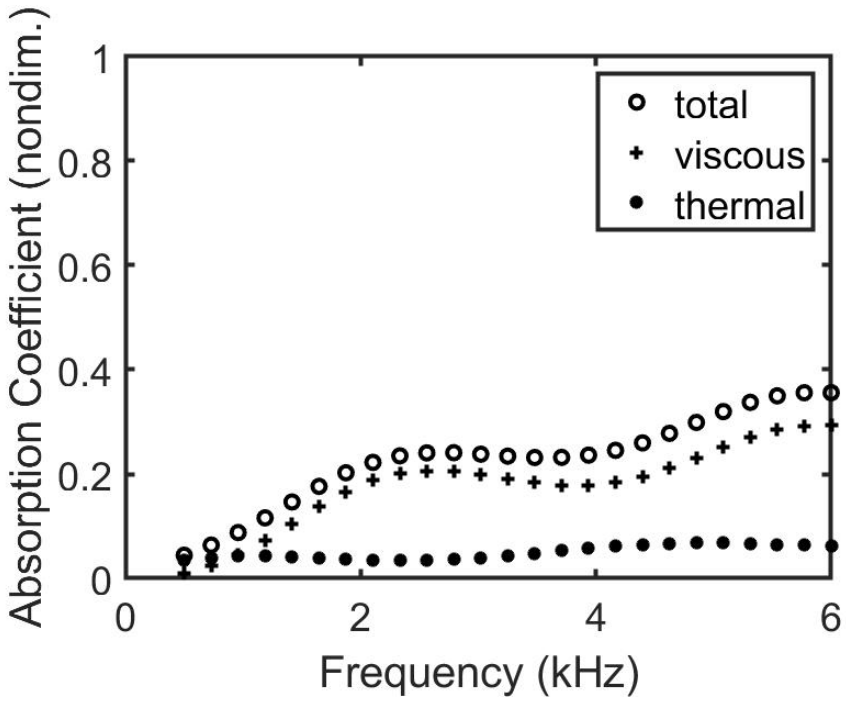

Figure 5·4: Viscous, thermal, and total acoustic absorption of 40 PPI Duocel aluminum foam of thickness 48 mm computed from the approximate method.

For validation, the proposed method was compared to published experimental data [1] and implementation of the JCAPL model, [1] shown in Figure 5·5. There is good agreement between all three except at low frequencies, in which the experimental data shows a resonant spike which is likely an experimental artifact.

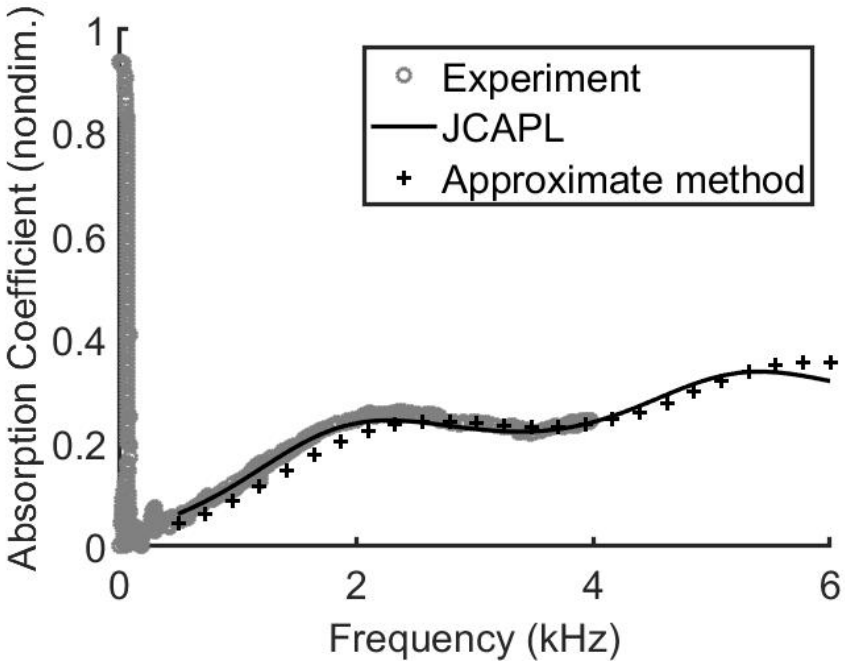

Figure 5·5: Comparison of acoustic absorption with published JCAPL model [1] and test data [1].

Effects of porosity and PPI

Metallic foams, such as those manufactured by ERG, can be fabricated with varying relative densities and PPI while retaining similar geometrical structure. Since viscous and thermal losses are integrated over the surface area of the foam, it follows that foams with a larger surface area will be better absorbers, as long as the assumption of small boundary layer remains valid. The following analysis is a way to predict how surface area scales with changes in foam parameters.

An ideal unit cell for an open-cell foam, proposed by Gibson and Ashby [5], consists of interconnected square beams with thickness t, and length L. From mass and geometrical relationships, the following can be derived. The volume, relative density,

surface area, and PPI scale, respectively as:

$$V \propto L^3, \tag{5.8}$$

$$\frac{\rho_f}{\rho} \propto \frac{t^2}{L^2}, \tag{5.9}$$

$$SA \propto tL, \text{and} \tag{5.10}$$

$$PPI \propto \frac{1}{L}. \tag{5.11}$$

Thus the specific surface area, defined as the foam surface area divided by the bulk volume, is

$$SSA \propto \frac{1}{L}\sqrt{\frac{\rho_f}{\rho}}. \tag{5.12}$$

It is expected that the specific surface area increases with increasing PPI and increasing square root of relative density. To study this effect, a total of eight meshes of varying relative density for 20 PPI and 40 PPI metallic foams were analyzed. An additional micro-CT scan of a 20 PPI metallic foam was done. To create models with varying relative density, image thresholding was controlled in ScanIP in order to retain the same PPI structure but create a new digital design of a realistic structure that could be fabricated.

The specific surface area versus relative density was calculated from the meshes and plotted in Figure 5·6; the trends predicted from Equation 5.12 are apparent.

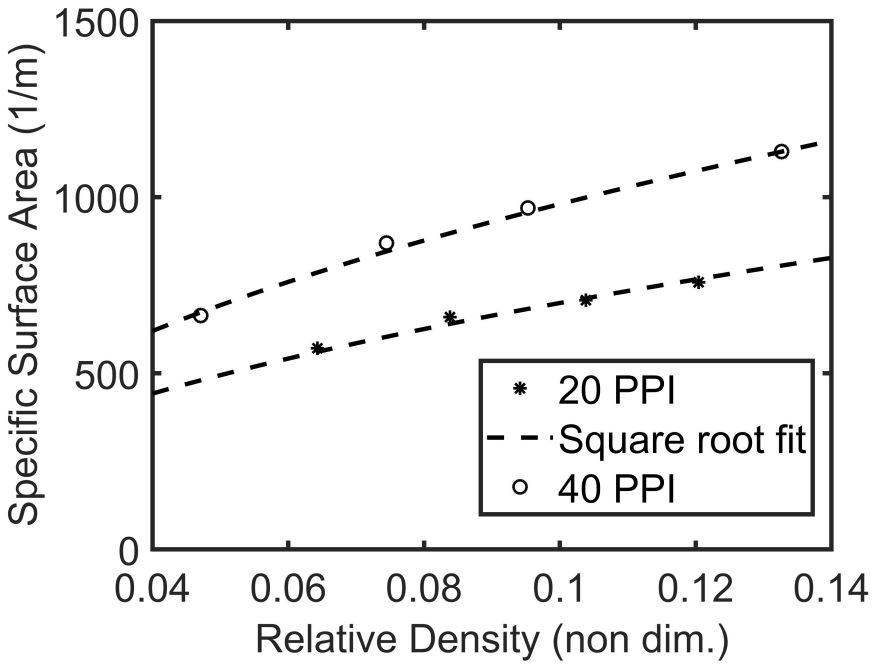

Figure 5·6: Specific surface area versus relative density for eight different meshes created through image thresholding in ScanIP.

The analysis described in Section 5.1.2 was utilized for all meshes and the absorption is plotted in Figure 5·7. The trends indicate that the optimum absorption is achieved for larger PPI (smaller pore sizes) and higher relative density.

Results have been reported in the literature for similar pore sizes [22], [90], [93] although the type of metallic foam, fabrication method, and fluid medium can all effect this trend.

This is more apparent considering relative density; continuing to increase relative density (and decrease void fraction) drives the material to becoming less like a foam, and more like a solid metal, thereby increasing reflected energy and reducing sound absorption performance. Typically this would be for higher relative densities (20 to 25 percent [96]), that are above the values studied in this section and even above fabrications limitations of some manufacturers, including ERG.

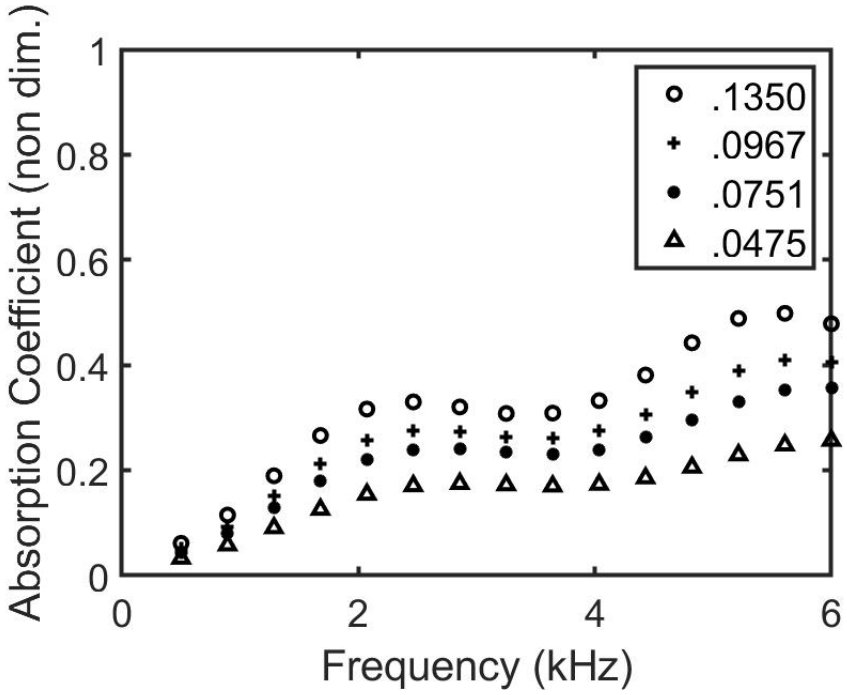

(a)

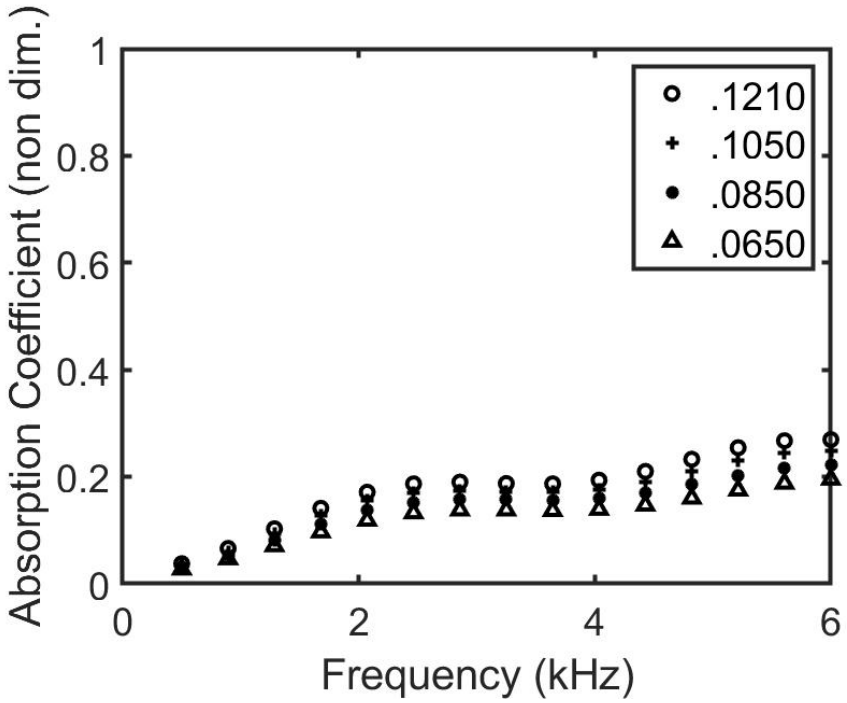

(b)

Figure 5·7: Absorption coefficient versus frequency for varying relative density for (a) 40 PPI and (b) 20 PPI

5.1.4 Regimes of Accuracy

The section presents the accuracy of the approximation compared to a complete thermoviscous acoustic FEA solution using a two-dimensional geometry designed to be representative of a pore. The accuracy of the approximation depends on the length scales of the foam compared to the thermal and viscous boundary layers of the surrounding fluid. In particular, there are a few lengths that should be considered. The approximation cannot accurately predict interactions of overlapping boundary layers; therefore the radius of a pore should be much greater than the boundary layer thickness. The approximation is also derived based on a velocity and pressure profile over an infinite flat plate. In a foam, there are curved and finite surfaces in which the velocity profile will differ from the velocity profile derived for the infinite flat plate. For example, as shown in Figure 5·8, the tangential velocity profile is uniform over an infinite plate, which is not true in general for other surfaces. However, there are regimes in which the boundary layers become so insignificant such that assuming an infinite flat plate velocity profile leads to a very accurate estimate for absorption, despite the geometry difference.

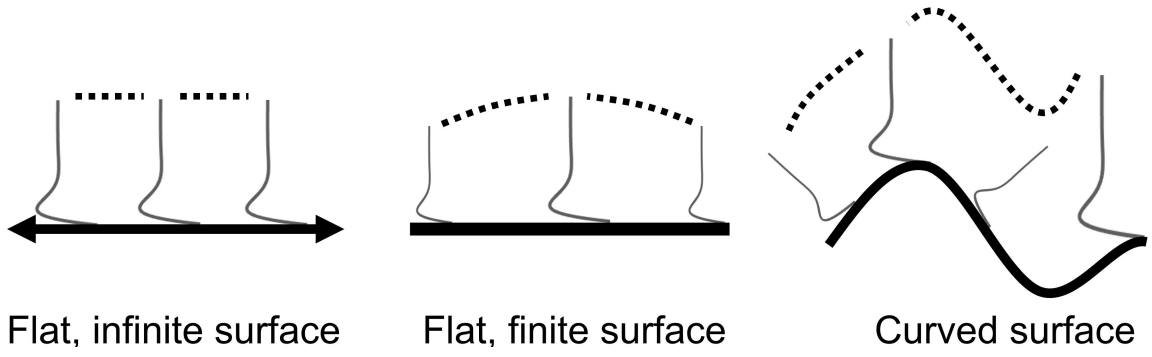

Figure 5·8: Schematic of spatial dependence of tangential velocity boundary layers over different surface geometries.

Consider the velocity boundary layer surrounding a circular cross section having similar dimensions as a metal foam strut, shown in Figure 5·9. In Figure 5·9 (a), the

radius is 1 mm and the frequency is 100 Hz. The velocity boundary layer comparison for the infinite plate and the numerical solution in Figure 5·9 (b) shows quite good agreement. As frequency increases, the boundary layer thickness decreases and the agreement is expected to improve. This observation, which is crucial for the use of the proposed method, also holds true for the thermal boundary layer.

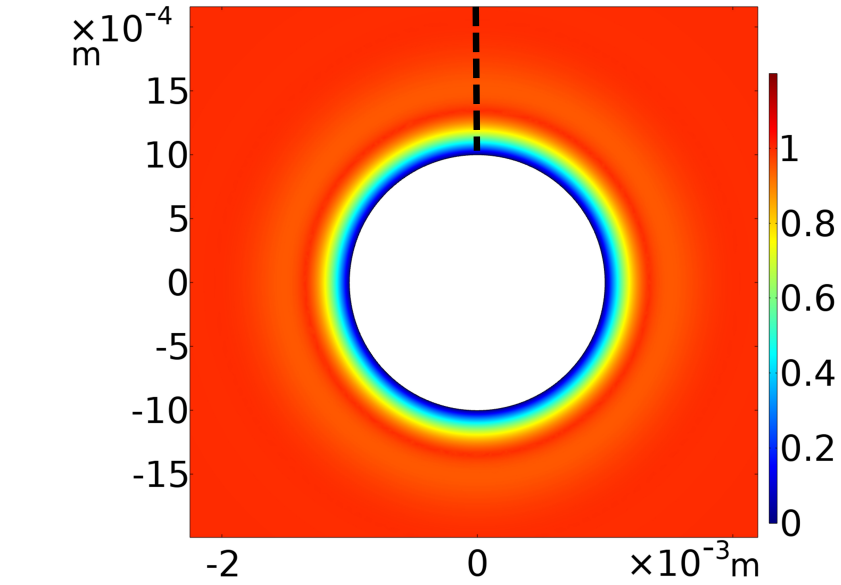

(a)

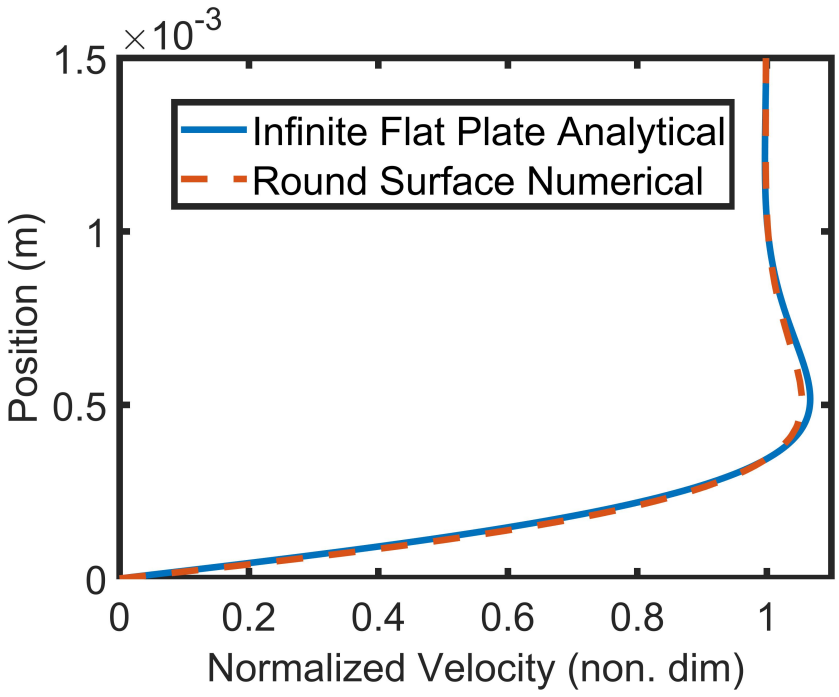

(b)

Figure 5·9: (a) Velocity profile at 100 Hz (normalized to mean field velocity) over a circle of radius equal to 1 mm and (b) comparison to the velocity profile over an infinite flat plate (plotted along dashed line in (a)).

Recall that there is no damping in the FEA solution using the boundary layer loss approximation. To calculate the absorbed power, the fluid damping properties are taken into account later using the pressure and velocity fields found from the undamped FEA solution. Thus the absorbed and incident power are computed semi-independently (the phase of the reflection coefficient is not known by this computation, only the magnitude).

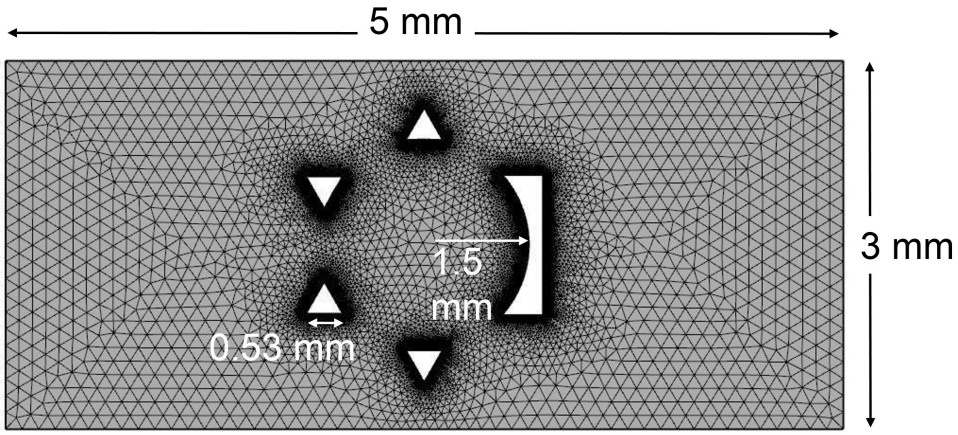

Figure 5·10: Two-dimensional mesh representing the cross section of a single pore.

Consider the geometry in Figure 5·10, which is based on the microstructure from Figure 5·1. There are cross sectional shapes that appear triangular and larger shapes which represent different cross sections of foam struts and nodes. This model is designed to capture the geometry, length scales, and boundary layer effects surrounding a single pore in the foam with a simplified two-dimensional model while not having the computational expense of a complex, three-dimensional unit cell models such as a tetradecahedron. Average measurements of strut thickness (side length of triangular cross section) and pore radius were measured from micro-CT images of a 40 PPI foam. The averages yielded a strut side length of $s = 0.53$ mm and pore radius $r_p = 1.5$ mm.

For this model, the pore has also been assumed motionless. For use of this ap-

proximation with flexible foam, the frame and void region around the frame both need to be included in the mesh and a full structural acoustic FEA solution will need to be computed. The losses in this case can also be due to structural damping due to vibration of the foam.

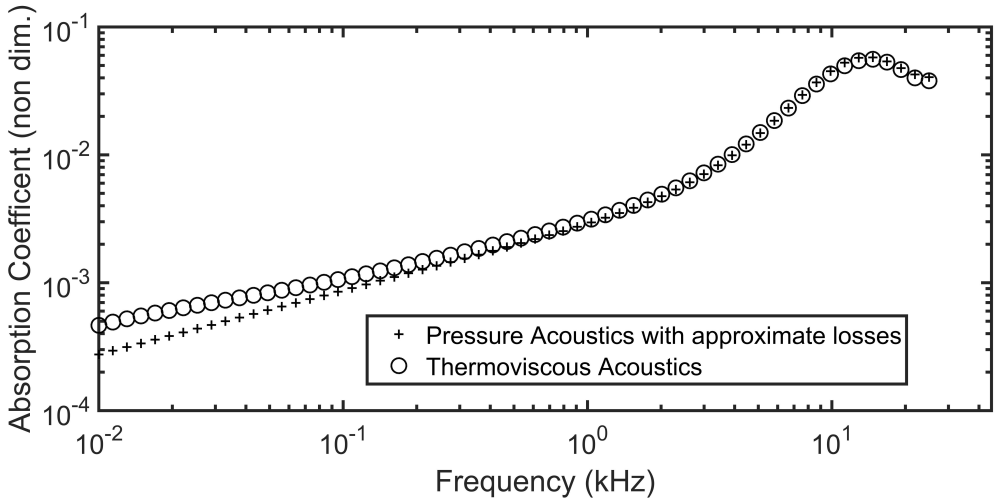

Figure 5·11: Absorption coefficient versus frequency for the single pore cross section model.

This example considers losses that occur only over interior geometry features, not along outer edges. The absorption is computed assuming a rigidly backed layer with an incident pressure source. Computations are made in COMSOL, using both the pressure acoustics module coupled with the boundary layer loss approximation and also the thermoviscous acoustics module. In the thermoviscous computations, the linearized Navier-Stokes equations are solved in the frequency domain, taking into account boundary layer effects in the acoustic analysis as a single step. However, this means the mesh must adequately resolve the boundary layer (typically at least 10 elements over the boundary layer). The fine mesh around the inner surfaces, as shown in Figure 5·10, is the mesh used for the thermoviscous analysis. The boundary layer loss approximation does not require such a fine mesh. Additionally there are less degrees of freedom per node because temperature is not being computed. This

results in significantly less computation time. The results for absorption coefficient versus frequency are shown in Figure 5·11. The computation time was decreased from 28 minutes, 56 seconds to 29 seconds (on a desktop with 16 GB RAM for 60 frequencies) by using the approximation.

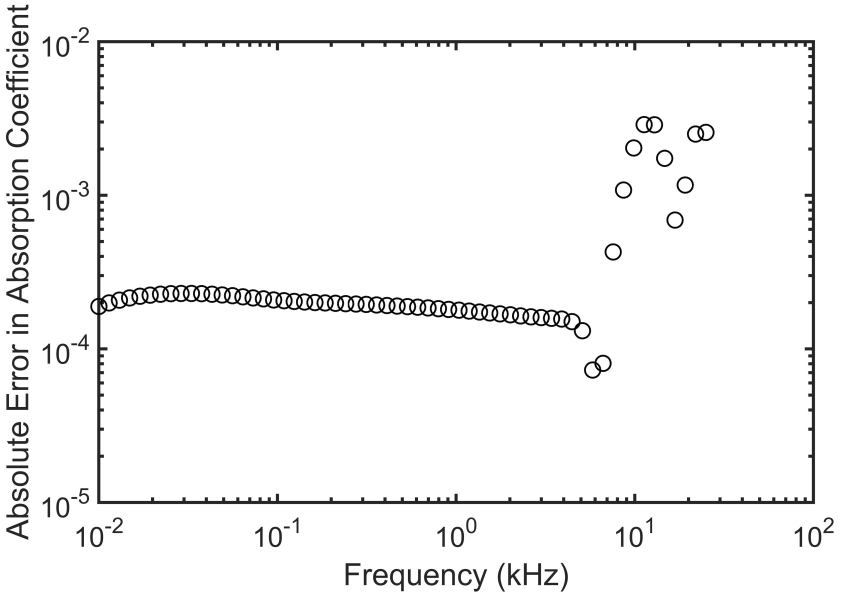

Figure 5·12: Absolute error versus frequency for the single pore cross section model.

The absorption coefficient for the single pore model is relatively low, less than 0.06 over the entire frequency range. The absolute error in absorption coefficient for the approximate and thermoviscous simulation is plotted in Figure 5·12. Over the entire frequency range, the absolute error never exceeds 0.003 which indicates significantly high accuracy considering that the absorption coefficient scales from 0 to 1.

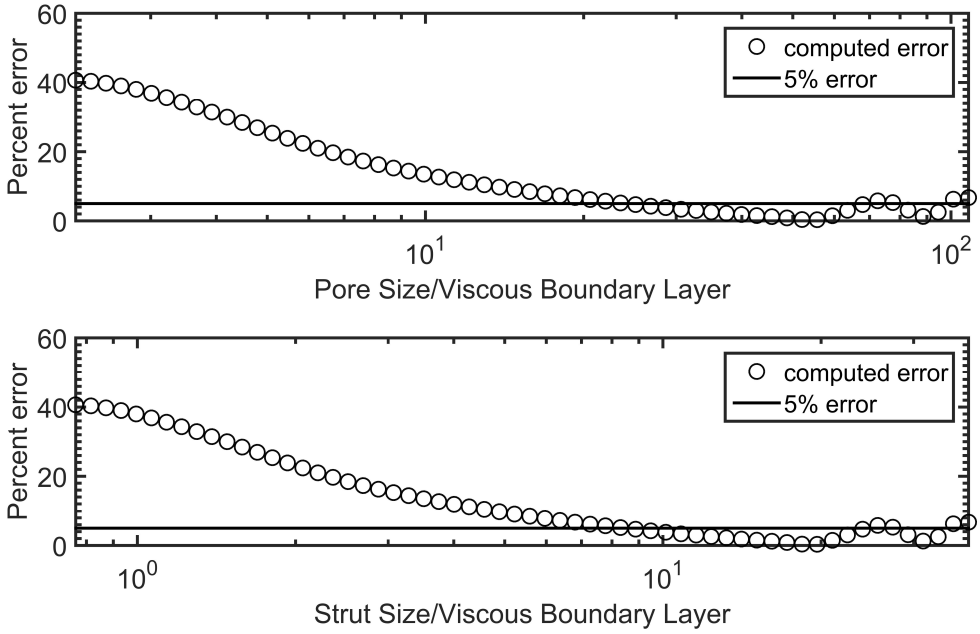

Figure 5·13: Percent error for the single pore cross section model.

To look at regimes in which the approximation is accurate, two non-dimensional parameters can be formed. Both the viscous and thermal boundary layers could be considered. For this case, since both boundary layers are nearly identical in magnitude, only the viscous boundary layer will be used. The non-dimensional numbers are the pore radius divided by the boundary layer ($\Pi_1 = r_p\sqrt{\frac{\omega}{2\nu}}$) and the strut side length divided by the boundary layer ($\Pi_2 = s\sqrt{\frac{\omega}{2\nu}}$). These are similar to the "acoustic" Reynolds number used by others [92]. In Figure 5·13, the percent error between the approximate and thermoviscous simulation is plotted. The percent is calculated as the absolute value of the difference divided by the thermoviscous absorption at each frequency. The plots indicate that the approximation should not be used when the length scales of the foam are less than or equal to the size of the boundary layer (greater than 40 % error is observed). When the pore size and strut size become large, the percent error continues to diminish and as a result of the approximation,

the percent error fluctuates around and below 5%.

5.1.5 Conclusion

The method presented in this section utilized high fidelity models of metallic foam constructed using micro-CT scans to estimate acoustic absorption based on boundary layer theory. The analysis is valid for regimes in which the boundary layer is small compared to foam geometry. The results showed that for low relative density open-cell metallic foams in air, viscous effects dominate over thermal effects from approximately 1.5 to 6 kHz. Decreasing pore size and increasing relative density yielded superior absorption. Finally, a two-dimensional geometry was presented which elucidated accuracy of the method by comparison to a complete thermo-viscous acoustic finite element solution.

5.2 Approximations for Acoustic Absorption using Viscous and Thermal Boundary Layers modeled as Acoustic Boundary Conditions

In this section, a method for estimating acoustic absorption in porous materials is presented in which the thermal and viscous boundary layers are modeled through boundary conditions to the Helmholtz equation for the acoustic pressure. The method is proposed for rigid-framed porous materials, where vibration of the frame is negligible compared to pressure fluctuations in air. The method reduces computation times by two orders of magnitude compared to a full thermoviscous acoustic solver. Furthermore, the method is shown to be highly accurate over geometrical features and frequencies of interest, as long as thermal and viscous boundary layers do not overlap and the effects of sharp changes in curvature are negligible. The method is demonstrated for a periodic sound absorber from the literature as well as a sound absorber with a randomly graded microstructure.

5.2.1 Introduction

In addition to conducting experiments, it is important to be able to predict acoustic absorption of porous materials for design and optimization. In this section, a method for estimating acoustic absorption for rigid-framed porous materials is presented that utilizes a recently derived model [97], in which visco-thermal losses are modeled as a boundary condition of the Helmholtz equation for the acoustic pressure. This method is compared to existing methods, including a thermoviscous model based on the linearized Navier-Stokes equations, a fluid-equivalent homogenization model, and another approximate method utilizing a Helmholtz solver with losses approximated by pressure and velocity profiles over an infinite flat plate [84]. The proposed method is advantageous for porous materials with random or graded microstructures, where homogenization techniques are difficult and complete thermoviscous solutions are computationally expensive.

Additionally, in this work a detailed analysis of a two-dimensional fibrous material is presented. The accuracy of the method is analyzed for a representative periodic model from the literature over geometrical features of interest that include effects of curvature and pore spacing. Furthermore, the method is validated for a randomly generated two dimensional porous material with graded features. For one representative material, the proposed method had an average error in absorption coefficient (compared with a full thermoviscous computation) of 0.03 from 0.5 to 10 kHz, where the average absorption was 0.48. The method reduced computational time by two orders of magnitude as a result of having fewer degrees of freedom and less strict mesh refinement requirements.

A number of empirical and semi-phenomenological models have been developed for predicting sound absorption in porous materials. An excellent textbook was written by Allard and Atalla [20] which includes modeling methods for rigid and elastic

frame porous materials, multilayered absorbers and coupling, and poroelastic finite element methods. A popular empirical model for fibrous materials is the Delaney-Bazley model [72], which relies heavily on the measurement of static airflow resistivity for predicting acoustic performance. Miki [98] proposed modified expressions to the Delaney-Bazley model in order to preserve positive real surface impedance at low frequencies.

Semi-phenomenological models use effective microstructure properties of the porous material as well as the fluid properties to predict acoustical indicators. For example, a model by Kosten and Zwikker was derived for cylindrical pores [77]. For this geometry, the flow resitivity can be written analytically in terms of the radius, porosity, and viscosity of the fluid. Kosten and Zwikker derived an effective complex, frequency dependent density which took into account the viscous effects and an effective complex, frequency dependent bulk modulus which took into account thermal effects. For more complex geometries, models such as the Johnson-Champoux-Allard (JCA) [44], [45] model can be used, where the microstructure parameters used in this model are porosity, flow resitivity, tortuosity, viscous characteristic length, and thermal characterstic length. For a real porous material, use of the JCA model requires determination of these five intermediate variables. This usually requires use of specialized experimental techniques or numerical techniques based on a representative unit cell determined by statistical analysis. An example of this is a unit cell reconstruction of a metallic foam [89].

A complete thermoviscous acoustic finite element analysis of a three dimensional porous material based on the linearized compressible Navier-Stokes equations can be used to compute acoustic absorption. However, for many materials the model can be computationally intensive due to the large number of degrees of freedom (pressure, temperature, and velocity components) as well as the fine mesh required to resolve the

sharp gradients in temperature and velocity that occur near fluid-solid interfaces due to the thermal and viscous boundary layers. Additionally, there are porous materials for which it is difficult to determine or utilize effective microstructure properties, due to random or graded microstructure. For these cases, it is possible to estimate thermal and viscous losses using a Helmholtz acoustic finite element model despite not having the boundary layer physics in the mesh modeled.

One method to accomplish this is to assume boundary layer profiles everywhere in the geometry that are derived based on the boundary layer solutions for a fluid oscillating over a flat, infinite plate [84]. This method has been used to predict acoustic absorption in resonators [94] and metallic foams [46] for frequency regimes where the boundary layers do not overlap. Bossart [99] proposed an impedance-like boundary condition that required an initial guess and iteration post-processing scheme to converge. Additionally, Berggren [97] derived boundary condition terms that included both viscous and thermal effects that can be implemented without need for initial guess. This method has been used to compute acoustic absorption for resonators [100], however to the authors' knowledge this method has not been investigated for porous materials. Pierce [101] derived a similar acoustic boundary condition based on vorticity and entropy mode fields (see equation 10-4.12). Further approximate methods for modeling acoustic and thermal effects using finite element or boundary element methods are summarized in Chapter 2 of Nijhof [102].

The remaining sections are organized as follows. In Section 5.2.2, several methods for estimating acoustic absorption in porous materials are described including the proposed method. In Section 5.2.3, results are presented which compare predicted absorption trends for all methods discussed for a 2 dimensional representative porous material from the literature. The computational efficiency and accuracy of the proposed method are described in detail. Additionally in Section 5.2.3, acoustic

absorption is discussed for a randomly generated porous material which includes a graded microstructure. Such a material would be difficult to analyze using existing methods. The acoustic solution fields as well as boundary layer thickness relative to geometry is considered in Section 5.2.5 and the chapter is concluded in Section 5.2.6.

5.2.2 Methods of predicting acoustic absorption

Predicting the acoustic absorption of a porous material is important for proper material selection or material design and optimization in noise reduction applications. In this section, a method for estimating acoustic absorption based on viscous and thermal boundary layers modeled as boundary conditions is proposed and compared to several established methods. For the porous materials considered in this work, it is assumed the acoustic wavelength is long compared to pore sizes and the acoustic excitation is linear. For these materials, the acoustic losses come from viscous and thermal losses that occur in boundary layers surrounding the air and material surface. Absorption that occurs in the bulk of the fluid is negligible compared to boundary layer losses.

Johnson-Champoux-Allard model

The Johnson-Champoux-Allard [JCA] model [44], [45] is a well-known acoustic model for rigid-framed porous materials. A description of the JCA model including the implemented equations has been given previously in Section 3.1.3. Use of the JCA model for a real porous material requires determination of the five microstructure parameters of the material. This may require 1) statistical analysis and study of microstructure to determine representative pores, 2) experimental measurements, and/or 3) numerical computations on representative pores.

Thermoviscous acoustic finite element model

An alternative method for estimating absorption is to use the actual geometry of the material in a finite element model rather than homogenize the medium. This is advantageous if, for example, the geometry is known or can be obtained from techniques such as micro-computed tomography. Numerical solutions of the linearized Navier-Stokes equations in the frequency domain can be used together with a no-slip and iso-thermal boundary conditions along the surface of the material that is in contact with air. This is shown schematically for a fibrous material in Fig. 5·14 (b). For this simulation, the losses are localized close to the boundaries, thus the mesh must resolve the sharp gradients within the thin boundary layers.

This simulation is meant to model a plane acoustic wave incident upon a semi-infinite porous absorbing layer that is rigidly backed. Symmetry boundary conditions are prescribed along lateral boundaries of the layer. One end of the layer is prescribed with zero normal acoustic force (rigid), while the other end of the layer is prescribed with a uniform acoustic force, modeling an incident plane wave. The effect of any heat flow across the incident surface into the bulk medium is also assumed to be insignificant since the heat losses occur locally due to thermal boundary layers. The absorption is computed by first calculating the ratio of total pressure to velocity at the incident surface (surface impedance). Then Equations (5) and (6) can be used. For three dimensional simulations at high frequencies, this method can become computationally infeasible due to the need for a fine mesh in the vicinity of the boundary in addition to a large number of degrees of freedom per node. The following two subsections describe approximate methods for estimating acoustic absorption while still using finite element models of the geometry.

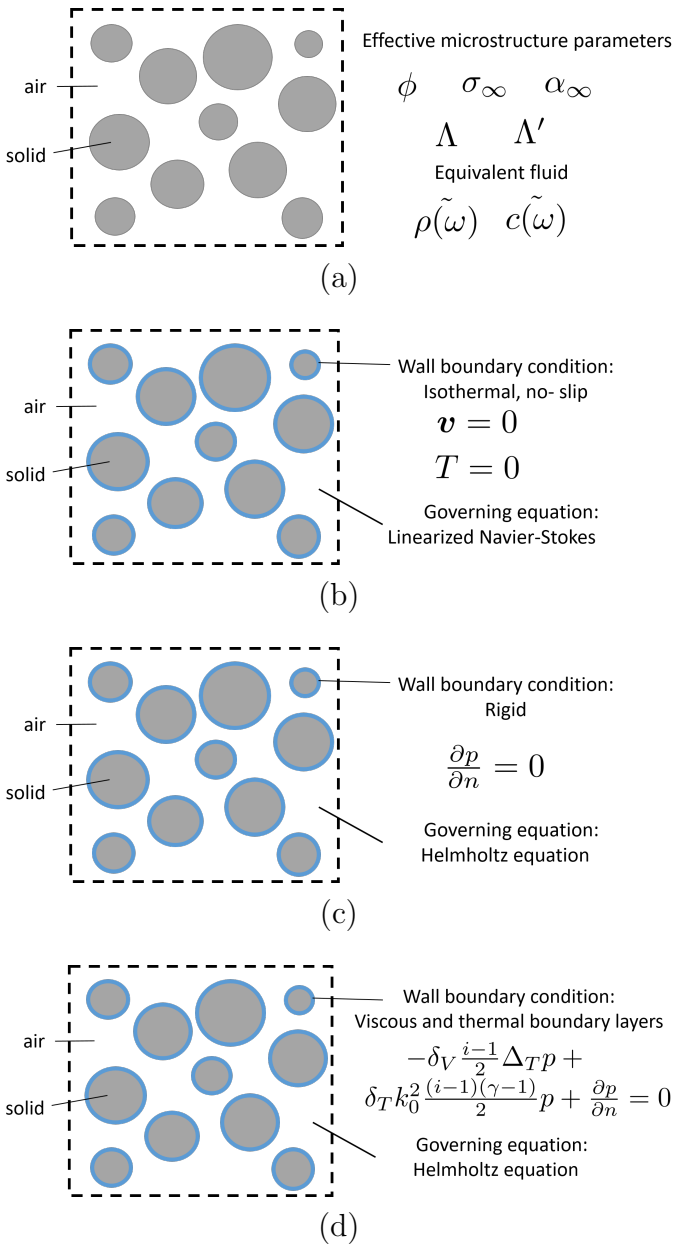

Figure 5·14: Summary of methods for computing acoustic absorption including (a) Johnson-Champoux-Allard model, (b) thermoviscous acoustic analysis, (c) Helmholtz acoustic analysis with rigid boundary conditions, and (d) Helmholtz acoustic analysis with viscous and thermal boundary layers modeled as boundary conditions.

Helmholtz finite element models

Helmholtz post-processing method If the boundary layer thickness is small compared to local geometry features, then velocity and temperature profiles in the bulk of the fluid are nearly unaffected by the velocity and temperature changes due to the boundary layer. This means that a Helmholtz solver can adequately predict the pressure and velocity profiles in the bulk of the fluid. For a finite element implementation as in Fig. 5·14 (c), the surfaces of the porous material are prescribed to be rigid.

A method proposed by Searby [84] uses this idea to compute viscous and thermal losses using analytical solutions for boundary layer profiles over a flat, infinite plate. This method has been discussed in depth in Section 5.1.

Proposed method In this subsection, a method for computing acoustic absorption is proposed using a Helmholtz solver in which the visco-thermal losses are modeled through a boundary condition. The basis of this method is the construction of a power absorbing boundary condition which replaces the boundary layer. In a previous work, Berggren [97] derived such a boundary condition term that includes both viscous and thermal effects

$$-\delta_V \frac{i-1}{2}\Delta_T p + \delta_T k_0^2 \frac{(i-1)(\gamma-1)}{2} p + \frac{\partial p}{\partial n} = 0 \tag{5.13}$$

The thermal and viscous boundary layer thicknesses are $\delta_T = \sqrt{2D/\omega}$ and $\delta_V = \sqrt{2\nu/\omega}$. Additionally, Δ_T is the sum of the second order spatial derivatives in the tangential direction. For a porous material, this boundary condition is prescribed along the surfaces in contact with air, shown schematically in Figure 5·14 (d). In this method, the losses are introduced in the finite element model through this boundary condition and not as a second post-processing step.

5.2.3 Results for a 2D fibrous sound absorbing material

In this section, first the proposed method is compared to the three other previously described methods for a representative periodic fibrous material. Secondly, the proposed method is implemented for a randomly generated graded microstructure. For the simulation results presented in this section, the commercial software COMSOL v5.4 was used. To implement the boundary condition in equation 5.13, a weak contribution was used in the weak form PDE interface. For the Helmholtz solution and Searby postproccessing calculations, the Pressure Acoustics interface was used. Lastly, the Thermoviscous Acoustics interface was used for the full linearized Navier-Stokes solution.

5.2.4 Periodic array of fibers

An ideal fibrous sound absorbing material can be modeled as a hexagonal array of cylinders, with radius r and spacing w as indicated in Figure 5·15. This arrangement has been studied extensively in the literature [2] and will be used as a benchmark case for comparison. For $r = 200\,\mu\text{m}$, $w = 200\,\mu\text{m}$, the five microstructure parameters are [2] $\phi = 0.74$, $\sigma = 3757\,\text{Ns/m}^4$, $\alpha_\infty = 1.14$, $\Lambda = 332\,\mu\text{m}$, and $\Lambda' = 569\,\mu\text{m}$.

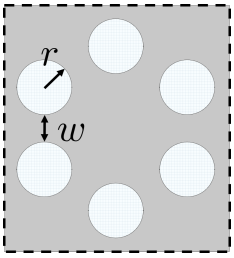

Figure 5·15: Perriodic unit cell from the literature [2].

For a porous layer of thickness $L = 16\,\text{mm}$, the acoustic absorption was computed using the JCA model, the thermoviscous acoustic solution, the Helmholtz post-processing method, and the proposed method.

The results for the normal incidence absorption coefficient are shown in Figure 5·16 for all methods. The thermoviscous solution is taken as the true solution, since the geometry is accurately modeled and the mesh is resolved with 10 elements across the boundary layer thickness. In Figure 5·16 it is clear that the Searby method is the most inaccurate, and the Berggren method is the most accurate. Additionally, there is some intermediate error between the JCA model and the thermoviscous solution. This may be attributed to the fact that for a sample of finite thickness, the array of fibers may be cut off at some non-integer multiple of the repeated pattern, thus it is not a perfectly periodic material.

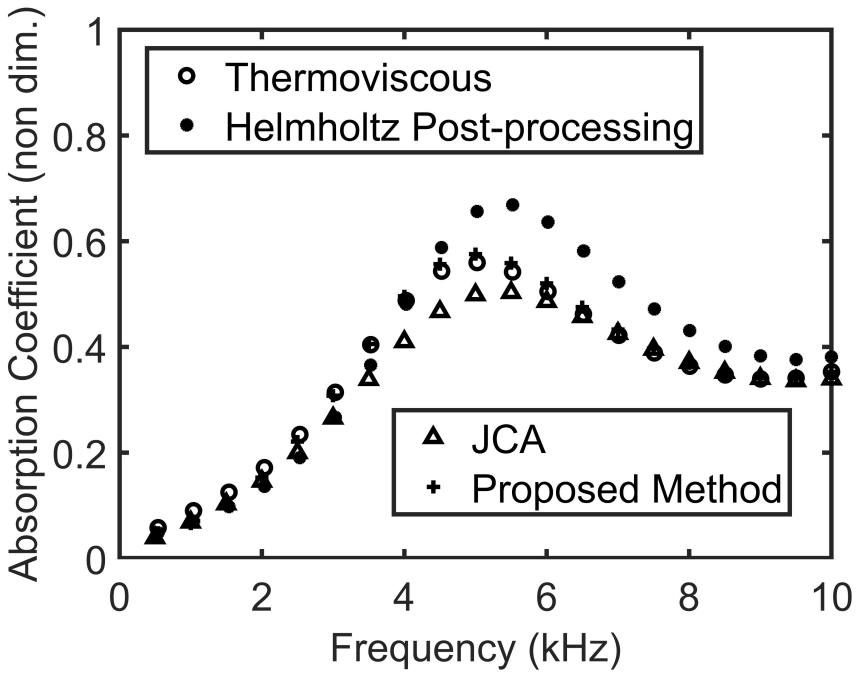

(a)

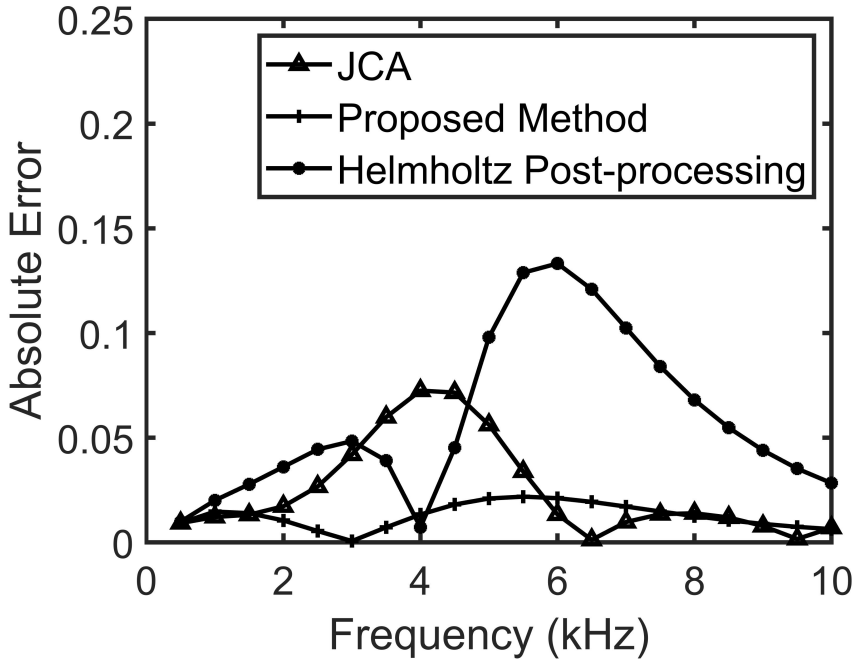

(b)

Figure 5·16: (a) Normal incidence absorption coefficient and (b) absolute error with thermoviscous result for a periodic array of fibers with $r = 200\,\mu\text{m}$, $w = 200\,\mu\text{m}$, and $L = 16\,\text{mm}$.

To examine the accuracy of the proposed method as well as the Helmholtz post-processing method, 91 models were generated with varying radius and spacing (varying from $100\,\mu m - 300\,\mu m$. The error metric used was a frequency-averaged absolute error in absorption coefficient. For both models, the error is plotted in Fig. 5·17.

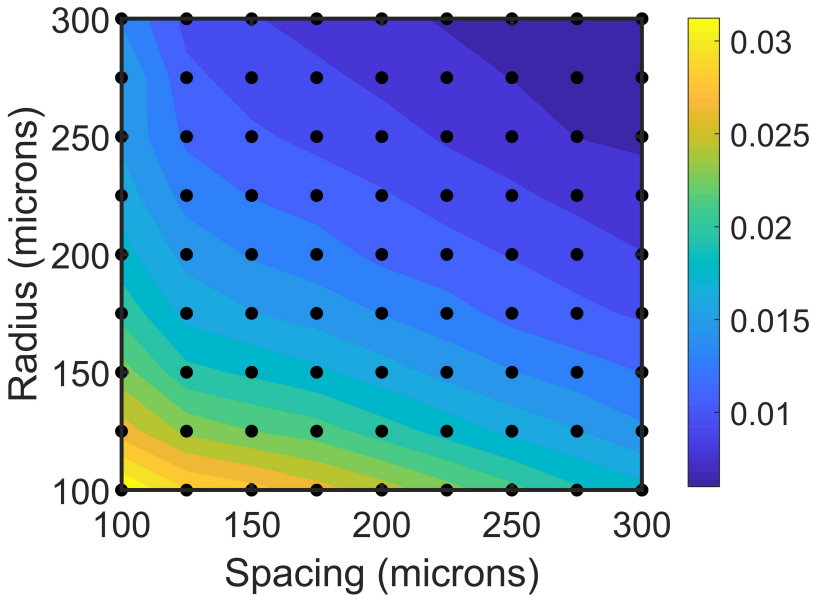

(a)

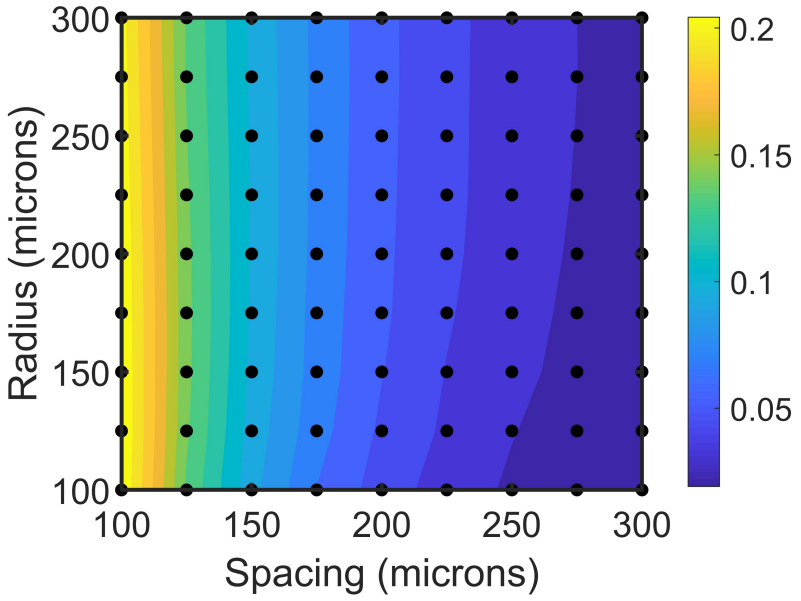

(b)

Figure 5·17: Frequency-averaged absolute error in absorption coefficient from the thermoviscous solution for (a) thermal and viscous boundary layers as acoustic boundary conditions (b) rigid boundary conditions.

Both approximate methods neglect effects of curvature as well as overlapping boundary layers. These effects are looked at in depth through varying radius and spacing, respectively. It can be seen in Fig. 5·17 (a) that the proposed method is quite accurate for both changes in radius and spacing. Even for the smallest and most tightly packed configuration ($r = 100\,\mu\text{m}$, $w = 100\,\mu\text{m}$), the frequency-averaged absolute error is 0.03. For Fig. 5·17 (b), it is interesting to note that the Helmholtz post-processing method appears insensitive to changes in radius. Furthermore, it is nearly an order of magnitude less accurate, especially at smaller spacing.

A significant advantage of the proposed method is the computational efficiency compared to a full thermoviscous solution. For example, for $r = 100\,\mu\text{m}$ and $w = 100\,\mu\text{m}$ on a desktop computer with 16 GB of RAM, the model for the proposed method had 31,175 DOFs and solved in 5 seconds for 20 frequencies. In contrast, the thermoviscous solution had approximately 1.8 million DOFs, which resulted from a refined mesh of 10 elements across the boundary layer thickness near the surface, as well as an increased number of solution variables (pressure, velocity, and temperature). The solution time was 12 minutes and 21 seconds (for 20 frequencies). Thus even for a fairly simple 2 dimensional model, a complete thermoviscous solution quickly becomes computationally expensive. For this model, the average error in absorption coefficient (compared with a thermoviscous computation) was 0.03 (see Fig. 5·17 (a)) from 0.5 to 10 kHz and the average absorption was 0.48.

Random array of fibers

The proposed method is also highly advantageous for materials with randomized or graded microstructure, where homogenization models are difficult to implement and a complete thermoviscous solution is expensive. To demonstrate this, a randomized array of fibers was generated as shown in Fig. 5·18. The structure was generated by

placing fibers in random positions with a minimum allowable spacing of $w = 100\,\mu\text{m}$. The fiber radius was linearly varied along the length from $r = 300 - 100\,\mu\text{m}$ from left to right. This nonhomegeneous composition allows for two non-symmetric directions of incidence (left to right and right to left), marked 1 and 2 in Fig. 5·18.

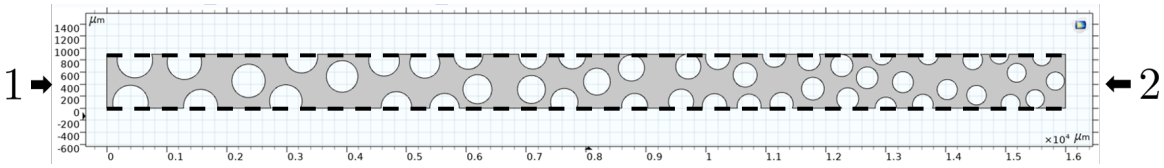

Figure 5·18: Randomly generated material with gradually decreasing fiber radius across the length. Minimum allowable fiber spacing of $w = 100\,\mu\text{m}$. Two directions of incidence are marked 1) left to right, and 2) right to left)

The proposed Berggren method was implemented on the random structure, and the results are shown in Figure 5·19. For both directions, the frequency-averaged absolute error is less than 0.025, and the frequency-averaged absorption is near 0.5. It is interesting to note that the absorption is directionally dependent. This result suggests that this method may be used to optimize or tune the microstructure to maximize absorption in certain frequency ranges.

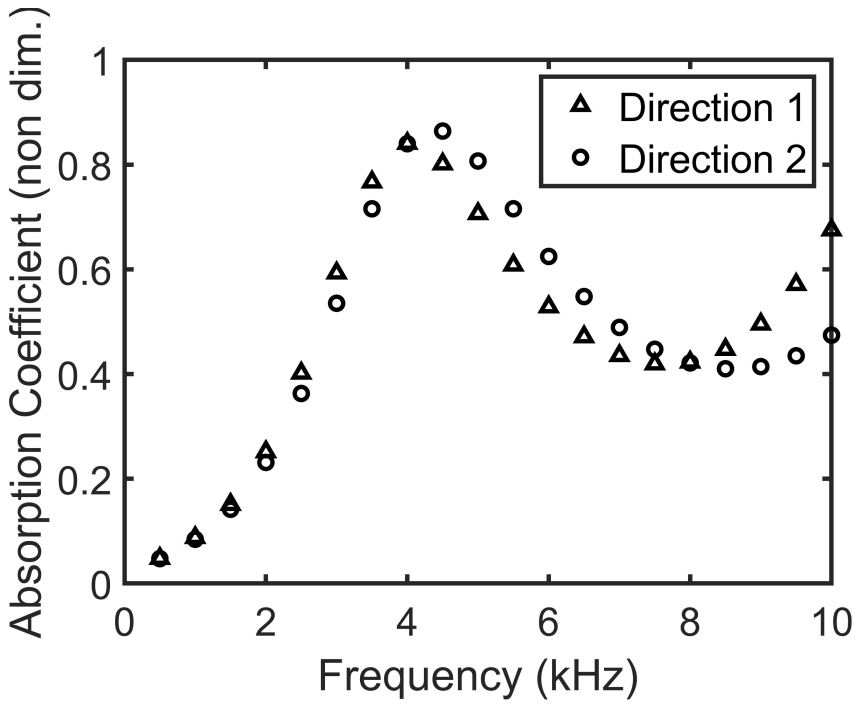

(a)

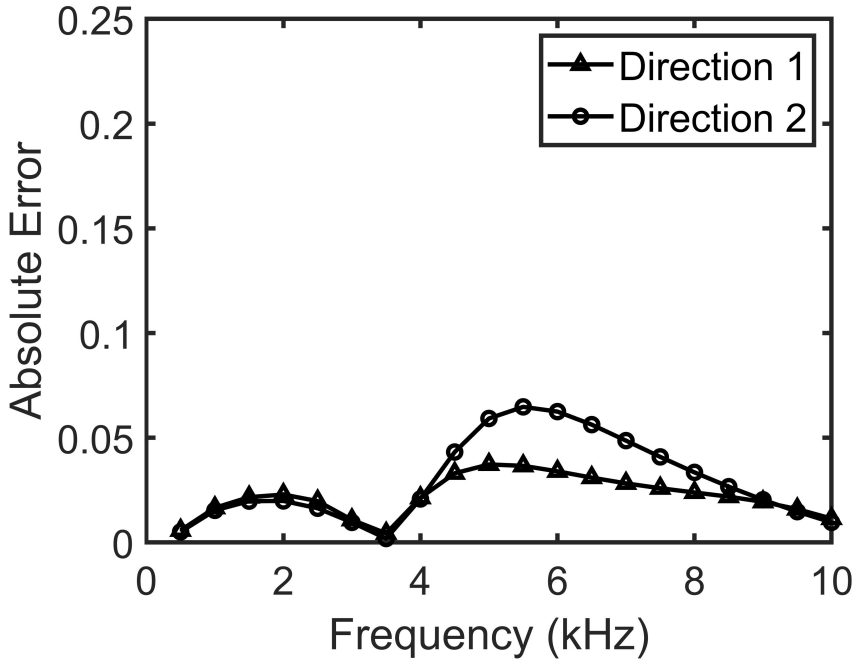

(b)

Figure 5·19: (a) Normal incidence absorption coefficient and (b) absolute error with thermoviscous result for a randomly generated graded geometry.

5.2.5 Discussion

As seen in the previous section, the accuracy of the proposed method is a function of the geometry structure, since the effects of curvature and overlapping boundry layers are not taken into account. To determine implications of these geometrical features, it is appropriate to compare them to the length scales of the viscous and thermal boundary layers. Consider the ratio of the width spacing w to the viscous boundary layer thickness. When this ratio is 2:1, the boundary layers of two opposite surfaces spaced w apart will be at the point of nearly overlapping. Therefore, for the proposed method to have higher accuracy, this ratio should be greater than 2:1. Fig. 5·20 shows a contour of the ratio of length scale to boundary layer thickness over the lengths and frequencies of interest studied in this work. Since the boundary layer thicknesses are functions of frequency, this non dimensional ratio increases with increasing frequency. From Fig. 5·20, it is clear that at higher frequency and larger length scales, the ratio is maximized. This trend in the color contour resembles the trend in Fig. 5·17, where the error is also minimized with increase in length scales.

Fig. 5·20 also applies for considering curvature in the geometry, since the effects of curvature are not accounted for in the derivation of the boundary condition. Furthermore, since the thickness of the thermal boundary layer in air is nearly the same as the viscous boundary layer, the same reasoning as previously described applies for overlapping thermal effects.

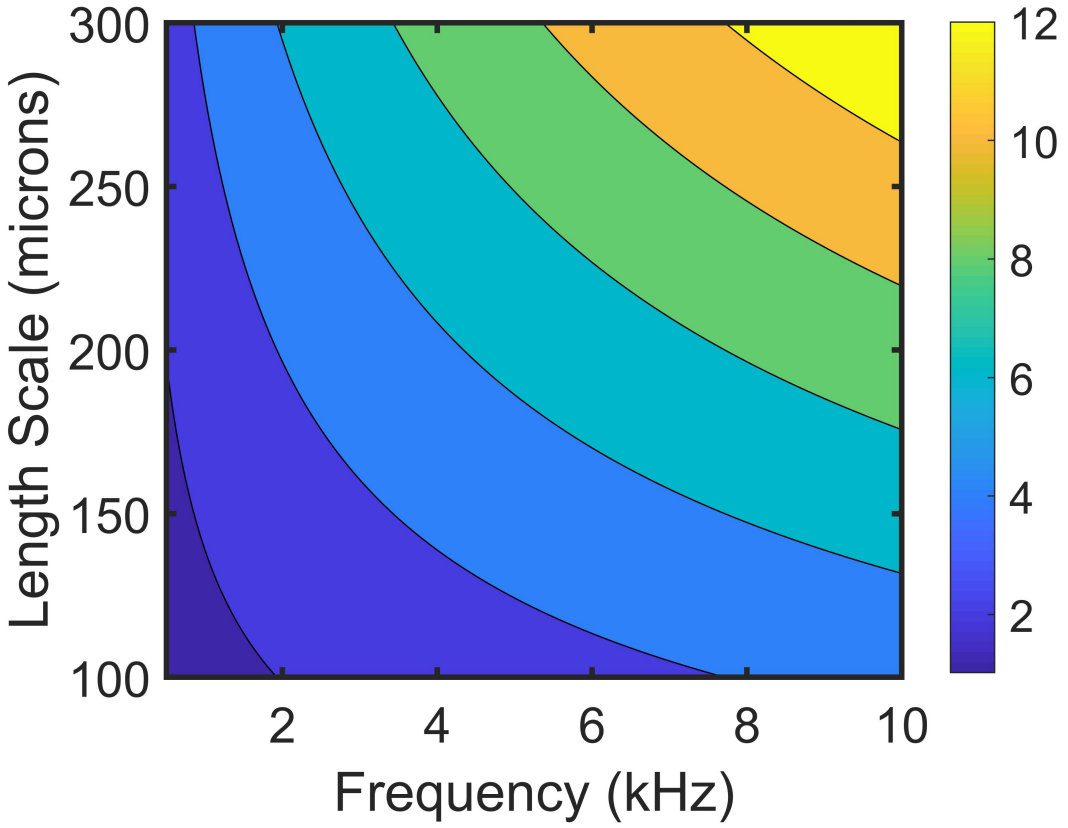

Figure 5·20: Contour of non-dimensional ratio of length scale to viscous boundary layer thickness.

To qualitatively examine the accuracy of the proposed method in further detail, the solution profiles for pressure and velocity at 5 kHz are plotted in Fig. 5·21 for the model with with $r = 300\,\mu\text{m}$ and $w = 300\,\mu\text{m}$. The direction of incidence for all models is left to right (applied pressure on the left and rigidly backed on the right). The steady state solution is a standing wave profile in the layer of the material. It can be seen that for Fig. 5·21 (a)-(d), the solution fields for the proposed method match well with the thermoviscous solution. However, the Helmholtz solution, which is used in the method described in section 5.2.2, appears to be quite different.

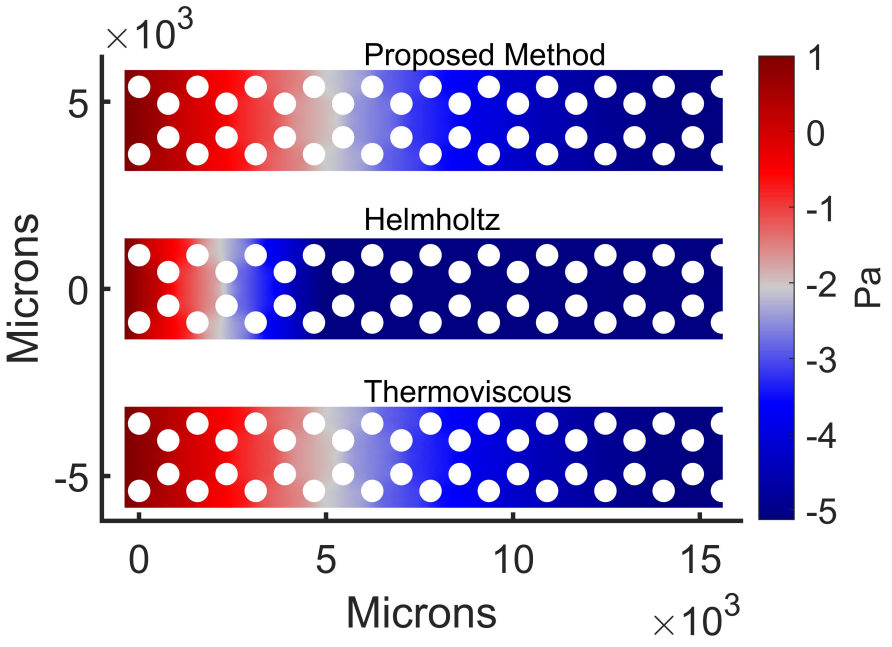
×10^3
Proposed Method
Helmholtz
Thermoviscous
Microns
5
0
-5
0
5
10
15
Microns
×10^3
1
0
-1
-2
-3
-4
-5
Pa

(a)

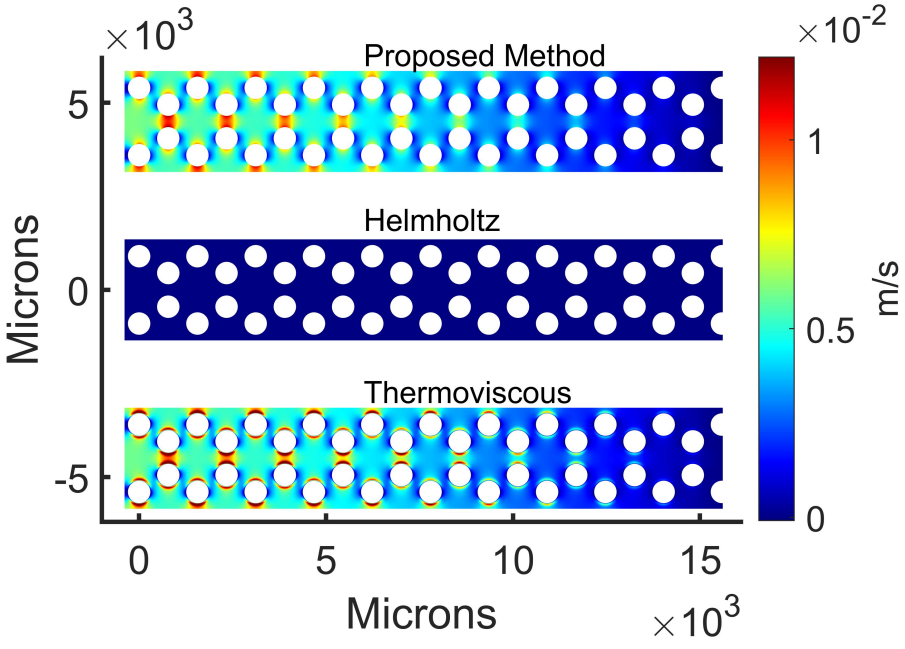
×10^3
Proposed Method
Helmholtz
Thermoviscous
Microns
5
0
-5
0
5
10
15
Microns
×10^3
×10^-2
1
0.5
0
m/s

(b)

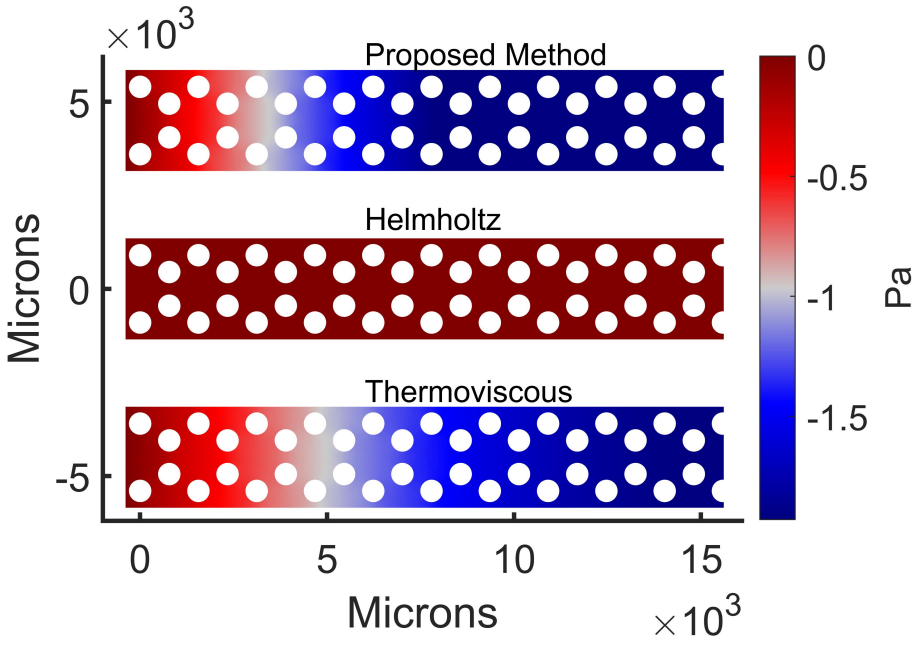

(c)

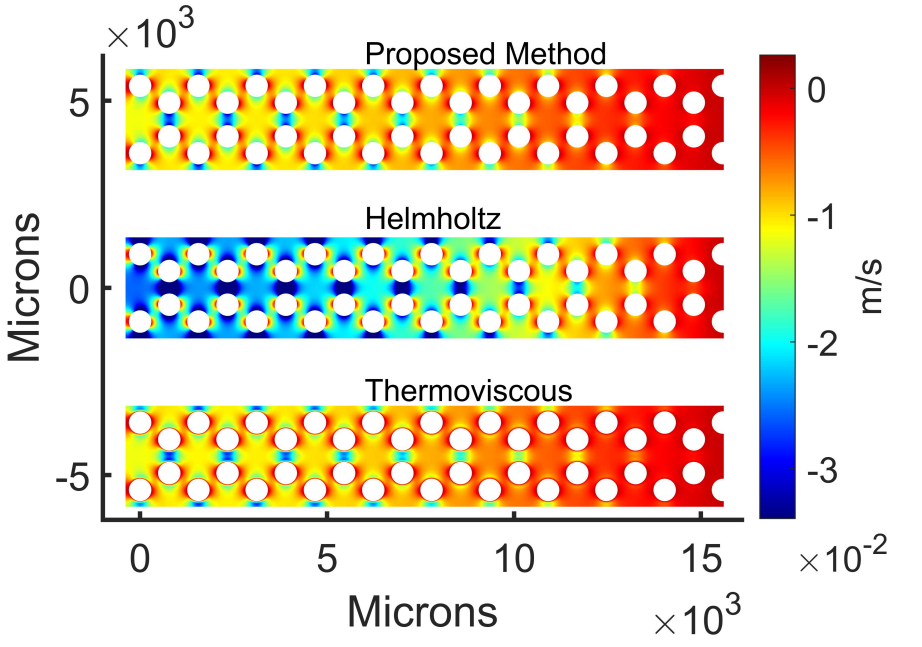

(d)

Figure 5·21: Acoustic fields at 5 kHz (a) real pressure, (b) real velocity, (c) imaginary pressure, and (d) imaginary velocity for a a periodic array of fibers with $r = 300\,\mu\text{m}$, $w = 300\,\mu\text{m}$

Recall that there is no damping inherent in the Helmholtz solution. This results in a zero imaginary pressure in the standing wave for a real prescribed pressure and rigid backing, because all the reflected pressure is in phase with the incident. For the same reasoning, there is zero real velocity for the Helmholtz solution. The real pressure and imaginary velocity fields are correct in mode shape but off in order of magnitude. This indicates that the geometry of the model is such that out of phase components are significantly altering the bulk solution field.

This is not true for all geometries. Consider the same periodic structure with $r = 100\,\mu\text{m}$ and $w = 600\,\mu\text{m}$ as shown in Fig. 5·22.

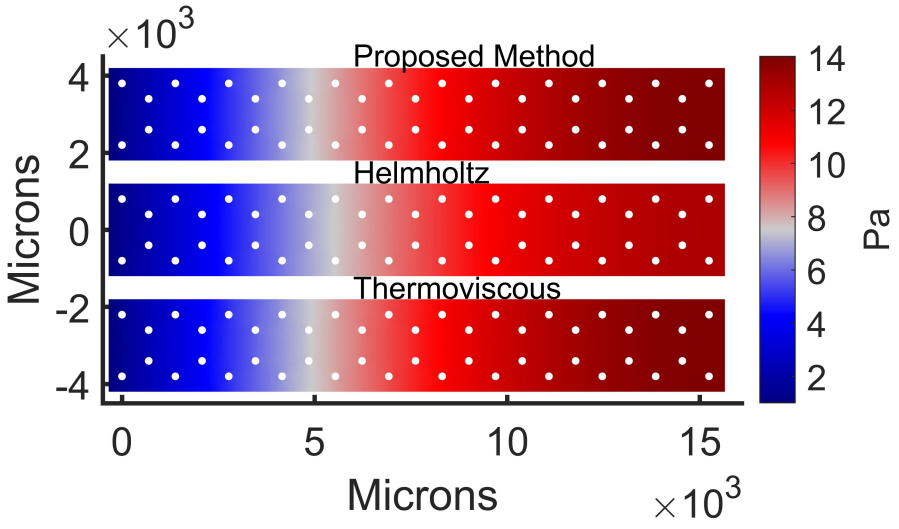
×10^3
Proposed Method
Helmholtz
Thermoviscous
Microns
4
2
0
-2
-4
0
5
10
15
Microns
×10^3
14
12
10
8
6
4
2
Pa

(a)

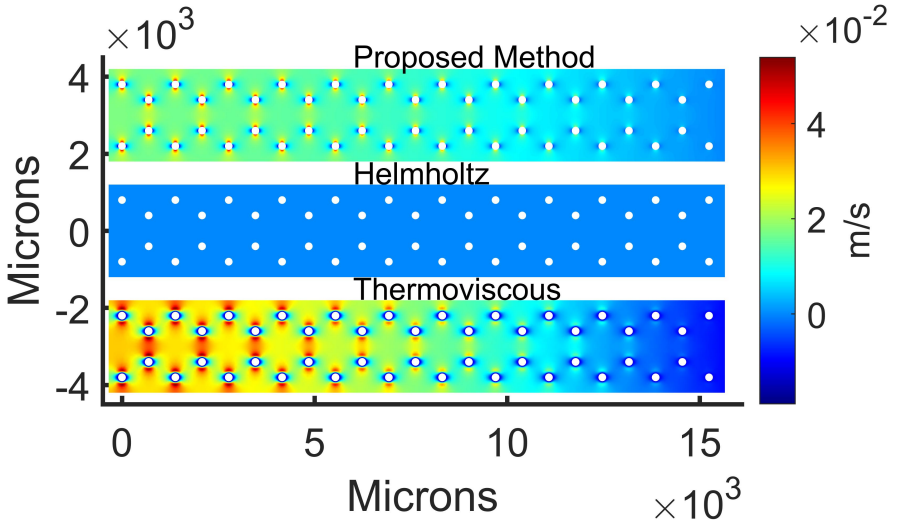
×10^3
Proposed Method
Helmholtz
Thermoviscous
Microns
4
2
0
-2
-4
0
5
10
15
Microns
×10^3
×10^-2
4
2
0
m/s

(b)

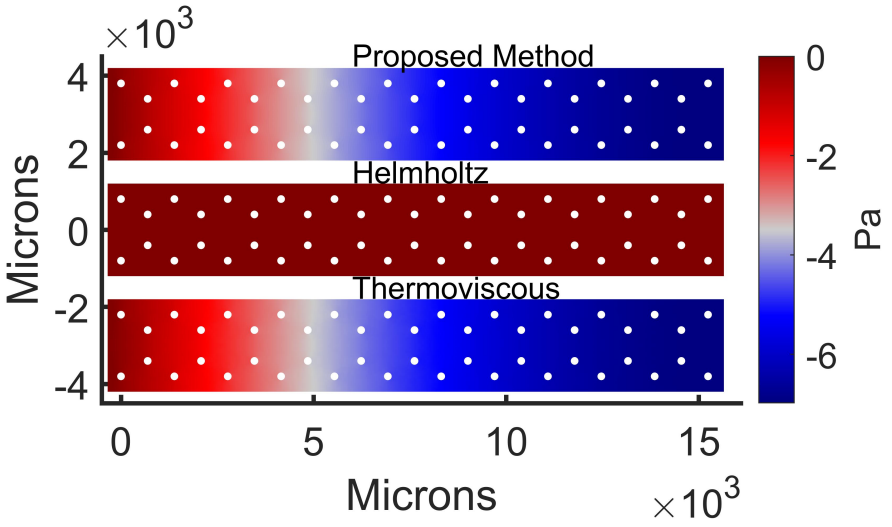

(c)

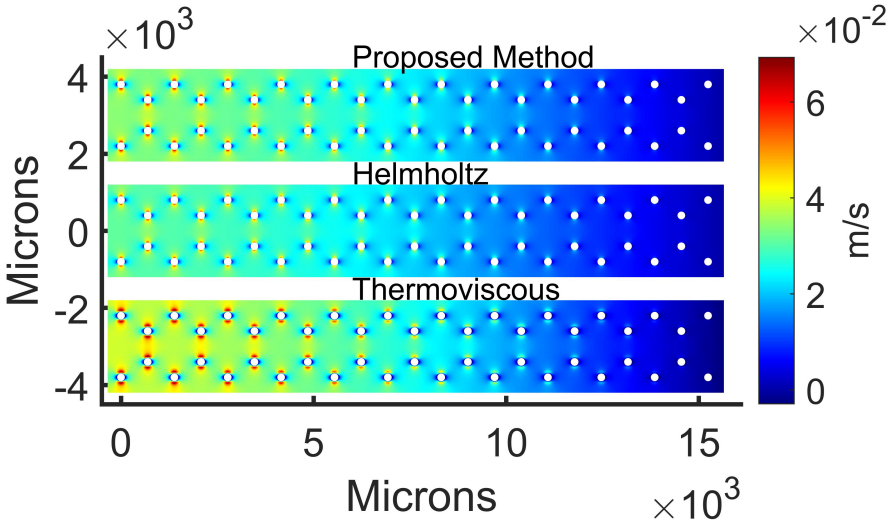

(d)

Figure 5·22: Acoustic fields at 5 kHz (a) real pressure, (b) real velocity, (c) imaginary pressure, and (d) imaginary velocity for a a periodic array of fibers with $r = 100\,\mu\text{m}$, $w = 600\,\mu\text{m}$

Here, the Helmholtz solution shows improvement compared to the thermoviscous solution for both real pressure and imaginary velocity. This is due to the large increase in spacing w and is similar to trends predicted in Figure 5·17 (b), where error decreases significantly with increasing spacing. The solution fields predicted by the proposed method (Berggren) appear correct in terms of pressure. For velocity, there is a larger discrepancy locally in the field surrounding the fibers. This confirms that the accuracy of the method is dependent on curvature, a trend seen also in Figure 5·17 (a).

5.2.6 Conclusion

In this section, a method for estimating acoustic absorption in porous materials is presented in which visco-thermal losses are modeled as a boundary condition of the Helmholtz equation for the acoustic pressure. The proposed method was shown to have high accuracy and decreased computational time by more than two orders of magnitude compared to a full thermoviscous acoustic solver. Additionally, the proposed method is advantageous for modeling highly randomized or graded microstructures that can be difficult the model with existing methods. Implications of geometrical assumptions such as non-overlapping boundary layers and curvature are analyzed numerically and discussed, providing guidelines for use of the proposed method.

Chapter 6

Summary and Future Work

This chapter serves as an overall summary of this thesis and discussion of concepts for future work. The reader should refer to each individual chapter's conclusion subsection for more detailed commentary. In Section 6.1, the significance of each chapter is summarized in terms of listing the research accomplishments associated with each chapter. In Section 6.2, a summary of potential future work is listed as it pertains to each chapter.

6.1 Summary of Novelty and Significance

In this section, the novelty and significance of this thesis is presented in an itemized list corresponding to each chapter.

6.1.1 Bulk Mechanical Properties of Open-cell Metallic Foams (Chapter 2)

- Foam microstructures were digitally designed using computer graphics algorithms and imported into finite element analysis software to determine effective bulk mechanical properties. Resulting properties showed order of magnitude agreement with published scaling laws, however higher accuracy was achieved by inclusion of additional terms in a quadratic fit for relative density.

- Five separate commercially available metallic foams with varying porosity, pore size, and host metal were analyzed structurally using high fidelity meshes cre-

ated from micro-CT scans. The analysis highlighted the importance of foam microstructure that results from manufacturing processes including strut density (hollow versus solid) as well as pore elongation from gravity.

6.1.2 Acoustic and Bulk Mechanical Properties of Metallic Foams after Triaxial Hydrostatic Compression (Chapter 3)

- A method of triaxial compression of metallic foams was presented which utilized hydrostatic pressure to preferentially alter the microstructure.
- Due to the unique microstructure of the compressed samples, a significant improvement in sound absorption coefficient was seen compared to conventional samples.
- Compressed foams were tested structurally using a load frame and digital image correlation. Compared to conventional foams, compressed foams exhibited higher compliance, higher toughness, and a reduced Poisson ratio.

6.1.3 Acoustic Absorption and Vibration Damping by Saturated Metallic Foam (Chapter 4)

- A composite foam consisting of a metallic foam embedded with a polyurethane foam was fabricated to leverage the high stiffness and high absorption properties of the metal and polyurethane, respectively. Sound absorption was modeled using a lumped parameter model. Experimental results indicated that the composite foam had significantly higher sound absorption that the conventional metallic foam.
- Metallic foams saturated with viscous liquids were tested experimentally to measure damping. The best performing material was a metallic foam saturated

with petroleum jelly, with an increase in damping ratio from 0.006 to 0.07 for a transient experiment.

6.1.4 Estimating Acoustic Absorption in Foams Using Finite Element Analysis and Boundary Layer Theory (Chapter 5)

- A method for estimating acoustic absorption in metallic foams was proposed and demonstrated. It used high fidelity models of the air region within the pores constructed from micro-CT scans. The method incorporated boundary layer theory solutions over an infinite flat plate with a lossless Helmholtz solver.

- A second method for estimating acoustic absorption in metallic foams was proposed using thermal and viscous boundary layers modeled as acoustic boundary conditions in a lossless Helmholtz solver. This second method is recommended due to higher accuracy for models with the same geometrical features. However, the second method can be more difficult to implement in existing commercially available software.

6.2 Future Work

Throughout the coarse of this work, many ideas have sparked from conversations with my advisor, collaborators, and lab mates. For those ideas that I have been unable to pursue, but still may have some merit, a comprehensive list is presented below as it corresponds to each respective chapter.

6.2.1 Bulk Mechanical Properties of Open-cell Metallic Foams (Chapter 2)

- Extensions of finite element analysis of commercial foams to include foams with a filler material.

6.2.2 Acoustic and Bulk Mechanical Properties of Metallic Foams after Triaxial Hydrostatic Compression (Chapter 3)

- Plastic deformation of foams to higher compression ratios (greater than two) in order to determine optimal compression ratio to maximize sound absorption.
- Further investigation of structural properties as a function of compression ratio. Investigation of the applicability of Gibson scaling laws for compressed foams.
- Further investigation into the the relative importance of geometry versus plastic deformation as a mechanism for inducing negative Poisson ratio materials.

6.2.3 Acoustic Absorption and Vibration Damping by Saturated Metallic Foam (Chapter 4)

- Additional measurements of fluid saturated metallic foams to determine the damping ratio as a function of frequency.
- Analysis and experiments of vibration damping of metallic foams saturated with viscoelastic materials such as rubber.
- Analysis and experiments measuring acoustic absorption of fluid saturated metallic foams in water.

6.2.4 Estimating Acoustic Absorption in Foams Using Finite Element Analysis and Boundary Layer Theory (Chapter 5)

- Investigations into optimizing a microstructure for specific surface area.
- Investigations into applicability of the proposed approximate methods for flexible foams. This would involve a fluid-structure interaction problem which would be able to capture structural damping as well and viscous and thermal boundary layer losses.

- Use of the derived [thermal and viscous boundary layer] boundary condition equations for a general fluid-structure interaction problem. For example, for a nano-scale beam vibrating in air, nearly all the energy is dissipated due to viscosity (negligible radiation and thermal losses). Is it possible to write the viscous equation in terms of structural degrees of freedom which would then simplify the fluid-structure interaction to merely a separate boundary condition (no need to mesh or model the air).

Bibliography

[1] N. Dukhan, Metal Foams: Fundamentals and Applications, DEStech Publications, Inc, 2013.

[2] C. Perrot, F. Chevillotte, R. Panneton, Bottom-up approach for microstructure optimization of sound absorbing materials, The Journal of the Acoustical Society of America 124 (2) (2008) 940–948.

[3] J. Banhart, Manufacture, characterisation and application of cellular metals and metal foams, Progress in Materials Science 46 (6) (2001) 559–632.

[4] M. F. Ashby, A. Evans, N. Fleck, L. Gibson, J. Hutchinson, H. Wadley, F. Delale, Metal foams: a design guide, Applied Mechanics Reviews 54 (6) (2001) B105–B106.

[5] L. J. Gibson, M. F. Ashby, Cellular Solids: Structure and Properties, Cambridge University Press, 1999.

[6] V. Deshpande, M. Ashby, N. Fleck, Foam topology: bending versus stretching dominated architectures, Acta Materialia 49 (6) (2001) 1035–1040.

[7] H. Zhu, J. Knott, N. Mills, Analysis of the elastic properties of open-cell foams with tetrakaidecahedral cells, Journal of the Mechanics and Physics of Solids 45 (3) (1997) 319–343.

[8] C. Chen, R. Lakes, Holographic study of conventional and negative Poisson's ratio metallic foams: elasticity, yield and micro-deformation, Journal of Materials Science 26 (20) (1991) 5397–5402.

[9] J. Choi, R. Lakes, Non-linear properties of metallic cellular materials with a negative Poisson's ratio, Journal of Materials Science 27 (19) (1992) 5375–5381.

[10] R. Lakes, Foam structures with a negative Poisson's ratio, Science 235 (1987) 1038–1041.

[11] K. Evans, Tailoring the negative Poisson's ratio, Chemical Industry 20 (1990) 654.

[12] C. Kosten, C. Zwikker, Properties of sponge rubber as a material for damping vibration and shock, Rubber Chemistry and Technology 12 (1) (1939) 105–111.

[13] A. Gent, K. Rusch, Viscoelastic behavior of open-cell foams, in: Cellular plastics: proceedings of a conference, Natick, Massachusetts, April 13-15, 1966, no. 1462, National Academies, 1967, p. 42.

[14] N. Hilyard, S. Kanakkanatt, The dynamic mechanical behaviour of liquid-filled foams, Journal of Physics D: Applied Physics 3 (6) (1970) 906.

[15] W. Xu, C. Jiang, J. Zhang, Improvement in underwater acoustic absorption performance of open-celled sic foam, Colloids and Surfaces A: Physicochemical and Engineering Aspects 482 (2015) 568–574.

[16] X. Wang, Porous metal absorbers for underwater sound, The Journal of the Acoustical Society of America 122 (5) (2007) 2626–2635.

[17] H. Cheng, F. Han, Compressive behavior and energy absorbing characteristic of open cell aluminum foam filled with silicate rubber, Scripta Materialia 49 (6) (2003) 583–586.

[18] M. Vesenjak, L. Krstulović-Opara, Z. Ren, A. Öchsner, Ž. Domazet, Experimental study of open-cell cellular structures with elastic filler material, Experimental Mechanics 49 (4) (2009) 501.

[19] S. Yin, N. Rayess, Characterization of polymer-metal foam hybrids for use in vibration dampening and isolation, Procedia Materials Science 4 (2014) 311–316.

[20] J. Allard, N. Atalla, Propagation of Sound in Porous Media: Modelling Sound Absorbing Materials, 2nd Edition, John Wiley & Sons, 2009.

[21] T. J. Lu, A. Hess, M. Ashby, Sound absorption in metallic foams, Journal of Applied Physics 85 (11) (1999) 7528–7539.

[22] F. Han, G. Seiffert, Y. Zhao, B. Gibbs, Acoustic absorption behaviour of an open-celled aluminium foam, Journal of Physics D: Applied Physics 36 (3) (2003) 15–24.

[23] T. Wierzbicki, M. Doyoyo, Determination of the local stress-strain response of foams, Journal of Applied Mechanics 70 (2) (2003) 204–211.

[24] S. Osher, R. Fedkiw, K. Piechor, Level set methods and dynamic implicit surfaces, Applied Mechanics Reviews 57 (3) (2004) B15–B15.

[25] A. H. Schoen, Infinite Periodic Minimal Surfaces Without Self-intersections, National Aeronautics and Space Administration, 1970.

[26] Q. Fang, D. A. Boas, Tetrahedral mesh generation from volumetric binary and grayscale images, in: 2009 IEEE International Symposium on Biomedical Imaging: From Nano to Macro, IEEE, 2009, pp. 1142–1145.

[27] J. Zhou, P. Shrotriya, W. Soboyejo, Mechanisms and mechanics of compressive deformation in open-cell al foams, Mechanics of Materials 36 (8) (2004) 781–797.

[28] P. Fanelli, A. Evangelisti, P. Salvini, F. Vivio, Modelling and characterization of structural behaviour of Al open-cell foams, Materials & Design 114 (2017) 167–175.

[29] T. Nieh, K. Higashi, J. Wadsworth, Effect of cell morphology on the compressive properties of open-cell aluminum foams, Materials Science and Engineering: A 283 (1-2) (2000) 105–110.

[30] W.-Y. Jang, S. Kyriakides, On the crushing of aluminum open-cell foams: Part I. experiments, International Journal of Solids and Structures 46 (3-4) (2009) 617–634.

[31] E. Andrews, W. Sanders, L. J. Gibson, Compressive and tensile behaviour of aluminum foams, Materials Science and Engineering: A 270 (2) (1999) 113–124.

[32] E. Andrews, G. Gioux, P. Onck, L. Gibson, Size effects in ductile cellular solids. Part II: experimental results, International Journal of Mechanical Sciences 43 (3) (2001) 701–713.

[33] D. Li, L. Dong, R. S. Lakes, The properties of copper foams with negative Poisson's ratio via resonant ultrasound spectroscopy, Physica Status Solidi (b) 250 (10) (2013) 1983–1987.

[34] D. T. Queheillalt, D. D. Hass, D. J. Sypeck, H. N. Wadley, Synthesis of open-cell metal foams by templated directed vapor deposition, Journal of Materials Research 16 (4) (2001) 1028–1036.

[35] H. Choe, D. C. Dunand, Synthesis, structure, and mechanical properties of Ni–Al and Ni–Cr–Al superalloy foams, Acta Materialia 52 (5) (2004) 1283–1295.

[36] M. Ashby, The properties of foams and lattices, Philosophical Transactions of the Royal Society A: Mathematical, Physical and Engineering Sciences 364 (1838) (2006) 15–30.

[37] E. Andrews, Open-cell foams with hollow struts: mechanical property enhancements, Materials Letters 60 (5) (2006) 618–620.

[38] H. Fan, D. Fang, Enhancement of mechanical properties of hollow-strut foams: analysis, Materials & Design 30 (5) (2009) 1659–1666.

[39] B. Moore, T. Jaglinski, D. Stone, R. Lakes, On the bulk modulus of open cell foams, Cellular Polymers 26 (1) (2007) 1–10.

[40] P. Viot, Hydrostatic compression on polypropylene foam, International Journal of Impact Engineering 36 (7) (2009) 975–989.

[41] V. Deshpande, N. Fleck, Isotropic constitutive models for metallic foams, Journal of the Mechanics and Physics of Solids 48 (6-7) (2000) 1253–1283.

[42] P. Bai, X. Shen, X. Zhang, X. Yang, Q. Yin, A. Liu, Influences of compression ratios on sound absorption performance of porous nickel–iron alloy, Metals 8 (7) (2018) 539.

[43] P. Bai, X. Yang, X. Shen, X. Zhang, Z. Li, Q. Yin, G. Jiang, F. Yang, Sound absorption performance of the acoustic absorber fabricated by compression and microperforation of the porous metal, Materials & Design 167 (2019) 107637.

[44] D. L. Johnson, J. Koplik, R. Dashen, Theory of dynamic permeability and tortuosity in fluid-saturated porous media, Journal of Fluid Mechanics 176 (1987) 379–402.

[45] Y. Champoux, J.-F. Allard, Dynamic tortuosity and bulk modulus in air-saturated porous media, Journal of Applied Physics 70 (4) (1991) 1975–1979.

[46] M. J. Cops, J. G. McDaniel, E. A. Magliula, D. J. Bamford, Analysis of thermal and viscous boundary layers in acoustic absorption by metallic foam, The Journal of the Acoustical Society of America 146 (1) (2019) 649–655.

[47] ASTM Standard E1050-12, Standard test method for impedance and absorption of acoustical materials using a tube, two microphones, and a digital frequency analysis system.

[48] D. Lafarge, P. Lemarinier, J. F. Allard, V. Tarnow, Dynamic compressibility of air in porous structures at audible frequencies, The Journal of the Acoustical Society of America 102 (4) (1997) 1995–2006.

[49] S. R. Pride, F. D. Morgan, A. F. Gangi, Drag forces of porous-medium acoustics, Physical Review B 47 (9) (1993) 4964.

[50] F. Yang, X. Shen, P. Bai, X. Zhang, Z. Li, Q. Yin, Optimization and validation of sound absorption performance of 10-layer gradient compressed porous metal, Metals 9 (5) (2019) 588.

[51] K. Boomsma, D. Poulikakos, The effects of compression and pore size variations on the liquid flow characteristics in metal foams, Journal of Fluids Engineering 124 (1) (2002) 263–272.

[52] A. Hernández, Combined flow and heat transfer characterization of open cell aluminum foams, M.S. Thesis, University of Puerto Rico, Mayagüez campus, 2005, https://scholar.uprm.edu/handle/20.500.11801/845.

[53] M. B. Mansour, E. Ogam, A. Jelidi, A. S. Cherif, S. B. Jabrallah, Influence of compaction pressure on the mechanical and acoustic properties of compacted earth blocks: An inverse multi-parameter acoustic problem, Applied Acoustics 125 (2017) 128–135.

[54] Y. Atalla, R. Panneton, Inverse acoustical characterization of open cell porous media using impedance tube measurements, Canadian Acoustics 33 (1) (2005) 11–24.

[55] B. Castagnede, A. Aknine, B. Brouard, V. Tarnow, Effects of compression on the sound absorption of fibrous materials, Applied Acoustics 61 (2) (2000) 173–182.

[56] B. Castagnède, J. Tizianel, A. Moussatov, A. Aknine, B. Brouard, Parametric study of the influence of compression on the acoustical absorption coefficient of automotive felts, Comptes Rendus de l'Académie des Sciences-Series IIB-Mechanics 329 (2) (2001) 125–130.

[57] J. Zhou, S. Allameh, W. Soboyejo, Microscale testing of the strut in open cell aluminum foams, Journal of Materials Science 40 (2) (2005) 429–439.

[58] P. J. Veale, Investigation of the behavior of open cell aluminum foam, M.S. Thesis, University of Massachusetss at Amherst, 2010, https://scholarworks.umass.edu/theses/443/.

[59] J. P. Arenas, M. J. Crocker, Recent trends in porous sound-absorbing materials, Sound & Vibration 44 (7) (2010) 12–18.

[60] N. Kino, G. Nakano, Y. Suzuki, Non-acoustical and acoustical properties of reticulated and partially reticulated polyurethane foams, Applied Acoustics 73 (2) (2012) 95–108.

[61] O. Doutres, N. Atalla, K. Dong, A semi-phenomenological model to predict the acoustic behavior of fully and partially reticulated polyurethane foams, Journal of Applied Physics 113 (5) (2013) 054901.

[62] F. Chevillotte, R. Panneton, Elastic characterization of closed cell foams from impedance tube absorption tests, The Journal of the Acoustical Society of America 122 (5) (2007) 2653–2660.

[63] C. Perrot, F. Chevillotte, M. Tan Hoang, G. Bonnet, F.-X. Bécot, L. Gautron, A. Duval, Microstructure, transport, and acoustic properties of open-cell foam samples: Experiments and three-dimensional numerical simulations, Journal of Applied Physics 111 (1) (2012) 014911.

[64] J.-L. Wojtowicki, R. Panneton, Improving the efficiency of sealing parts for hollow body network, Tech. rep., SAE Technical Paper (2005).

[65] J. F. Allard, C. Depollier, P. Guignouard, P. Rebillard, Effect of a resonance of the frame on the surface impedance of glass wool of high density and stiffness, The Journal of the Acoustical Society of America 89 (3) (1991) 999–1001.

[66] K. V. Horoshenkov, A. Khan, F.-X. Bécot, L. Jaouen, F. Sgard, A. Renault, N. Amirouche, F. Pompoli, N. Prodi, P. Bonfiglio, et al., Reproducibility experiments on measuring acoustical properties of rigid-frame porous media (round-robin tests), The Journal of the Acoustical Society of America 122 (1) (2007) 345–353.

[67] T. E. Vigran, L. Kelders, W. Lauriks, P. Leclaire, T. Johansen, Prediction and measurements of the influence of boundary conditions in a standing wave tube, Acta Acustica United with Acustica 83 (3) (1997) 419–423.

[68] C. Kosten, J. Janssen, Acoustic properties of flexible and porous materials, Acta Acustica United with Acustica 7 (6) (1957) 372–378.

[69] M. A. Biot, Theory of propagation of elastic waves in a fluid-saturated porous solid. I. low-frequency range, The Journal of the Acoustical Society of America 28 (2) (1956) 168–178.

[70] M. Biot, D. Willis, The elastic coefficients of the theory of consolidation, Journal of Applied Mechanics 24 (1957) 594–601.

[71] M. A. Biot, Generalized theory of acoustic propagation in porous dissipative media, The Journal of the Acoustical Society of America 34 (9A) (1962) 1254–1264.

[72] M. Delany, E. Bazley, Acoustical properties of fibrous absorbent materials, Applied Acoustics 3 (2) (1970) 105–116.

[73] M. Brennan, W. To, Acoustic properties of rigid-frame porous materials – an engineering perspective, Applied Acoustics 62 (7) (2001) 793–811.

[74] Y. Yang, B. Li, Z. Chen, N. Sui, Z. Chen, M.-U. Saeed, Y. Li, R. Fu, C. Wu, Y. Jing, Acoustic properties of glass fiber assembly-filled honeycomb sandwich panels, Composites Part B: Engineering 96 (2016) 281–286.

[75] H. Jiang, Y. Wang, Phononic glass: A robust acoustic-absorption material, The Journal of the Acoustical Society of America 132 (2) (2012) 694–699.

[76] X. Olny, C. Boutin, Acoustic wave propagation in double porosity media, The Journal of the Acoustical Society of America 114 (1) (2003) 73–89.

[77] C. Zwikker, C. W. Kosten, Sound Absorbing Materials, Elsevier, 1949.

[78] K. V. Horoshenkov, A. Hurrell, J.-P. Groby, A three-parameter analytical model for the acoustical properties of porous media, The Journal of the Acoustical Society of America 145 (4) (2019) 2512–2517.

[79] F. Scheffler, R. Herrmann, W. Schwieger, M. Scheffler, Preparation and properties of an electrically heatable aluminium foam/zeolite composite, Microporous and Mesoporous Materials 67 (1) (2004) 53–59.

[80] W. Patten, S. Sha, C. Mo, A vibrational model of open celled polyurethane foam automotive seat cushions, Journal of Sound and Vibration 217 (1) (1998) 145–161.

[81] M. Bianchi, F. Scarpa, Vibration transmissibility and damping behaviour for auxetic and conventional foams under linear and nonlinear regimes, Smart Materials and Structures 22 (8) (2013) 084010.

[82] P. Göransson, Acoustic and vibrational damping in porous solids, Philosophical Transactions of the Royal Society A: Mathematical, Physical and Engineering Sciences 364 (1838) (2006) 89–108.

[83] S. R. Singiresu, Mechanical vibrations, Addison Wesley, 1995.

[84] G. Searby, M. Habiballah, A. Nicole, E. Laroche, Prediction of the efficiency of acoustic damping cavities, Journal of Propulsion and Power 24 (3) (2008) 516–523.

[85] R. F. Lambert, A study of the factors influencing the damping of an acoustical cavity resonator, The Journal of the Acoustical Society of America 25 (6) (1953) 1068–1083.

[86] M. N. Vouvakis, K. Zhao, J.-F. Lee, Finite-element analysis of infinite periodic structures with nonmatching triangulations, IEEE Transactions on Magnetics 42 (4) (2006) 691–694.

[87] N. Michailidis, F. Stergioudi, H. Omar, D. Tsipas, An image-based reconstruction of the 3D geometry of an Al open-cell foam and FEM modeling of the material response, Mechanics of Materials 42 (2) (2010) 142–147.

[88] I. Jeon, T. Asahina, K.-J. Kang, S. Im, T. J. Lu, Finite element simulation of the plastic collapse of closed-cell aluminum foams with x-ray computed tomography, Mechanics of Materials 42 (3) (2010) 227–236.

[89] C. Perrot, R. Panneton, X. Olny, Periodic unit cell reconstruction of porous media: application to open-cell aluminum foams, Journal of Applied Physics 101 (11) (2007) 113538.

[90] H. Ke, Y. Donghui, H. Siyuan, H. Deping, Acoustic absorption properties of open-cell Al alloy foams with graded pore size, Journal of Physics D: Applied Physics 44 (36) (2011) 365405.

[91] F. Chevillotte, C. Perrot, R. Panneton, Microstructure based model for sound absorption predictions of perforated closed-cell metallic foams, The Journal of the Acoustical Society of America 128 (4) (2010) 1766–1776.

[92] X. Wang, T. J. Lu, Optimized acoustic properties of cellular solids, The Journal of the Acoustical Society of America 106 (2) (1999) 756–765.

[93] T. J. Lu, F. Chen, D. He, Sound absorption of cellular metals with semiopen cells, The Journal of the Acoustical Society of America 108 (4) (2000) 1697–1709.

[94] F. Mbailassem, E. Gourdon, Q. Leclere, E. Redon, T. Cambonie, Sound absorption prediction of linear damped acoustic resonators using a lightweight hybrid model, Applied Acoustics 150 (2019) 14–26.

[95] G. K. Batchelor, An Introduction to Fluid Dynamics, Cambridge University Press, 2000.

[96] C. Guiping, H. Deping, S. Guangji, Underwater sound absorption property of porous aluminum, Colloids and Surfaces A: Physicochemical and Engineering Aspects 179 (2-3) (2001) 191–194.

[97] M. Berggren, A. Bernland, D. Noreland, Acoustic boundary layers as boundary conditions, Journal of Computational Physics 371 (2018) 633–650.

[98] Y. Miki, Acoustical properties of porous materials-modifications of delany-bazley models, Journal of the Acoustical Society of Japan (E) 11 (1) (1990) 19–24.

[99] R. Bossart, N. Joly, M. Bruneau, Hybrid numerical and analytical solutions for acoustic boundary problems in thermo-viscous fluids, Journal of Sound and Vibration 263 (1) (2003) 69–84.

[100] P. Risby Andersen, V. Cutanda Henríquez, L. Godinho, J.-D. Chazot, J. Carbajo San Martín, Characterization of acoustic metasurface absorbers using numerical methods including viscous and thermal losses, in: INTER-NOISE and NOISE-CON Congress and Conference Proceedings, Vol. 259, Institute of Noise Control Engineering, 2019, pp. 5709–5719.

[101] A. D. Pierce, Introduction to its Physical Principles and Applications, Acoustical Society of America and American Institute of Physics (1981) 122.

[102] M. J. J. Nijhof, Viscothermal wave propagation, Ph.D. Thesis, University of Twente, 2010, https://research.utwente.nl/en/publications/viscothermal-wave-propagation.

CURRICULUM VITAE